Ab Initio Investigations of Solid Electrolytes for Lithium- and Sodium-ion Batteries

by

William D. Richards

Sc.B., Brown University (2010)
M.Phil, University of Cambridge (2011)

Submitted to the Department of Materials Science and Engineering
in partial fulfillment of the requirements for the degree of

Doctor of Philosophy

at the

MASSACHUSETTS INSTITUTE OF TECHNOLOGY

February 2017

Author ..... Signature redacted
Department of Materials Science and Engineering
November 28, 2016

Certified by ..... Signature redacted
Gerbrand Ceder
Visiting Professor
Thesis Supervisor

Accepted by ..... Signature redacted
Donald R. Sadoway
Chairman, Departmental Committee on Graduate Studies

Ab Initio Investigations of Solid Electrolytes for Lithium- and Sodium-ion Batteries

by

William D. Richards

Submitted to the Department of Materials Science and Engineering
on November 28, 2016, in partial fulfillment of the
requirements for the degree of
Doctor of Philosophy

Abstract

Solid-state electrolytes have the potential to dramatically improve the safety and longevity of state-of-the-art battery technology by replacing the flammable organic electrolytes currently employed in Li-ion batteries. Recent advances in the development of new thiophosphate electrolytes have reenergized the field by achieving room temperature conductivities exceeding those liquid electrolytes, but a number of practical challenges to their widespread adoption still exist. This thesis applies ab initio computational methods based on density functional theory to investigate the structural origins of high conductivity in ionic conductor materials and provides a thermodynamic explanation of why the integration of these newly developed thiophosphates into high-rate cells has proven difficult in practice, often resulting in high interfacial resistance.

As a result of these computational investigations, we report the prediction and synthesis of a new high performance sodium-ion conducting material: $Na_{10}SnP_2S_{12}$, with room temperature ionic conductivity of 0.4 mS cm^{-1}, which rivals the conductivity of the best sodium sulfide solid electrolytes to date. We computationally investigate the variants of this compound where Sn is substituted by Ge or Si and find that the latter may achieve even higher conductivity.

We then investigate the relationship between anion packing and ionic transport in fast Li-ion conductors, finding that a bcc-like anion framework is desirable for achieving high ionic conductivity, and that this anion arrangement is present in a disproportionately high number of known Li-conducting materials, including $Na_{10}SnP_2S_{12}$ and its structural analog $Li_{10}GeP_2S_{12}$. Using this bcc anion lattice as a screening criterion, we show that the $I\bar{4}$ material $LiZnPS_4$ also contains such a framework and has the potential for very high ionic conductivity. While the stoichiometric material has poor ionic conductivity, engineering of its composition to introduce interstitial lithium defects is able to exploit the low migration barrier of the bcc anion structure. Thermodynamic calculations predict a solid-solution regime in this system that extends to x = 0.5 in $Li_{1+2x}Zn_{1-x}PS_4$, thus it may yield a new ionic conductor with exceptionally high lithium-ion conductivity, potentially exceeding 50 mS cm^{-1} at room temperature.

Finally, we develop a computational methodology to examine the thermodynamics of formation of resistive interfacial phases through mixing of the electrode and electrolyte. The results of the thermodynamic model of interfacial phase formation are well correlated with experimental observations and battery performance, and predict that thiophosphate electrolytes have especially high reactivity with high voltage oxide cathodes and a narrow electrochemical stability window. We also find that a number of known electrolytes are not inherently stable, but react in situ with the electrode to form passivating but ionically conducting barrier layers.

Thesis Supervisor: Gerbrand Ceder
Title: Visiting Professor

Acknowledgments

I would like to thank my advisor, Professor Gerbrand Ceder, for his guidance and support through this work. His high standards for scientific rigor and clear communication have been instrumental in the development of all of his students. I'm also very appreciative of the latitude that he has afforded me in the direction of study, allowing the exploration of a wide range of topics within this field. I also thank my thesis committee, Professors Jeffrey Grossman and Ju Li, for their helpful comments and discussion while writing this theses.

I'd like to thank the other members of the the LiCon subgroup: Shyue Ping Ong, Yifei Mo, Eric Wang, Lincoln Miara, and Jae Chul Kim, with whom I've collaborated closely on much of this thesis work. I'd also like to thank everyone at Samsung Research Japan, particularly Tomoyuki Tsujimura and Naoki Suzuki, for their tireless experimental efforts on these new materials.

This project was made so much more enjoyable by all the members of the Ceder Group who I've had the pleasure of working with and getting to know over my years here, including Piero Canepa, Stephen Dacek, Alex Toumar, Daniil Kitchaev, Ian Matts, Jinhyuk Lee, Lusann Yang, Nancy Twu, Rahul Malik, Sai Gautam, Alex Urban, Sai Jayaraman, Sangtae Kim, and many others. They have been invaluable, both in their intellectual contributions and discussion of science, as well as their support through this long process.

I'm also grateful for funding provided from Samsung Advanced Institute of Technology, and for computational resources provided by XSEDE.

Finally, I'd like to thank my friends and family who have supported me over the years; I couldn't have made it through without you.

Contents

List of Figures

List of Tables

Introduction

The lithium-ion battery has become ubiquitous in its use to power all manner of devices, with applications ranging from consumer electronics to frequency regulation of the power grid. Lithium-ion batteries are also being increasingly used in vehicle electrification, with various technologies finding applications in both plug-in electric vehicles and hybrids. The dominance of Li-ion technologies have been due to their high energy density, current generation commercial cells are able to achieve approximately 600 Wh L^{-1}. Though they have a long history of use since their commercialization in 1991, serious safety concerns still exist due to their use of flammable organic solvent electrolytes; even recently, a number of major incidents of Li-ion battery fires were caused by ignition of the electrolyte[31, 93, 7]. These safety concerns are especially problematic for grid-scale storage and transport applications including aircraft and automobiles, as the larger size of the batteries in these applications makes heat dissipation and thermal runaway a greater concern.

In addition to the flammability of organic solvents, the transfer of Li-ion technology from consumer electronics to electric vehicles and grid application is placing increasingly more stringent requirements on battery lifetimes. Most consumer products are expected to have lifetimes of a few years, with batteries are subjected to $\sim$100s of charge-discharge cycles;

electric vehicles and grid storage technologies require significantly larger and more expensive batteries that to reduce levelised cost require lifetimes on the order of 10-30 years and many thousands of discharge cycles. The United States Department of Energy has identified the validated performance, particularly the uncertainty over the usable life of batteries, and safety as key barriers to their deployment in energy storage systems [37]. One of the main mechanisms of lithium-ion battery degradation is reaction of the electrolyte with either the anode or the cathode to form a solid electrolyte interphase (SEI) layer, which slowly reduces both capacity and rate capability[5, 155, 154]. These degradation mechanisms can force a tradeoff between capacity and rate performance and cycle life – high capacity and higher rate require typically requires higher voltage cells and smaller particle sizes, but both of these may accelerate the SEI formation by higher oxidation potential of the cathode, and larger surface area to volume ratios[34].

Solid-electrolyte materials have been proposed as a viable non-flammable to organic electrolytes in lithium batteries, and may also aid in solving the SEI formation problem, having no organic components to polymerize by oxidation at the electrode surface. High voltage thin film batteries employing solid electrolytes have already been demonstrated to retain almost full storage capacity over many thousands of cycles [8, 83]. In addition to addressing the safety and SEI concerns, a switch to solid electrolyte materials may also enable novel device geometries to improve packing efficiency and cell capacity, and other advantages including superior electrochemical, mechanical, and thermal stability, absence of leakage, and the possibility of battery miniaturization[74].

The ever-present drive to increase energy density has led to a number of next-generation battery technologies that aim to increase the energy density of one or both electrodes. To

improve capacity of the anode, there is a large body of research on directly using a metal or alloy anode instead of graphite (hard carbon for Na-ion). Metal anodes could improve battery energy density by up to 50 %, but currently cannot be used because of dendrite formation that can cause battery shorting [163]. Protecting the lithium metal anode by a thin layer of solid electrolyte may also improve performance in liquid-electrolyte cells[6]. Use of solid electrolytes has also been proposed in next generation battery materials that eliminate the relatively heavy and expensive transition metal and store energy by direct anion redox. These include lithium-sulfur, with a theoretical specific energy of 2567 Wh kg^{-1} (based on the mass of Li_2S) and lithium-air, with a specific energy of 3505 Wh kg^{-1}(based on the mass of Li_2O_2)[14]. This can be compared with the theoretical energy density of an NMC cathode with a lithium-metal anode, of 1064 Wh kg^{-1}[104]. In terms of energy density (based on the total volume of charged anode and discharged cathode), which is arguably the more important metric for consumer electronic devices, these are 2196 Wh L^{-1} for Li-S, 3506 Wh L^{-1} for Li-air, and 3024 Wh L^{-1} for NMC. The use of solid electrolyte materials in Li-S batteries is attractive as one of the major technological hurdles is the solubility of polysulfides in liquid electrolytes, which are able to slowly discharge the cell [85]. Similarly, Li-air batteries also suffer from parasitic reactions and often fail by electrolyte decomposition[64]. It should be noted that these technologies are significantly less mature than commercialized intercalation Li-ion batteries; there are many other challenges, both in reaction catalysis and electronic and ionic transport within the electrode materials, that also must be addressed.

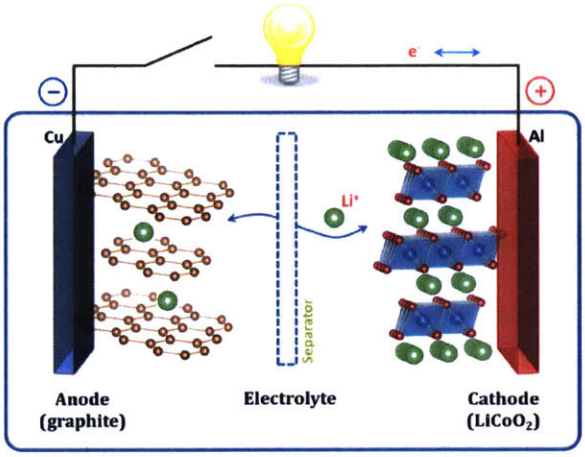

Figure 1-1: **Schematic of an intercalation battery.** The working ion (Li^+) shuttles between high potential (graphite anode) and low potential ($LiCoO_2$ cathode) through the electrolyte. The electron follows the ion through the circuit during discharge, and drives the Li motion during charge with the application of a charging voltage.[36]

1.1 Principles of battery operation

Lithium-ion and other intercalation batteries follow similar principles of operation. The general features, outlined in a simple schematic (Figure 1-1), are instructive for identifying the important properties of an electrolyte material. Energy is stored in the system via the segregation of the working ion, in many cases Li^+, to a region of high chemical potential – the anode. During discharge, these Li^+ ions are allowed to equilibrate to a region of lower lithium chemical potential, the cathode, by traveling through an electrolyte. The electrolyte allows the passage of Li^+ ions, but not electrons, which to maintain local charge neutrality must travel through an external circuit; this flow of electrons can be harnessed to do useful work. In secondary (rechargeable) batteries, the process can be reversed by the application of a voltage across the electrodes.

Battery performance is typically quantified by 3 main parameters:

1. Energy density/specific energy, the volumetric and gravimetric measures of the amount

of energy storage (units Wh L^{-1}, Wh Kg^{-1}). The energy density is determined by the product of capacity (amount of stored Li) and voltage (the energy stored per ion).

2. Rate capability, the speed of charge and discharge (measured in C, where 1C rate means charging or discharging fully in 1 hour, and 5C is full charge or discharge in 12 minutes)

3. Cycle life, or the deterioration in energy density or rate performance of the battery after repeated charge/discharge cycles, typically measured as a percentage of first cycle capacity.

Considering this mechanism of operation, a few key properties of electrolyte materials become apparent. The electrolyte must be an electronic insulator to force electrons through the external circuit and suppress self-discharge of the battery. To enable high charge and discharge rates, the ionic conductivity of the electrolyte must be high. The electrolyte must be stable against decomposition with the electrode and cathode materials (the different types of stability will be discussed in greater detail in Chapter 5). These properties are required for both liquid and solid electrolytes. Currently, state of the art organic solvent electrolytes achieve room temperature conductivity on the order of 5-10 mS cm^{-1} [148]. The higher transference number of solid electrolytes (typically $\sim$1 vs $\sim$0.3 for liquid electrolytes) means that to achieve charge and discharge rates competitive with liquid electrolytes, a solid electrolyte needs to have a conductivity of greater than 2 mS cm^{-1} assuming a similar diffusion distance. For thin film batteries this requirement is reduced, though with a substantial increase in manufacturing cost.

1.2 Li- and Na-ion batteries

Lithium ion batteries, first commercialized by Sony in 1991, make up an enormous fraction of the cells used in portable electronics today, and are in use in many electric vehicles. They typically operate via reversible intercalation of lithium ions between a graphite (Li_xC_6) anode and a transition metal oxide ($Li_{1-x}MO_2$) cathode, most typically with either cobalt, nickel or manganese (or some combination) as the transition metal. Another common cathode is $LiFePO_4$, which has an olivine structure. Voltages of these cells are typically between 3 and 5 V vs. Li metal, and determined primarily by the redox potential of the metal. Currently, the barriers to utilizing the highest voltage material are limited by electrolyte stability.

Sulfide cathode materials are also possible. One of the first Li-ion battery cathodes was layered TiS_2, though oxides are generally preferred because of their significantly higher voltage and lower weight, and hence higher energy density. Besides layered graphite anodes, Si and Sn alloy anodes are also used because of their higher capacity, though they show higher voltages vs. Lithium[52, 162, 167]. Lithium titanium oxide anodes also have a high voltage ($\sim$1.5 V) vs. Li metal, but show very minimal strain on cycling and are used for their high rate capability and cycle life[59].

Despite the long history of development of sodium batteries dating to the 1960s, and their concurrent development with Li-ion, development of Na-ion batteries for a while stagnated due to their lower voltage and energy density compared with Li. Na-ion batteries are emerging as candidates for large scale energy storage due to their low cost and the wide variety of cathode materials available. In addition to sodium being considerably more abundant than lithium, Na-ion batteries have the advantage of a broader range of available cathode

materials since many layered Li-transition metal oxides show improved performance in their sodium versions[24, 73, 114]. In addition, many high capacity Na cathodes do not contain cobalt, an expensive and scarce component of many commercial Li-ion cathodes.

A major difference between the Li-ion and Na-ion systems is the choice of anode. Sodium does not intercalate into graphite, and so other anode materials must be used, typically hard carbon, or titania[113]. Despite much work in the area, no sodium anode materials have been found that can match the conductivity, energy density, and price of graphite anodes in Li-ion batteries. Though hard carbon anodes have been shown to reversibly intercalate sodium[75], capacity is very low compared to that allowed by intercalation to LiC_6[113].

In both Li and Na-ion batteries, the choice of electrolyte is important for device performance. Because the cell voltage exceeds 1.23 V, the decomposition potential of water, aqueous electrolytes cannot be used. Typically, the electrolyte is an alkyl carbonate such as ethylene carbonate (EC) or dimethyl carbonate (DMC) with $LiPF_6$. These materials are unstable below 1.5 V vs. lithium metal, forming a solid-electrolyte-interphase (SEI) layer that partially passivates the surface[91]. Organic electrolytes can also be oxidized by the cathodes when delithiated. This is especially an issue with high-voltage cathodes (e.g. $LiNiO_2$) and so the use of organic electrolytes puts an upper limit on the safe operating voltage. Similar problems are seen in Na-ion batteries. The choice of electrolyte for Na-ion systems is not as well established as for Li-ion, but the vast majority of electrolytes in development are based on organic solvents[117]. These suffer from the same flammability concerns as their counterparts in lithium batteries, and are exacerbated by the presence of a more reactive metal.

1.3 Solid electrolytes

Development of solid-electrolytes, particularly for Li-ion batteries, has proceeded rapidly in recent years, with the conductivity of some systems even approaching and surpassing that of liquid electrolytes. Figure 1-2 shows the conductivities of a number of these materials. Solid electrolyte materials can be broadly categorized by their anion; most electrolyte materials are either sulfides or oxides.

Li-ion conducting oxides for electrolyte materials are most commonly found in the LISICON[13] (e.g., $Li_{14}ZnGe_4O_{16}$), NASICON[72, 28, 4] (e.g., $Li_{1.3}Al_{0.3}Ti_{1.7}(PO_4)_3$), perovskite[55] (e.g., $La_{0.5}Li_{0.5}TiO_3$), garnet[100, 107, 1] (e.g., $Li_7La_3Zr_2O_{12}$), and LiPON[165] (e.g., $Li_{2.88}PO_{3.73}N_{0.14}$) systems. These conductors exhibit ionic conductivities at RT on the order of 10^{-3} to 1 mS cm^{-1} with E_a ranging from 0.3 to 0.6 eV[74]. These systems typically require high synthesis temperatures[142] and cosintering to obtain good contact between the electrode and electrolyte[108], which is important for battery performance[140, 50].

Thiophosphate materials based on Li_3PS_4[134] have recently emerged as a novel class of superionic conducting materials with even higher conductivities and whose mechanical properties allow better physical contact with electrodes. Examples of these include the thio-LISICON conductor $Li_{3.25}Ge_{0.25}P_{0.75}S_4$ (2.2 mS cm^{-1} at RT, E_a= 0.22 eV [70]), $Li_{10}GeP_2S_{12}$ (LGPS), with a conductivity of 12 mS cm^{-1} at room temperature[65], and $Li_7P_3S_{11}$, a glass-ceramic with a room temperature conductivity of 17 mS cm^{-1}[129]. Less expensive versions of LGPS where Ge is replaced by Sn or Si have also been predicted[109] and synthesized[161, 78, 79, 12]. These thiophosphates are promising candidates as solid electrolytes as they

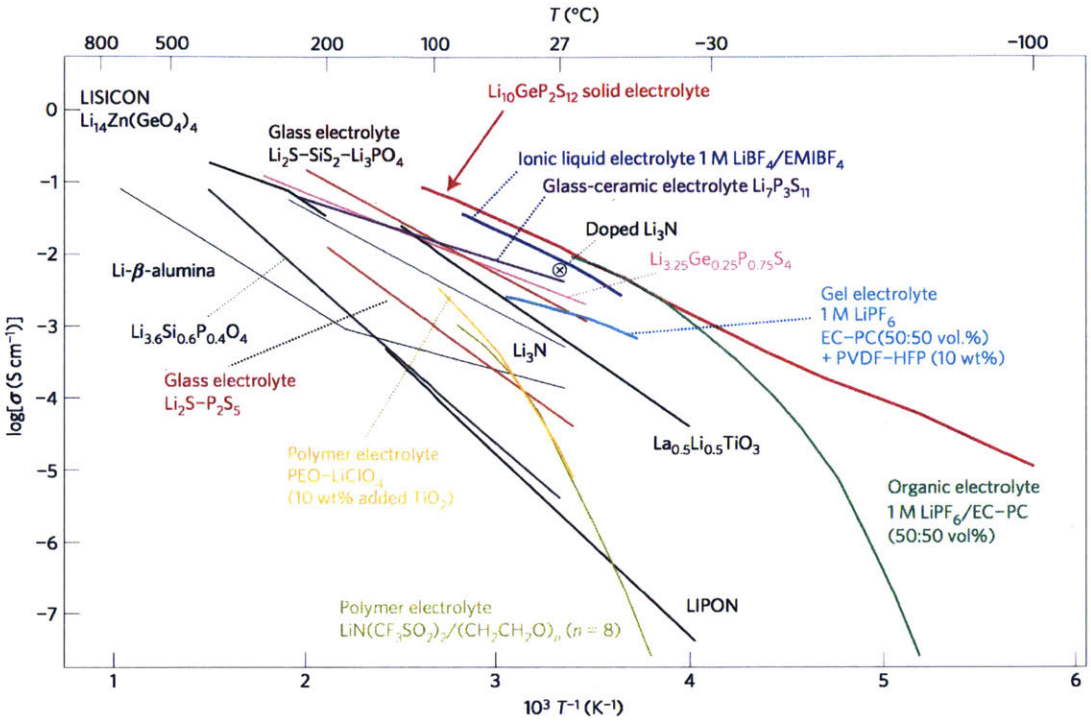

Figure 1-2: **Conductivity of Li-ion solid-electrolytes.** [65]

are soft and can be incorporated into batteries by cold pressing without requiring high temperature sintering. Remarkably, the conductivity of these thiophosphate materials even surpasses that of the liquid electrolyte $LiPF_6$ in EC/DMC, the electrolyte most commonly used in commercial cells today.[148].

In order to use solid electrolytes with lithium metal anodes dendrite formation must be suppressed; one approach is by using the mechanical contact between the electrolyte and lithium metal. This is a promising area of research, though even with use of very hard electrolyte materials realization of this goal has proven difficult as lithium dendrites are often still able to form through grain boundaries and small void spaces [120, 145].

The general trend of sulfide vs. oxide properties is similar for sodium solid electrolytes, though they are somewhat less well studied. The conductivities of a number of Na-ion

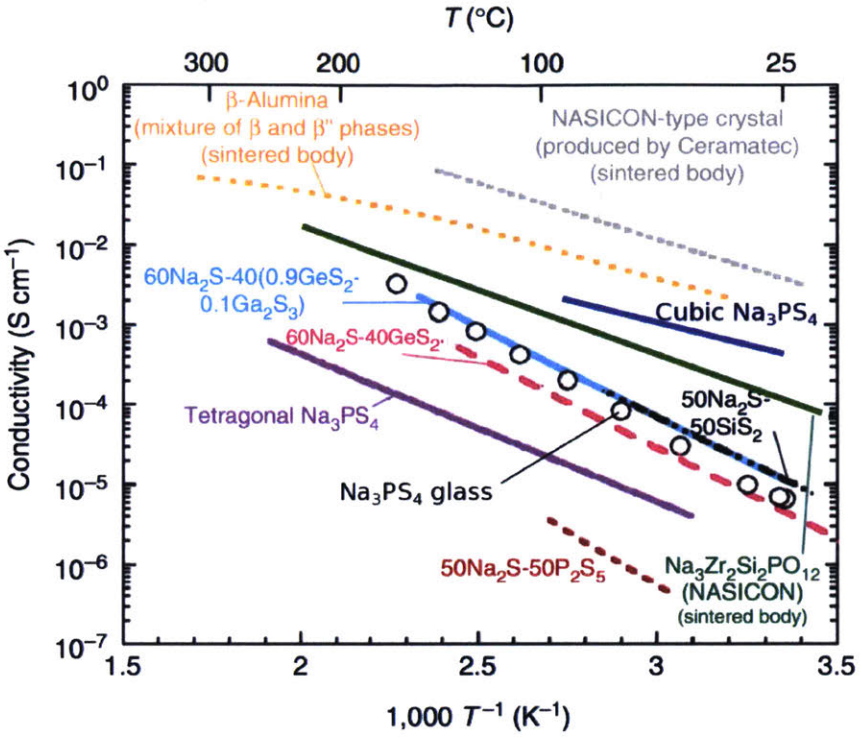

Figure 1-3: **Conductivity of Na-ion solid-electrolytes.** Adapted from reference [43]

conductors are shown in figure 1-3. Na-solid electrolytes have been commercialized in high temperature batteries such as β-alumina for sodium-sulfur (NAS) batteries[51], yet few materials with high conductivities at low temperature have been reported. Ionic conductivity of over 1 mS cm^{-1} has been shown in NASICON-type oxide crystals [72, 28], but processing of these materials at high temperatures (typically $> 1000\,^{\circ}$C [166, 51]) is required to reduce grain boundary resistance, which is incompatible with typical cathode materials and complicates battery fabrication. Recently the cubic phase of Na_3PS_4 has been reported to have conductivity as high as 0.46 mS cm^{-1}, and has been used in an all-solid-state battery[43, 44]. Silicon doping can increase defect concentrations in Na_3PS_4, resulting in a conductivity of 0.7 mS cm^{-1}[139]. For construction of solid-state cells, low strain electrodes[158, 159] are also important to minimize delamination of the electrolyte, especially when using harder

electrolyte materials such as oxides.

1.4 Organization of this thesis

The work in this thesis was undertaken with the broad goals of 1) understanding the factors that govern ionic diffusivity in solid electrolyte materials and allow superionic conductivity in some classes of materials, 2) investigating the interfacial phenomena leading to high interfacial resistance at the electrode, and 3) the discovery and design of new, improved materials.

Chapter 2 applies computational thermodynamics and transport simulations for the prediction of $Na_{10}SnP_2S_{12}$, a new sodium-ion conductor isostructural to LGPS, and its subsequent experimental realization. In chapter 3, we investigate the link between structure geometry and high ionic conductivity. We introduce an algorithm to rigorously compare crystal structures, and apply it to discover that many high-conductivity materials share a common bcc anion framework. Chapter 4 applies this insight to design a new Li-ion conductor, $Li_{1+2x}Zn_{1-x}PS_4$, with exceptionally high predicted conductivity. Finally, in chapter 5, we study electrolytes from a different perspective, examining the compatibility of electrolyte and electrode materials. We find that interfacial reactivity can be predicted from bulk thermodynamics, and that it is a very good predictor of cell performance. Applying this methodology to known materials, we explain the poor performance of electrolyte systems that appear to be highly stable from cyclic voltammetry measurements, and provide guidelines for designing high-rate cells. Because some of the techniques used in this thesis are used in multiple chapters, these methods are described separately, in Appendix A.

Chapter 2

Computational prediction of $Na_{10}SnP_2S_{12}$

Motivated by the the increased study of Na-ion batteries and its dearth of anode materials, we report the computation-assisted discovery and synthesis of a new high performance solid-state electrolyte material: $Na_{10}SnP_2S_{12}$. The synthesized material is found to have a room temperature ionic conductivity of 0.4 mS cm^{-1}, which rivals the conductivity of the best sodium sulfide solid electrolytes to date. We also computationally investigate the variants of this compound where Sn is substituted by Ge or Si and find that the latter may achieve even higher conductivity.

The high ionic conductivity, cycling performance, and chemical variability within the tetragonal lithium thiophosphates of $Li_{10}MP_2S_{12}$ (M = Si, Ge, Sn) [65, 109, 161, 78, 79, 12, 71] make the investigation of sodium versions of these materials attractive. Of course, the use of sodium versions in battery systems requires that these materials be thermodynamically

stable (such that they can be synthesized), and also that sodium-ion mobility is high.

Using first principles computations based on Density Functional Theory (DFT, see A.1), we evaluate three key properties of the tetragonal phases of $Na_{10}MP_2S_{12}$ (M = Si, Ge, Sn) to determine their suitability as a solid state electrolyte materials: 1) we determine the Na^+ conductivity and its activation energy from ab initio molecular dynamics (AIMD, see A.2) simulations, 2) using high throughput computations and structure prediction methods we comprehensively calculate the ground state phase diagram of each system to gauge the stability and synthesizability of each compound, and 3) we extract the electrochemical anodic and cathodic stability limits from the grand canonical equilibrium at various potentials similar to the approach described in an earlier work [111]. Based on this data, we then proceeded to synthesize and test $Na_{10}SnP_2S_{12}$[122].

2.1 Ground-state energy calculations

Since there is typically considerable cation site disorder in these conductors, we used an electrostatic energy criterion to pre-sceen Na/Vacancy orderings on the experimentally reported structure of LGPS [80]. For each of the 3 symmetrically distinct M/P orderings and for full and half Na4 site occupancy, we relaxed the structures of the lowest electrostatic energy arrangements using Density Functional Theory (DFT), taking the lowest energy of these as the 0 K enthalpy and structure. The structure of $Na_{10}MP_2S_{12}$ (NMPS) can be described as consisting of three symmetrically distinct chains of cations oriented parallel to the c-axis (see Figure 2-1). At unit cell coordinates x=0.25, y=0.25, tetrahedral Na sites (Na1, Na3) form a chain of partially occupied edge sharing sites. At x=0, y=0.5 there is an

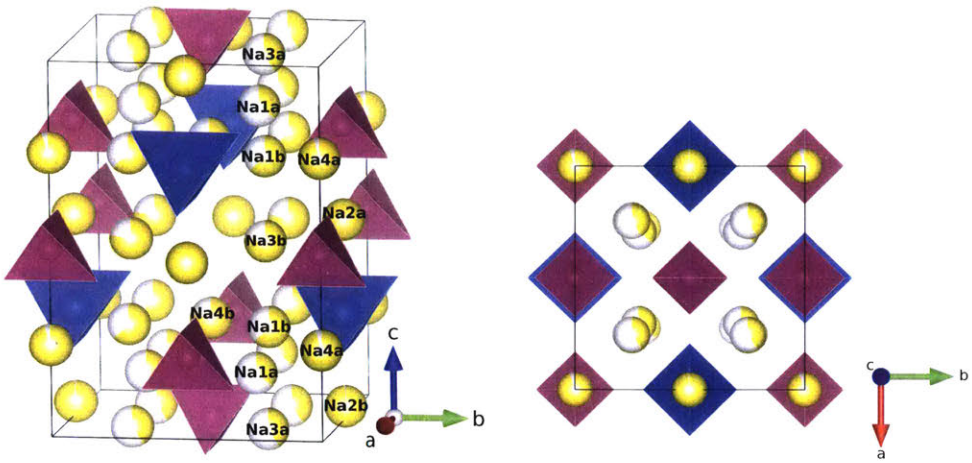

Figure 2-1: **Structure of $Na_{10}SnP_2S_{12}$ from DFT calculations.** Sodium occupancies are calculated from 600 K AIMD simulation (see section 2.7). All ground state NMPS structures share this M/P ordering, which reduces the symmetry from the $P4_2/nmc$ space group to $P\bar{4}m2$, separating the each Na site into two symmetrically distinct but similar sites marked a and b. PS_4 tetrahedra are marked in purple, SnS_4 tetrahedra in blue, and Na sites in yellow.

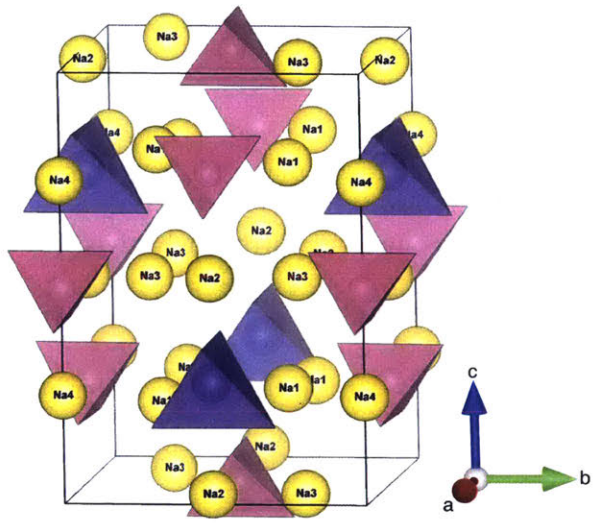

Figure 2-2: ***C*222 symmetry ground state ordering of Na atoms for the NMPS phases.** Labels on the Na-atoms correspond to those of the $P4_2/nmc$ space group disordered structure.

edge sharing chain of alternating Na_{oct} and $(M/P)_{tet}$ sites. At x=0, y=0, a similar chain but with a vacancy instead of M cation and more distorted Na_{oct} site is present (with repeat unit Na_{oct}-P_{tet}-Na_{oct}-Vac_{tet}). The ab initio MD results will demonstrate that the (Na1, Na3)

chains carry most of the Na conductivity with occasional crossover through the Na sites in the chain at x=0, y=0. The ground state M/P ordering, which is found to be shared among all studied chemistries, is shown in Figure 2-1 and the ground state Na-ion arrangement ($C222$ space group) in Figure 2-2.

2.2 Ab initio molecular dynamics

The Na ionic conductivity (σ), and activation energy (E_a) were determined from AIMD simulations between 600 K and 1300 K and extrapolated to room temperature. Ionic conductivity is calculated from AIMD through the intermediate calculation of D_σ, which has the units of a diffusivity but takes into account correlations between Na-ions (see section 2.7). The results are shown in Figure 2-3a, and compared to similar Li compounds in Table 2.1. The self diffusivity (D_{self}) of the Na ions was also calculated for comparison, with results included in Table 2.2. For both the Li and Na materials, activation energy slightly increases as M changes from Si $\rightarrow$ Ge $\rightarrow$ Sn. Somewhat surprisingly given the size difference between Na and Li ions, Na and Li materials have similar activation energies, resulting in high room temperature conductivities particularly for the Ge and Si materials which are predicted to have room temperature conductivities comparable to those of organic electrolytes[117]. Our result for $Na_{10}GeP_2S_{12}$ is similar to the result of ref. [66]. The degree of cooperativity of ionic motion is described by the Haven ratio H_r[99], which we calculate from the ratio of D_{self} to D_σ. This value is calculated to be approximately 0.56 in all of our simulations, which is slightly smaller than that observed experimentally for the lithium versions of these materials[79, 78], indicating a larger degree of cooperative motion.

Compound	DFT Simulation		Experimental	
	E_a (eV)	Conductivity, 298 K (mS cm^{-1})	E_a (eV)	Conductivity, 298 K (mS cm^{-1})
$Na_{10}SiP_2S_{12}$	0.229	10.28		N/A
$Na_{10}GeP_2S_{12}$	0.270	3.50		N/A
$Na_{10}SnP_2S_{12}$	0.317	0.94	0.356	0.4 (this work)
$Li_{10}SiP_2S_{12}$	0.20	23 [109]	0.196	2.3 [161]
$Li_{10}GeP_2S_{12}$	0.21	13 [109]	0.22 - 0.25	9 - 12 [78, 65]
$Li_{10}SnP_2S_{12}$	0.24	6 [109]	0.24 - 0.27	4 - 7 [79, 12]

Table 2.1: **Ionic conductivity of cation-substituted compounds $X_{10}MP_2S_{12}$ (X=Li, Na; M=Si, Sn, Al).** DFT simulation and experimental results on the sodium structures are from this work. Experimental and calculated values for the Li compounds are taken from the literature.

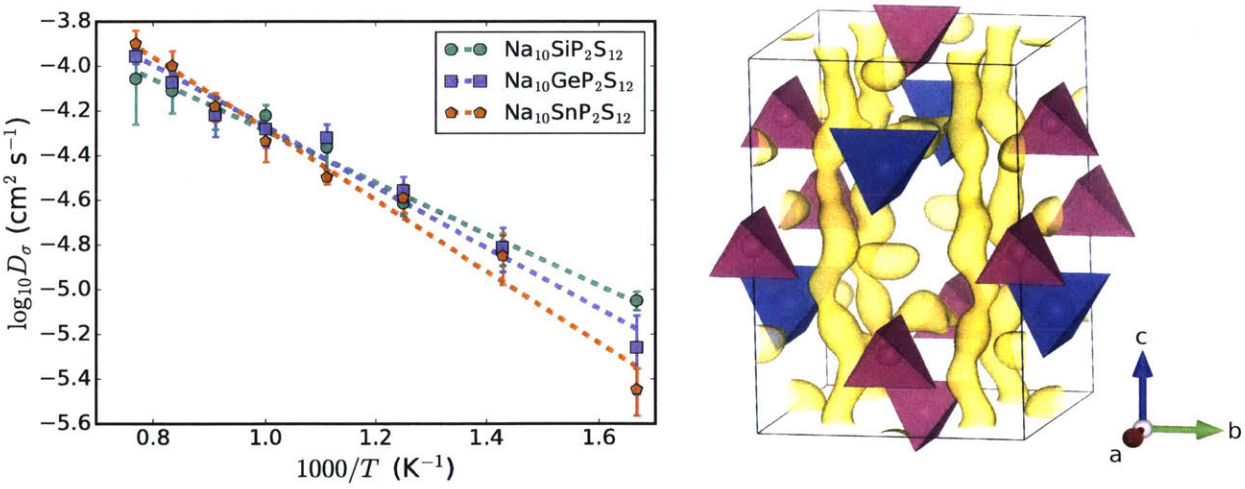

(a) (b)

Figure 2-3: **DFT computed diffusivity of $Na_{10}SnP_2S_{12}$.** a) Na diffusivity in $Na_{10}SiP_2S_{12}$, $Na_{10}GeP_2S_{12}$, and $Na_{10}SnP_2S_{12}$ from AIMD simulation. Dashed lines are Arrhenius fits to the data, and error bars are s.e.m. b) Na-ion probability density isosurface (yellow) of $Na_{10}SnP_2S_{12}$ from 600 K AIMD simulation. SnS_4 tetrahedra are marked in blue, PS_4 tetrahedra in purple.

Compound	E_a (eV)	Self diffusivity D_{self} at 298 K (cm^2 s^{-1})
$Na_{10}SiP_2S_{12}$	0.204	1.13×10^{-7}
$Na_{10}GeP_2S_{12}$	0.252	2.97×10^{-8}
$Na_{10}SnP_2S_{12}$	0.307	6.94×10^{-9}

Table 2.2: **Calculated self diffusivity D_{self} of $Na_{10}MP_2S_{12}$ (M = Si, Sn, Al).** Note that the differences between these activation energies and the activation energies of D_{corr} listed in table 2.1 are not statistically significant.

2.3 Phase diagrams and stability limits

To determine the feasibility of synthesizing these high conductivity tetragonal phases of $Na_{10}MP_2S_{12}$ (M = Si, Ge, Sn), we used DFT to evaluate the energies of materials and generate their respective quaternary phase diagrams. To obtain appropriate competing phases in the quaternary phase diagrams, we calculated the energy of a very large number of compounds in their relevant chemical spaces, including all known materials present in the Inorganic Crystal Structure Database (ICSD)[9] containing some or all of the four elements, all relevant materials derived from substituting sodium for lithium in all ICSD materials and the $Li_xP_yS_z$ structures compiled by Lepley et al.[82]. To further improve the coverage of these chemical spaces, we also applied the data-mined substitution methodology of Hautier et al.[41] to predict possible structures from a broader range of chemistries in the ICSD. The 0 K phase diagram for the Na-Sn-P-S, Na-Ge-P-S and Na-Si-P-S systems are shown in Figure 2-4.

No quaternary ground states are found in any of the three systems. Decomposition energy (E_{decomp}) to the equilibrium ground state structures is calculated using the convex hull method implemented in pymatgen [110] and is shown in Table 2.3, and compared to their lithium counterparts. For example, the stability of the $Na_{10}SnP_2S_{12}$ phase is given

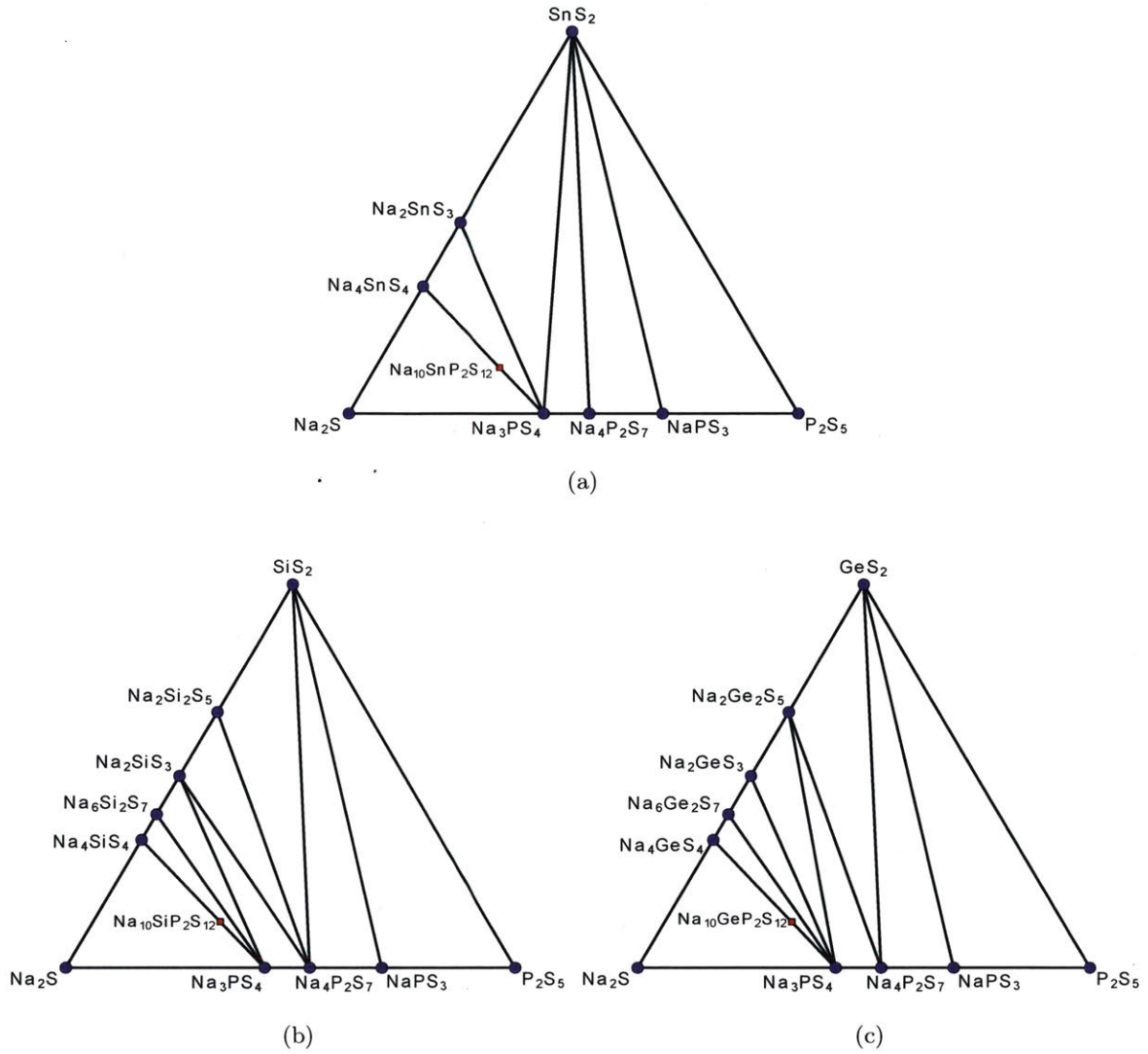

Figure 2-4: **Pseudo-ternary 0K phase diagrams for the NMPS systems.** a) Na_2S-SnS_2-P_2S_5, b) Na_2S-SiS_2-P_2S_5 and c) Na_2S-GeS_2-P_2S_5 chemical systems, computed from DFT energy calculations. Stable phases marked with blue dot.

by the calculated enthalpy of the decomposition reaction $Na_{10}SnP_2S_{12} \rightarrow 2\ Na_3PS_4 + Na_4SnS_4$. Even though all the considered electrolyte structures show a small driving force at 0 K to decompose to $(Li/Na)_4MS_4$ (M = Si, Ge, Sn) and $(Li/Na)_3PS_4$, this is similar to the Li-analogs which have similar decomposition energies, and have all been synthesized [65, 12, 161, 79]. We expect high configurational entropy on the cation sites to result in

their stabilization at moderate temperatures. An approximation of this entropy, neglecting the ion-ion interactions, can be obtained using the formula $S = -k_B \sum_i p_i \ln p_i$, where k_B is the Boltzmann constant, p_i is the probability of each state (occupied or unoccupied), and the sum is over all states for each site. Using a value of 50% occupancy of the Na-atoms in the edge-sharing c-axis chains and 50% M/P occupancy (28 sites with 50% occupancy per 50 atom unit cell) yields a value of 0.0334 meV K^{-1} $atom^{-1}$, which at 300 K already would stabilize the Sn and Ge compositions. This is an upper bound on the configurational entropy but vibrational entropy, particularly the soft phonon modes of the diffusing ions, is also expected to contribute to the structure's stabilization. Table 2.3 also shows the calculated anodic and cathodic stability limits evaluated from the chemical potentials of Na at which the compound decomposes, following the methods of reference [111]. Since these materials by our calculations are metastable at 0 K, we instead consider the potentials at which the ground state materials equilibrium becomes unstable, e.g. for $Na_{10}SnP_2S_{12}$, when either Na_4SnS_4 or Na_3PS_4 becomes unstable.

Cation (X)	Cation (M)	Decomposition products	E_{decomp} (meV $atom^{-1}$)	Metal reduction (V vs. metal anode)	Cathodic stability (V vs. metal anode)	Anodic stability (V vs. metal anode)
Na	Si	Na_4SiS_4 + 2 Na_3PS_4	13.6	0.80	1.25	1.77
	Ge	Na_4GeS_4 + 2 Na_3PS_4	7.2	1.10	1.25	1.70
	Sn	Na_4SnS_4 + 2 Na_3PS_4	7.1	1.09	1.25	1.82
Li	Si	Li_4SiS_4 + 2 Li_3PS_4	14.9	1.36	1.78	2.14
	Ge	Li_4GeS_4 + 2 Li_3PS_4	14.7	1.64	1.78	2.06
	Sn	Li_4SnS_4 + 2 Li_3PS_4	13.4	1.57	1.78	2.02

Table 2.3: **Phase equilibria decomposition enthalpies and stability ranges for $X_{10}MP_2S_{12}$.**

When the chemical potential (voltage) of the alkali is below (above) the stable region (as can be experienced at the cathode interface during charging), the ion and its associated

electron is pulled from the electrolyte, which decomposes into a mixture of sulfides and elemental sulfur (e.g. Na_4SnS_4 decomposes to S and Na_2SnS_3 above 1.82 V vs. Na metal, and S and SnS_2 above 2 V). In contact with the anode (cathodic limit), the Li/Na metal may reduce the metal or phosphorus in the electrolyte, potentially leading to electron conductivity through the electrolyte if this reaction continues without passivation. The cathodic limit for Na and Li compounds is set by the partial reduction of phosphorus to form Na_2PS_3, and the calculated cathodic stability is thus unaffected by the choice of metal (M) cation. The potentials at which the metal cation is fully reduced by the alkali are also listed in table 2.3, and indicate the potential at which the decomposition reaction is no longer passivating. The shift in the stability window between the Na and Li materials is due to the differing reduction potentials of the alkali metal. Previous DFT studies have shown that this reduction reaction can be passivated in some systems by the formation of a thin layer of Li_2S [82], though in practice insulating barrier coatings are typically employed at the anode/cathode interfaces [65, 123, 136]. The anodic voltage stability limit is set primarily by the reaction energy of the alkali metal with elemental sulfur, though in compounds with highly negative enthalpies of mixing from the binary sulfides the stability range is extended slightly. This effect is small in the considered electrolyte materials, with the anodic stability only changing on the order of 0.1 V between materials with different (M) cations.

2.4 Synthesis and experimental verification

In validation of our computational predictions, we report successful synthesis of $Na_{10}SnP_2S_{12}$, which was chosen due to its low materials cost and E_{decomp} of 7.1 meV atom^{-1},

which is lower than comparable materials which have been synthesized. $Na_{10}SnP_2S_{12}$ was prepared from the binary sulfide phases, under a range of cooling rates. $Na_{10}SnP_2S_{12}$ was synthesized by mixing stoichiometric amounts of Na_2S (Kojundo Chemical Laboratory Co. Ltd., 99%), P_2S_5 (Sigma-Aldrich Co., 99%), and SnS_2 (Kojundo Chemical Laboratory Co. Ltd., 99.9%) with a planetary ballmill (380 rpm for 17 h). The pelletized mixture was wrapped in gold foil and heated at 700 °C for 12 h in an evacuated quartz tube and slow-cooled down to room temperature for 99 hours (approximately -0.1 deg min^{-1}). The X-ray diffraction pattern is obtained with Cu-K_α radiation (40kV, 40mA) from 10-90° 2 theta with 0.03° step intervals.

The lattice volume and conductivity of the synthesized phase increase as the cooling rate is lowered (see Figure 2-5), with the highest conductivity achieved by cooling from 700 °C over 99 hours. Na-ion conductivity was measured with electrochemical impedance spectroscopy (EIS) using an AUTOLAB PGSTAT30 (Metrohm Autolab, Utrecht) at 30°C, 40°C, 60°C and 80°C with a frequency ranging from 1 MHz to 100 mHz and an amplitude of 10 mV under normal pressure. An indium foil blocking electrode was pressed onto both sides of the $Na_{10}SnP_2S_{12}$ pellet (11.5 mm diameter and 0.75 mm thickness). The conductivity values were obtained from the Cole-Cole plot of the data.

To compare the experimental XRD pattern with that predicted from DFT calculation, we used the Na and Sn/P site disordered structure with positions and fractional occupancies of each site generated from k-means clustering of Na-position data from the 600 K AIMD simulation as a starting point for powder XRD simulation of the structure. Comparison of the simulated and experimental XRD patterns is shown in Figure 2-6a. The obtained material is predominantly the expected tetragonal $Na_{10}SnP_2S_{12}$, with small amounts of

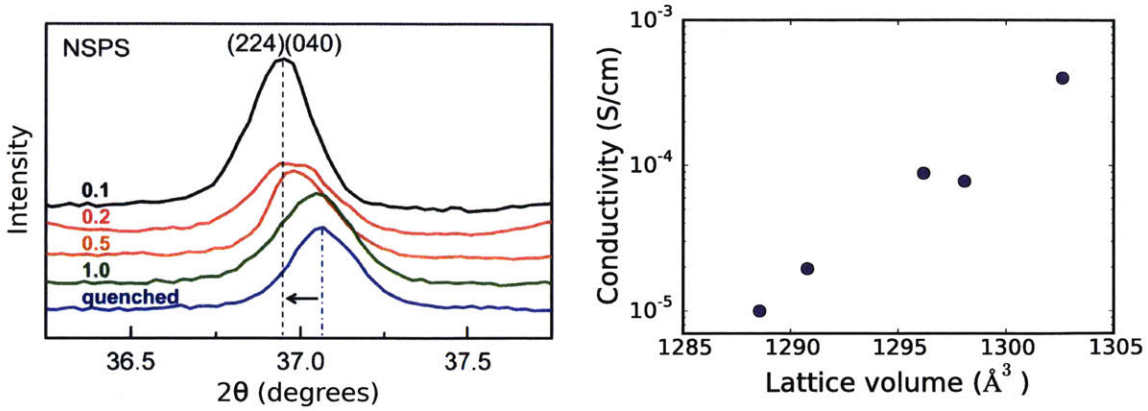

(a) (b)

Figure 2-5: **XRD as function of cooling rate for NSPS.** a) Main peak position for cooling rates of 0.1, 0.2, 0.5, and 1.0 K min^{-1}, and a quenched sample. Lattice volume increases as cooling rate is lowered b). Measured conductivity vs. lattice volume for these samples.

P_2S_5, Na_3PS_4, primarily in the tetragonal α-phase as indicated by the peak splitting at 31 and 36 degrees[43], and Na_2S, which formed during the slow cooling. At faster cooling rates, these impurity phases do not form but the resulting material has lower conductivity due to the lower lattice volume. The change in the lattice volume and conductivity is likely a result of the structure in the slow cooled sample having a higher ratio of Sn to P, since the observed impurities contain no Sn. Similar dependency of conductivity and lattice volume on this ratio are seen in the lithium systems[49]. The low conductivity of the impurity phases the slow-cooled sample are expected to reduce the measured conductivity by reduction in the effective cross-sectional area. The strong relation between lattice volume and conductivity also support the conductivity measured in the slow-cooled sample being that of $Na_{10}SnP_2S_{12}$.

The intensities of the 011 and (110 and 002) reflections, producing XRD peaks at 12

and 16 degrees, vary as a function with cooling rate, but are not strongly correlated with conductivity. Figure 2-6b shows the XRD spectrum of a quenched sample in which these low angle peaks are more clearly visible. The variation in these peak intensities may be caused either by slight disorder between the P_{tet}, M_{tet}, and Vac_{tet} sites, or by changes in average size of the $(Sn/P)S_4$ tetrahedra from slight compositional variation.

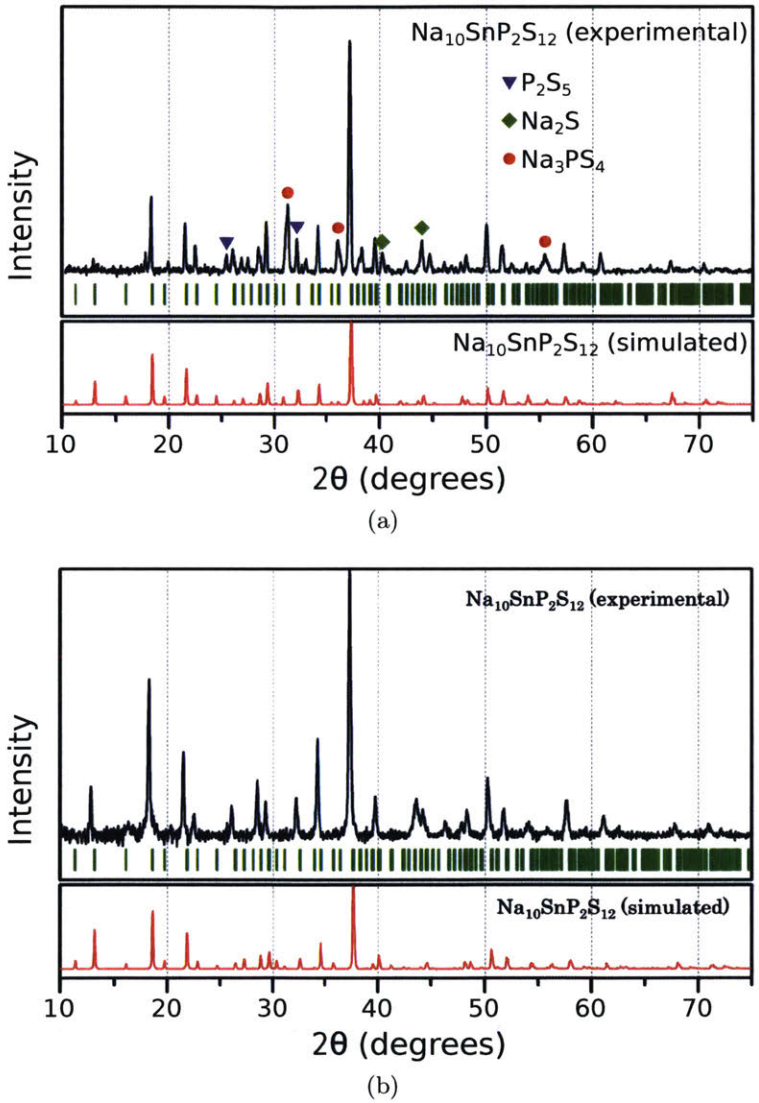

Figure 2-6: **Experimental and simulated XRD patterns of annealed and quenched $Na_{10}SnP_2S_{12}$.** XRD spectrum taken with Cu-K_α radiation (40kV, 40mA) a) Annealed experimental and simulated XRD patterns of $Na_{10}SnP_2S_{12}$, showing small amounts of re-crystallized P_2S_5, Na_3PS_4, and Na_2S. b) XRD of the quenched sample.

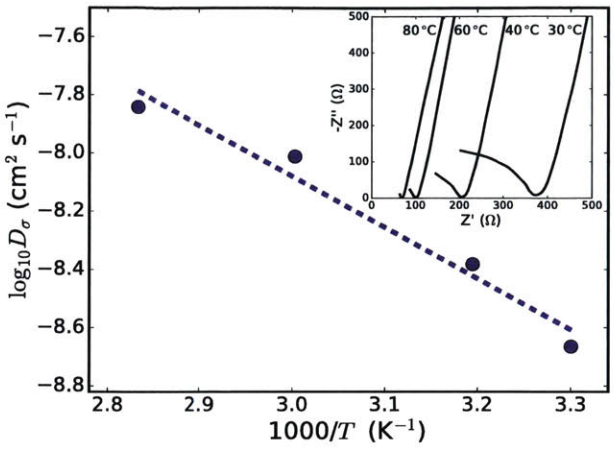

Figure 2-7: **Experimental crystal structure and diffusivity of $Na_{10}SnP_2S_{12}$..** Diffusivity calculated from experimentally measured ionic conductivity vs. temperature. Dashed line is an Arrhenius fit to the data. (inset) Electrochemical impedance spectroscopy measurements.

Considering that AIMD simulations were performed at elevated temperatures and extrapolated to experimental conditions, the conductivity predicted from these simulations is in remarkable agreement to our experimental electrochemical impedance spectroscopy (EIS) results (Figure 2-7). We predicted a room temperature conductivity of 0.94 mS cm^{-1} with activation energy of 317 meV, while experimentally $Na_{10}SnP_2S_{12}$ shows a conductivity of 0.4 mS cm^{-1} with an activation energy of 356 meV.

2.5 Discussion

$Na_{10}SnP_2S_{12}$ is a remarkably good ionic conductor; its room temperature conductivity of 0.4 mS cm^{-1} is comparable to the best performing sulfide electrolyte to date - cubic Na_3PS_4, which achieves conductivities of between 0.2 and 0.7 mS cm^{-1} depending on doping and processing conditions [43, 44, 139]. These thiophosphate electrolytes benefit from improved processability relative to the oxide β-alumina and NASICON-based compounds, which can

have higher conductivities but require high temperature sintering, making them difficult to incorporate into room temperature batteries. To evaluate the potential for even better conductors in this family of compounds we investigate in more detail the conductivity mechanism in these compounds and the effect of the main group metal (Si, Ge, Sn) on it.

From our DFT calculations, we see that the activation energy for Na diffusion in the NMPS materials shown in Figure 2-3a increases as the ionic radius of the (M)etal in the compound increases, with $E_a^{Si} < E_a^{Ge} < E_a^{Sn}$. This trend is also seen in activation energies for the Li conductors, both in experimental and DFT studies (Table 2.1). This is surprising since often the activation energy barrier between adjacent sites in a structure decreases as the size of the anion framework increases. In the NMPS conductors, however, the lattice parameter differences are small (<1%, Table 2.4), and the activation energy actually increases as the cell volume increases. The valence of the other cations near the transition state has been pointed to as an important factor as it can increase the activation energy by strong repulsion of the alkali in the activated state[67, 152], but this is unlikely to play a role here as Si, Ge, and Sn all have valence 4+. Hence, because of their similar volume and cation valence, these three compounds form a good dataset to evaluate potentially more subtle chemical influences on the conductivity. To understand the somewhat counterintuitive result, we examine the diffusion paths and site occupancies in each compound as a measure of the free energy landscape of the structures.

Cation (M)	a (Å)	c (Å)
Si	9.60	13.53
Ge	9.62	13.59
Sn	9.68	13.63

Table 2.4: **DFT calculated lattice parameters for tetragonal $Na_{10}MP_2S_{12}$ (M = Si, Ge, Sn).**

From the AIMD Na-ion trajectories we calculate the Na-ion probability density, defined as the time-averaged Na-ion occupancy, allowing visualization of the Na ion diffusion mechanism. The probability density from AIMD simulation of $Na_{10}SnP_2S_{12}$ at 600 K in Figure 2-3b is representative of all of our AIMD simulations, and shows that the majority of the Na diffusion occurs within the c-axis chain of partially occupied Na sites at x=0.25 and y=0.25, with some crossover between these channels. These results are in good qualitative agreement with the highly anisotropic Li sites seen in previous spectroscopic studies on LGPS [65, 80].

The Na-site occupancies of the three materials as a function of simulation temperature are shown in Figure 2-8. $P4_2/nmc$ spacegroup operations are applied to the Na-positions before analysis to undo the splitting of Na sites caused by the M/P ordering and shown in Figure 2-1. Trends in occupancy are similar for Na-sites that are part of the same c-axis cation chain, again confirming a flat energy landscape and high mobility along it. These Na-ion diffusion pathways are connected to each other through the Na4 (Na-crossover) sites, which are part of the Na_{oct}-P_{tet}-Na_{oct}-Vac_{tet} chain along the c-axis at x=0, y=0. The Na sites in the fully occupied Na_{oct}-P_{tet}-Na_{oct}-M_{tet} c-axis chain at x=0, y=0.5 have low energy and high occupancy, and are labeled as Na-immobile sites in Figure 2-8 as they are not expected to contribute strongly to diffusion at low temperatures.

At high temperatures the occupancies of each Na site are almost identical across the three chemistries, indicating that they are dominated by entropic effects and not by the specific enthalpic differences between the compounds. At low temperatures, relative occupancies are more dependent on differences in site enthalpy. Considering first the Sn material, the occupancy of the Na-crossover sites dramatically increases as temperature is reduced, indicating

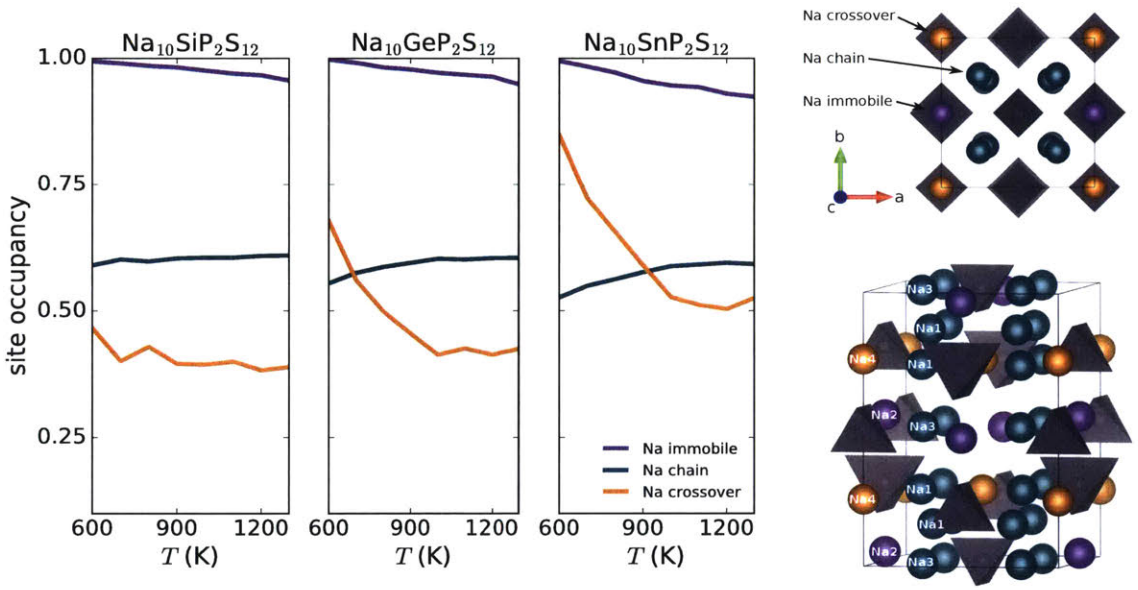

(a) (b)

Figure 2-8: **Na-site occupancy analysis of NMPS structures.** a) Occupancy of Na sites in $Na_{10}SiP_2S_{12}$, $Na_{10}GeP_2S_{12}$, $Na_{10}SnP_2S_{12}$ from AIMD simulation between 600 and 1300 K, after imposing $P4_2/nmc$ spacegroup operations. The site occupancies in the Na-chain (Na1 and Na3) have been combined for clarity. b) Illustration of the Na-chain, Na-crossover, and Na-immobile sites. SnS_4 and PS_4 tetrahedra (grey), all spheres are Na sites.

that the enthalpy of the Na-crossover sites is significantly lower than the Na-chain sites. In contrast to $Na_{10}SnP_2S_{12}$, occupancy of the Na-crossover sites in the Si material is relatively unaffected by temperature, indicating minimal site enthalpy difference between the Na-chain and Na-crossover sites. The behavior of occupancies in $Na_{10}GeP_2S_{12}$ is between these two extrema.

The diffusivity of Na-ions is determined primarily by the smoothness of their free energy landscape. In materials where atoms can be trapped in very low energy minima, activation energy for moving between these sites is increased, and thus diffusivity is reduced. The trends in Na-crossover site energy correlate well with the activation energies observed in simulation and explain why $Na_{10}SiP_2S_{12}$ has the highest predicted conductivity. At low T, the energy of the Na in the chain and crossover sites are almost equal, allowing Na to migrate in 3 dimensions with a very low barrier.

The good correspondence between the simulated and experimental results highlight the value of DFT as a predictive tool for the identification of new electrolyte materials. We focused synthesis efforts on the Sn material due to its affordability relative to the Ge version as well as its low E_{decomp} of 7.1 meV atom^{-1}, which is lower than comparable materials which have been synthesized. In LGPS and related lithium electrolytes, contact with the highly reducing lithium metal or graphite anode can cause electrolyte decomposition by reduction of the transition metal. For these sodium electrolytes this may be less of a concern due to the lower reduction potential of sodium. These newly predicted materials may also prove to be more stable in battery applications than cubic Na_3PS_4 material, since decomposition of $Na_{10}MP_2S_{12}$ requires diffusion of high-valent cations to form Na_3PS_4 and Na_4MS_4, in contrast to cubic Na_3PS_4, which can convert to a low conductivity tetragonal phase [60]

at the same composition. The conductivity of the new $Na_{10}SnP_2S_{12}$ electrolyte rivals that of the best known sulfide sodium-conductors, and the predicted Ge and Si materials, if confirmed, have the potential to surpass the conductivities of all known Na electrolytes in a system much more compatible with all solid-state battery fabrication than NASICON-based and other oxide electrolytes.

2.6 Conclusions

In this chapter, we used first principles calculation to predict the existence of several new high-performance sodium electrolyte materials, with excellent agreement to subsequent experimental results. This marks the first use of computational prediction to design novel sodium electrolytes. The resulting $Na_{10}SnP_2S_{12}$ electrolyte, with a conductivity of 0.4 mS cm^{-1} at room temperature and activation energy of 0.35 eV, rivals the best existing sulfide sodium-electrolytes and our predicted materials have the potential to surpass this conductivity. Through site-occupancy analysis of the AIMD simulations, we also show how the various metal substitutions in this framework can affect cation mobility by modulating the free energy landscape.

2.7 Computational Details

2.7.1 Density functional theory calculations

All ab initio structure calculations were performed with calculations implemented in VASP[76], using the projector augmented-wave method[10]. Calculations used the Perdew-Burke-Ernzerhof generalized-gradient approximation (GGA)[115]. For energy calculations

of NMPS structures, a Monkhorst-Pack k-point grid of 4x4x4 was used, for other competing phases, k-points were chosen such that $n_{\text{kpoints}} \times n_{\text{atoms}} > 1000$. The VASP pseudopotential set of Li (PAW_PBE Li 17Jan2003), Na (PAW_PBE Na 08Apr2002), Ge (PAW_PBE Ge 05Jan2001), Si (PAW_PBE Si 05Jan2001), Sn (PAW_PBE Sn_d 06Sep2000), P (PAW_PBE P 17Jan2003), and S (PAW_PBE S 17Jan2003) was used. Phase diagrams were constructed using a convex hull algorithm in energy-composition space, using tools implemented in the pymatgen software package[110].

2.7.2 Conductivity simulations

We performed ab initio molecular dynamics (AIMD) simulations under the Born-Oppenheimer approximation using VASP[76]. Atom trajectories are calculated with Verlet integration in an NVT ensemble. A Nose-Hoover thermostat with a period of 40 timesteps (80 fs) was used for all simulations. Na atom displacements are calculated with respect to the center of mass of the framework (non-Na) atoms.

Self-diffusivities from these simulations were calculated by fitting the Einstein relation of mean squared displacements to time ($\langle \|\Delta \mathbf{x}\|^2 \rangle = 2dD_{\text{self}}t$), where d is the dimensionality, using tools implemented in the pymatgen software package[110]. Ionic conductivities taking into account correlations between Na ions were calculated from the mean square displacement of the net Na-ion motion $\left\langle \left\| \sum_{i=1}^{n} \Delta \mathbf{x}_i \right\|^2 \right\rangle = 2dD_{\sigma}nt$. Inserting D_{σ} into the Nernst-Einstein equation is equivalent to using the Green-Kubo expression for ionic conductivity when Na-ions are the only mobile charge carriers[45, 146].

The AIMD simulations were performed on a single unit cell of NMPS, with 50 ions (2 formula units). The volume and shape of the cells were obtained from the fully relaxed cells

used for the energy calculations by enforcing tetragonal symmetry (equality of the a and b lattice parameters). The time step of the simulation was 2 fs. To reduce the computational cost of the calculation, forces were calculated using a single k-point. Temperatures were initialized at 300 K and scaled to the appropriate temperature over 1000 time steps (2 ps), starting from the ground state structure. Simulations between 600 K and 900 K lasted 350,000 time steps (700 ps), and simulations above 900 K lasted 250,000 time steps (500 ps).

Calculation of the activation energy (E_a) and extrapolation of results to room temperature was performed with an Arrhenius fit to the diffusivity data. The Haven ratio, H_r, an indication of the cooperativity of ionic motion, is calculated from the ratio of D_{self} to the D_σ in each simulation.

2.7.3 Ionic probability density

Na-ion probability densities were calculated from the AIMD simulations. After enforcing $P4_2/nmc$ symmetry, Na-ion positions relative to the center of mass of the framework (P, M, S) atoms were smoothed using a Gaussian kernel with standard deviation of 0.2 Å, and the resulting density visualized using Vesta[96].

2.7.4 Fractional occupancies

Fractional occupancies were calculated using a k-means clustering algorithm[87], initialized with atomic positions from the structure of LGPS[80]. At each clustering step, the shortest distance (taking into account periodic boundary conditions) to each mean was calculated, and a linear assignment algorithm[61] as implemented in pymatgen[110] was used at each simulation time step to assign each Na-ion position to the nearest mean, ensuring that at

most a single Na atom from each time step is assigned to any given mean. The resulting cluster sizes and centroids were used to define the occupancy and location of Na sites.

Chapter 3

The effects of anion framework on ionic conduction

The results of the previous chapter, specifically the close parallels between the performance of the Li and Na versions of the tetragonal structural frameworks, suggest that structural features of the conductor play a large role in determining ionic conductivity. Here, we reveal a more fundamental relationship between anion packing and ionic transport in fast Li-ion conducting materials, finding that the similarities in crystal structure between $Li_{10}GeP_2S_{12}$ and $Na_{10}SnP_2S_{12}$ actually place them within a much larger, though up until now unrecognized, family of ionic conductors even including the high conductivity phase of silver iodide. We find that an underlying body-centered cubic (bcc)-like anion framework that allows direct Li hops between adjacent tetrahedral sites is most desirable for achieving high ionic conductivity. This anion arrangement is present (albeit in a highly distorted state) in several fast ionic conductors.

3.1 Diffusion within crystal structures

The basic step in ionic diffusion is the migration of the ion between stable sites through a higher energy environment. The highest energy along this path is the activation energy for migration, which in good ionic conductors contributes the main component to the activation energy for long-range diffusion. The stable site for Li in ionic materials is usually a tetrahedral or octahedral site connected to other polyhedral sites in the structure through shared anion triangles. Examples of such paths in common battery cathode materials such as spinel oxides or rocksalt-type oxides are well established[151, 147]. To understand the topology of sites in good Li-ion conductors we begin by examining the crystal structure of two compounds having the highest Li-ion conductivity reported to date, $Li_{10}GeP_2S_{12}$[65, 78] and $Li_7P_3S_{11}$[164, 129]. The structure of $Li_{10}GeP_2S_{12}$ can be characterized by predominantly tetrahedral coordination of Li, Ge and P cations within a tetragonal lattice[65, 80]. In the structure of $Li_7P_3S_{11}$, corner-sharing $P_2S_7^{4-}$ ditetrahedra and PS_4^{3-} tetrahedra are surrounded by Li ions primarily having tetrahedral coordination[164]. To better understand the anion arrangements in these structures, we apply a structure matching algorithm to map the sulfur positions to the three most common crystal lattices: body-centered-cubic (bcc), face-centered-cubic (fcc) and hexagonal close-packed (hcp) lattices. Despite seeming to be very different structures, we find that the sulfur sublattices of both $Li_{10}GeP_2S_{12}$ and $Li_7P_3S_{11}$ very closely match a bcc lattice. The matchings are graphically shown in figures 3-1.

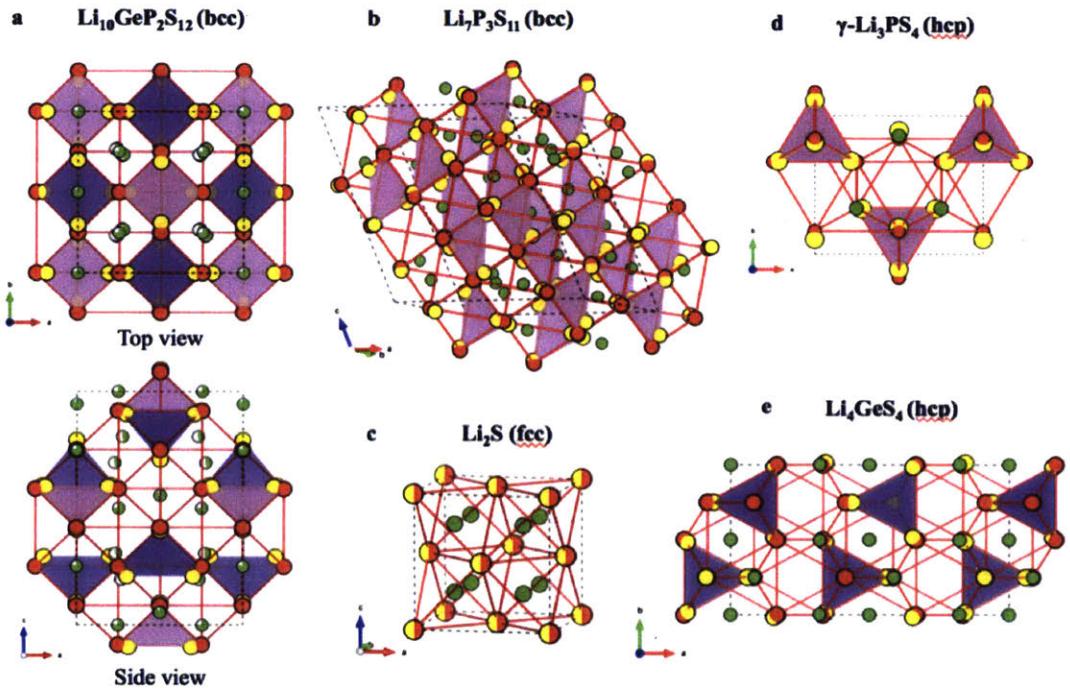

Figure 3-1: **Mapping of the anion sublattice to a bcc/fcc/hcp framework in solid-state Li-ion conductors.** Crystal structure of Li-ion conductors a) $Li_{10}GeP_2S_{12}$, b) $Li_7P_3S_{11}$, c) Li_2S d) γ-Li_3PS_4, and e) Li_4GeS_4. Li atom, partially occupied Li atom, S atom, PS_4 tetrahedra and GeS_4 tetrahedra (partially occupied in $Li_{10}GeP_2S_{12}$) are colored green, green-white, yellow, purple and blue, respectively. In both $Li_{10}GeP_2S_{12}$ and $Li_7P_3S_{11}$ the sulfur anion sublattice can be closely mapped to a body-centered-cubic (bcc) framework (red circles connected by red lines). In Li_2S the anion sublattice is an exact face-centered cubic (fcc) matrix (yellow-red circles). The anion sublattices in γ-Li_3PS_4 and Li_4GeS_4 are closely matched to a hexagonal close-packed (hcp) framework.

3.2 Comparison of ideal sulfur sublattices

To explain the predominance of bcc sulfur frameworks in high-conductivity solid electrolytes, we use the nudged elastic band method to determine Li^+ migration barrier within the bcc, fcc and hcp S^{2-} anion lattices in the dilute limit of a single Li^+ in a fixed S2- lattice with no other cations present. This computational experiment allows us to directly assess the effect of the anion configuration. The fcc and hcp lattices are present in many lithium sulfide materials, for example Li_2S has an fcc sulfur sublattice (Figure 3-1c); Li_4GeS_4 and γ-Li_3PS_4 (space group: Pmn21), the parent structures of $Li_{10}GeP_2S_{12}$ and other thio-LISICONs, both have an hcp sulfur sublattice (Fig 3-1d and Fig 3-1e). We use a lattice volume of 40 $Å^3$ per S atom (the same as $Li_{10}GeP_2S_{12}$) to keep the same free volume for Li diffusion in all anion lattices. The migration paths and their energy are shown in Figure 3-2.

We find that for all S lattices Li is most stable in the tetrahedral site. In the bcc S^{2-} lattice, the Li ion migrates with a remarkably low barrier of only 0.15 eV along a path connecting two face-sharing tetrahedral sites (T1 and T2 in Figure 3-2a), hereafter denoted as the T-T path. In the fcc anion lattice, Li migration between two tetrahedral sites (T1 and T2 in Figure 3-2b) is via an intermediate octahedral site (O1), hereafter denoted as the T-O-T path. This path is similar to what has been documented in fcc-structured oxides[67, 151]. The presence of the octahedral site along the path makes the barrier for T-O-T type migration in fcc much higher (0.39 eV at this volume). The T-O-T type path can be also found in the ab-plane of the hcp lattice (T1 to T2 through O1 in Figure 3-2c) with an almost identical activation barrier (0.40 eV). Li migration along the c-axis of the hcp lattice is primarily though a path connecting two face-sharing tetrahedral sites (T1 and T3)

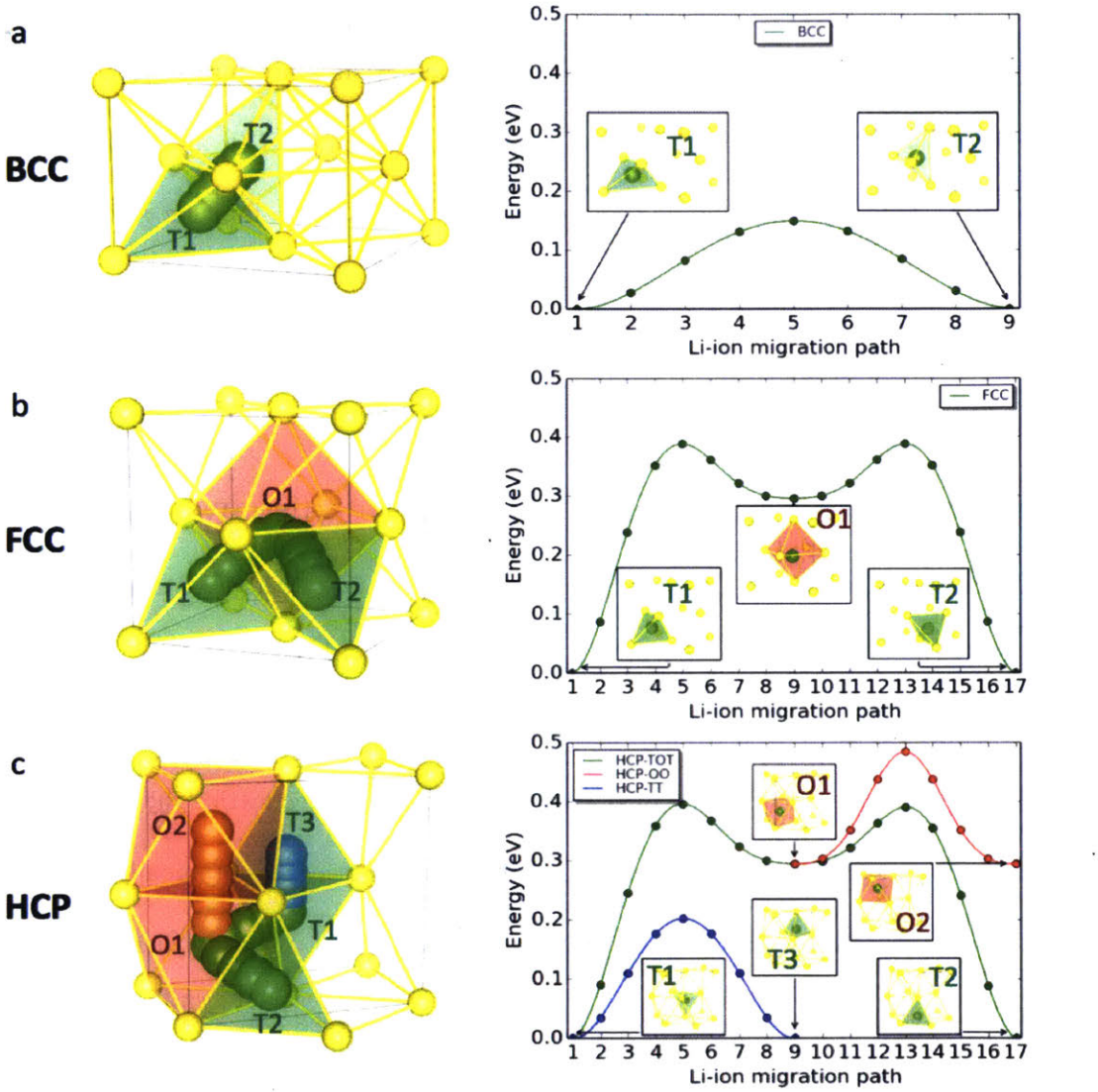

Figure 3-2: **Li-ion migration pathways in bcc/fcc/hcp-type anion lattices.** Li-ion migration path (left panels) and calculated energy path (right panels) in bcc (a), fcc (b) and hcp (c) sulfur lattices. The sulfur anions are colored yellow, and the Li ions are colored green, blue and red for different paths. LiS_4 tetrahedra and LiS_6 octahedra are colored green and red, respectively.

with a lower barrier (0.20 eV), but it does not percolate and requires Li migration through octahedral sites to achieve long-range Li diffusion. Li could also migrate between face-sharing octahedral sites (O1 and O2, 0.19 eV) along the c-axis, however additional activation energy is required to access this path as the octahedral sites are unstable. Therefore, Li conduction in a hcp lattice likely occurs by an alternation of T-T and T-O-T hopping, and the T-O-T hops, with higher energy barriers, are the rate-limiting steps. At room temperature this difference in activation energies between the bcc T-T path and hcp/fcc T-O-T paths corresponds to about three orders of magnitude difference in conductivity (σ), according to the relation $\sigma \sim e^{\frac{-E_a}{kT}}$.

Volume is thought to be an important factor in ion mobility[109]. We extend our analysis by evaluating the previously discussed migration barriers in all three lattices as a function of volume between 28.5 $Å^3$ (S atom) to 70.8 $Å^3$/(S atom) which is the range observed in the Inorganic Crystal Structure Database (ICSD)[9] for compounds that contain Li and S but not N, O, Se, F, Cl, Br, I or H (Figure 3-3). We find that for the bcc lattice the tetrahedral site is lowest in energy for all volumes, with the Li migration barrier monotonically decreasing as volume increases. The bcc arrangement remains optimal for Li mobility across all volumes (Figure 3-4). In fcc and hcp lattices the Li migration mechanism varies with the lattice volume. At small volumes (regime I in Figure 3-4), the most stable Li sites are octahedral due to the larger size of this site and the activation barrier is very large due to a large energy penalty when Li ion passes through an extremely small three-coordinated bottleneck. As the volume gets larger (regime II in Figure 3-4), the tetrahedral site becomes more stable, and the activation energy decreases as the size of the three-coordinated bottleneck increases. The crossover in site energies creates non-monotonic behavior of the migration

energy with volume in these close-packed lattices. At larger volumes (regime III in Figure 3-4), the octahedral site is no longer stable, and Li migration occurs directly between two tetrahedral sites bypassing the center of the octahedra, with a decreasing barrier as the volume further increases. The results in Figure 3-4 indicate clearly that bcc is the preferred anion arrangement for Li-ion conductors due to the low barrier of the T-T path.

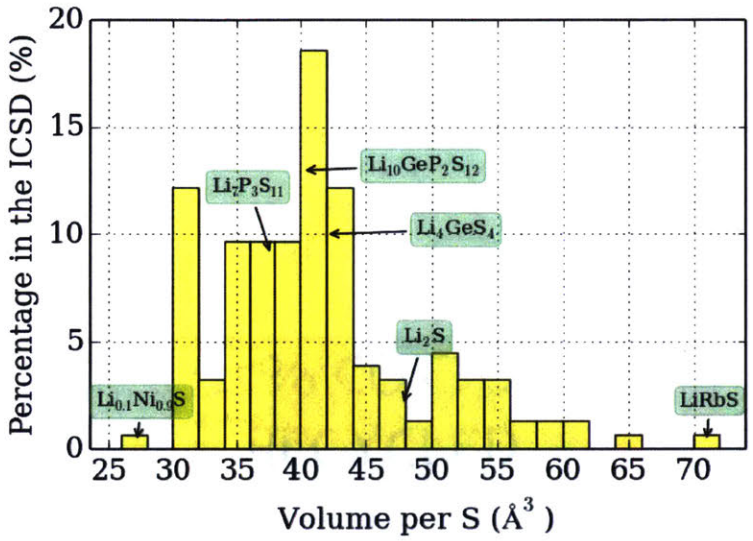

Figure 3-3: **Volume per sulfur atom for materials in the ICSD.** Materials were chosen that contained lithium and sulfur but no other anion species (N, O, Se, F, Cl, Br, I) or hydrogen. The data set from ICSD we use is cleaned by removing duplicate structures.

The above model analysis is validated by comparing it to the experimental activation energy in real compounds. The calculated 0.15 eV barrier in the bcc sulfur lattice with a volume of 40 Å^3 is only slightly lower than the experimentally determined activation energies of $Li_{10}GeP_2S_{12}$ (0.25 eV[65] and 0.22 eV[78]) and other derivatives with similar structures (0.22 eV of Li_7GePS_8[78], 0.20 eV of $Li_{10}SiP_2S_{12}$[161] and 0.27 eV of $Li_{10}SnP_2S_{12}$[79, 12]), and very close to that of $Li_7P_3S_{11}$ (0.18 eV[129]) with a similar volume (37.7 Å^3), as shown in Figure 3-4. The experimental activation energies of Li_4GeS_4 (0.53 eV[98] with volume of

41.8 Å^3) and γ-Li_3PS_4 (0.49 eV[98] with volume of 38.6 Å^3) are also close to the calculated barrier for the hcp lattice (0.40 eV at V=40.0 Å^3). It is to be expected that the barriers for real compounds are higher than those in our model analysis, as the electrostatic interaction between the migrating Li^+ and the other cations is usually the highest in the activated state[67, 153], so adding the relevant cations in our simulations would increase activation energies. For materials without any tetrahedral vacancies such as Li_2S, our model underestimates the diffusion activation energy as it considers only the migration barrier and not the contribution of the defect (e.g., vacancy) formation energy.

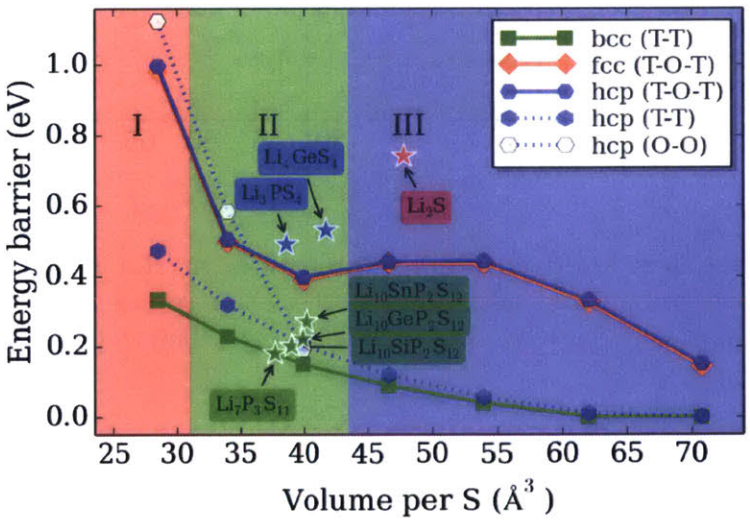

Figure 3-4: **Activation barrier for Li-ion migration versus lattice volume.** Activation barrier calculated for the Li-ion migration pathways in the bcc/fcc/hcp S^{2-} lattices at different volumes. Solid and dotted lines are guides to the eye. Experimental activation energies for $Li_{10}GeP_2S_{12}$[65, 80], $Li_{10}SnP_2S_{12}$[12, 79], $Li_{10}SiP_2S_{12}$[161], $Li_7P_3S_{11}$[129], Li_2S[85], Li_4GeS_4[98] and γ-Li_3PS_4[98] are marked by a star symbol for comparison. The underestimate of the activation energy for Li_2S is due to fact that the experimental value contains contributions from the defect formation energy.

3.3 Li-ion probability density analysis

Our analysis of differences in the diffusion mechanisms of bcc, fcc and hcp sulfur lattices are further confirmed by the probability density of Li ions obtained from ab initio molecular dynamics (AIMD) simulations for several Li-ion conductors (Figure 3-5). The simulations are performed at 900K to speed up diffusion and reduce the simulation time. The probability density is defined as the time-averaged spatial occupancy probability of Li-ions in the crystal structure, and is inversely correlated to the Li site energy. For two sites with probabilities P1 and P2, the difference in their free energies can be given approximately by $\Delta G = -kT\ln(P_1/P_2)$. At 900 K, each doubling of probability corresponds to a decrease in Li site energy of about 50 meV.

The distribution of Li ions in $Li_{10}GeP_2S_{12}$ demonstrates that conduction occurs predominantly via the channels connecting tetrahedrally coordinated Li sites along the c-axis (Figure 3-5a). Notably, the probability density extends between these tetrahedral sites with relatively large probabilities, suggesting high Li occupancy along the diffusion channels, which is also seen experimentally[65, 95]. The evenly distributed probability densities indicate that Li ions have a relatively flat energy landscape along the channels, and the energy barriers for diffusion between these sites are low, in agreement with our analysis of the bare sulfide lattices. In $Li_7P_3S_{11}$ the probability densities form a three-dimensional Li diffusion network (Figure 3-5b). As compared to $Li_{10}GeP_2S_{12}$, the densities in $Li_7P_3S_{11}$ are more evenly distributed within the diffusion network, confirming the small activation energy of 0.18 eV (0.19eV) reported experimentally[129] (computationally), even lower than that of $Li_{10}GeP_2S_{12}$ (0.22-0.25 eV[65, 78]). In contrast, Li ions are almost exclusively found on

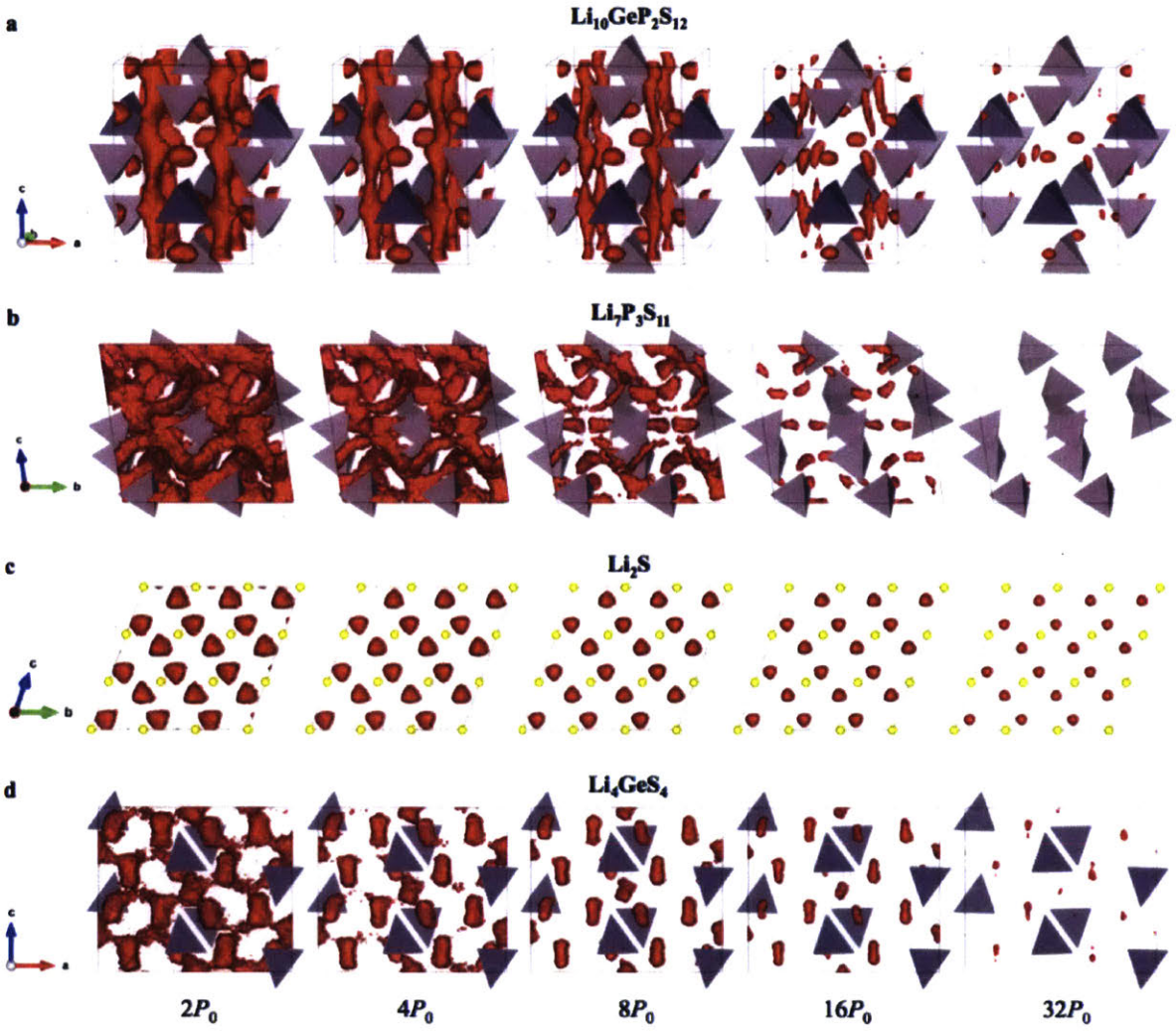

Figure 3-5: **Li ion probability densities in Li-ion conductors.** The probability densities of Li ions are obtained from AIMD simulations at 900 K in a) $Li_{10}GeP_2S_{12}$, b) $Li_7P_3S_{11}$, c) Li_2S, and d) Li_4GeS_4. Isosurfaces of the ionic probability densities are plotted at increasing isovalues ranging from $2P_0$ to $32P_0$, where P_0 is defined to be the mean value of the lithium atomic density for each structure. PS_4 tetrahedra and GeS_4 tetrahedra are colored purple and blue, respectively. The sulfur atoms are shown as small yellow circles for Li_2S

the isolated tetrahedral sites in the fcc sulfur framework of Li_2S (Figure 3-5c) even when Li vacancies are induced (see Methods). The Li occupancy is negligibly small at the octahedral sites, which are required to connect the tetrahedral sites and form a percolating diffusion network. The absence of a connected diffusion network indicates that the Li ions hop through these octahedral sites at a very low frequency, and that the octahedral-site energies are much higher than in the tetrahedral sites, again in agreement with the results on the bare sulfide lattices. In Li_4GeS_4, which has an underlying hcp sulfur lattice, the probability densities are localized in pairs of face-sharing tetrahedral sites (elliptical regions in Figure 3-5d), corresponding to the T-T path (Figure 3-2c). A percolation network for long-range Li diffusion can be only formed through the bridging octahedral sites, which have significantly smaller occupation probability. Therefore, the energy landscape for Li-ions in Li_4GeS_4 and Li_2S is considerably more corrugated than in $Li_{10}GeP_2S_{12}$ or $Li_7P_3S_{11}$, leading to the higher activation energies found in Li_4GeS_4 and Li_2S.

3.4 Discussion

A general principle for the design of Li-ion conductors with low activation energy can be distilled from the above findings: all the sites within the diffusion network should be energetically close to equivalent, with large channels connecting them. The superior ionic conductivity of Li-ion conductors with a bcc-like anion framework, e.g., $Li_{10}GeP_2S_{12}$ and $Li_7P_3S_{11}$, is due to the primarily tetrahedral coordination of the Li ions and their geometric similarity to the bcc anion sublattice, which contains a percolating network composed entirely of tetrahedral sites that are crystallographically and energetically equivalent. This

is unlike structures with the more common hcp or fcc anion frameworks, which require migration through sites with very different coordination (e.g. 4 and 6) to achieve percolation.

In Figure 3-6 we show the Li-containing sulfides from ICSD screened with our bcc framework matching algorithm. Transition-metal (TM) containing compounds are excluded as TM cations can be easily reduced by the lithium anode. Only 25 compounds can be matched to bcc, and most of them are significantly distorted from a perfect bcc lattice. The superionic conductors $Li_{10}GeP_2S_{12}$ and $Li_7P_3S_{11}$ are among the few sulfides that are well matched to bcc. This screening demonstrates that the bcc framework serves as a descriptor for Li-ion conductors with high conductivity. A few other Li-ion conductors, such as Li_3BS_3[156] and β-Li_3PS_4 (space group: Pnma)[48, 86], which are reported to exhibit high conductivities and low activation energies, also emerge from this screening. Note that the screening results include materials whose closest match is fcc or hcp sublattice (e.g. Li_4GeS_4, γ-Li_3PS_4 to hcp, see Methods) but that can be mapped to bcc if relatively large length and angle deviations are allowed. As the bcc framework is much less common for anions than hcp or fcc, very high ionic conductivity is limited to a small group of compounds.

We expect the above principle to be transferable to other combinations of mobile cations and immobile anion lattices. For example, in the recently discovered Li-ion conductors Li_3OCl and Li_3OBr with the anti-perovskite structure[168] the oxygen and halide anions are bcc packed. With the presence of Li interstitials the activation energy can be as low as 0.17 eV as they activate a path connecting energy-equivalent tetrahedral sites[25]. The known fast Ag^+ and Cu^+ conducting halides and chalcogenides (e.g., α-AgI) also have bcc anion sublattices, and possess higher ionic conductivities than fcc and hcp-based phases[53]. These findings are also transferable to other chemical systems; the migration barrier is lowest

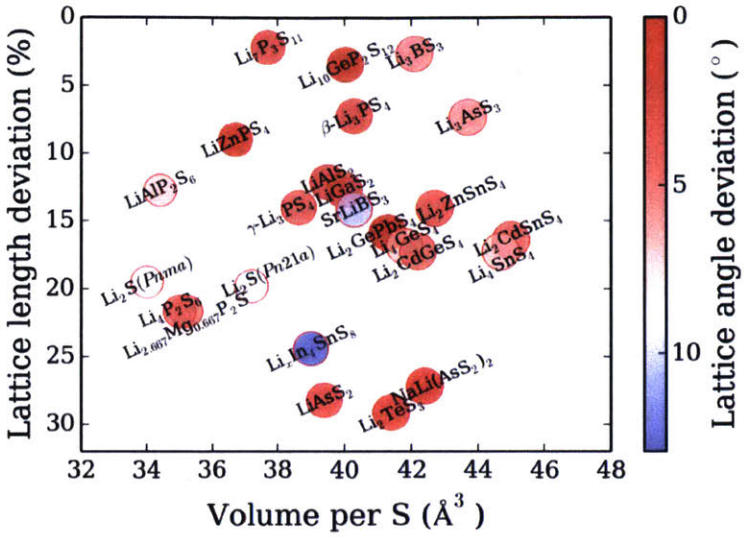

Figure 3-6: **Screened ICSD compounds containing Li and S with similarity to a bcc-like anion framework using the structural matching algorithm.** Compounds with transition metal cations are excluded. The lattice length deviation is defined as $\sigma_l = 1 - \min(a,b,c)/\max(a,b,c)$, and the angle deviation is defined as $\sigma_\theta = \max(|90° - \alpha|, |90° - \beta|, |90° - \gamma|)$, where the a, b, c, α, β, and γ are the conventional unit-cell parameters of the transformed lattice. For an ideal compound with a perfect bcc anion framework $\sigma_l = \sigma_\theta = 0$.

for bcc anion lattice for lithium in O^{2-} and halide lattices, and for other cations including Na^+ or Mg^{2+} [157]. We note that although we predict low activation energies for oxides with bcc oxygen framework, the typically higher activation energy one finds in oxides mainly comes from the much lower frequency with which oxygen takes on a bcc-like arrangement compared to sulfur, and from the smaller volume and reduced polarizability of oxides, which increases the electrostatic interactions between the migrating ion and the other cations.

It is worth noting that there exist a few examples of non-bcc type anion frameworks that also accommodate a network composed entirely of tetrahedral sites for the mobile cations. Such frameworks can be found in the crystal structures of ionic conductors including the argyrodite-type Li_7PS_6 and its halide-substituted derivatives Li_6PS_5X (X=Cl, Br, I)[21], and a very recently reported sodium conductor[43, 139] cubic-Na_3PS_4, which exhibit good

ionic conductivities close to 1 mS cm^{-1} at room temperature. These structures' frameworks cannot be closely matched to a bcc, fcc, or hcp sublattice, but the underlying mechanism for cation migration through the percolating face-shared tetrahedral sites with low activation energy is fundamentally very similar to the bcc-type superionic conductors.

3.5 Conclusions

In this chapter, we investigated the critical influences of the anion-host matrix on the ionic conductivity of solid-state Li-ion conductors. A novel descriptor emerges from these findings: anion sublattices with bcc-like frameworks are superior for Li-ion diffusion leading to a lower activation barrier than in other close-packed frameworks. The bcc anion framework allows the Li ions to migrate within a network of interconnected tetrahedral sites possessing equivalent energies. This feature is found in recently synthesized superionic Li-ion conductors such as $Li_{10}GeP_2S_{12}$ and $Li_7P_3S_{11}$. This new insight has predictive power and can serve as valuable design guidelines for developing fast ion-conducting materials with improved properties, as well as for further searches for new types of Li-ion conductor materials.

3.6 Computational details

3.6.1 Crystal structure analysis

In order to compare structural features between materials, we develop an algorithm to identify similar crystal structures and substructures. The algorithm is in principle similar to previously reported affine mapping techniques[54, 15], and implemented in pymatgen[110]. The algorithm finds an affine mapping between two structures that exactly matches their

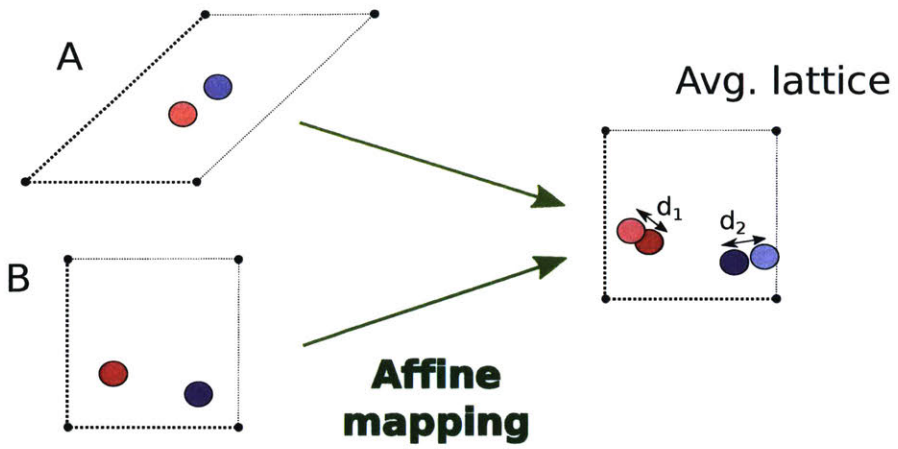

Figure 3-7: **Computing structural similarity.** 2d schematic of the mapping algorithm. The two input structures A and B are mapped via affine transformations onto a lattice generated by the average of the two lattice parameters, while minimizing the RMS distance (of d_1 and d_2) between the sites. The affine transformations are generated to map each lattice exactly onto the target lattice, leaving a translational degree of freedom to align the sites.

periodicities, and minimizes the RMS distance between sites in each structure. Only affine mappings that preserve lattice angles and lengths to within specified tolerances are considered. Structures are considered equivalent if the maximum distance between sites is below a maximum tolerance. When the two structures contain differing numbers of sites, affine mappings to supercells of the smaller structure are also considered. A schematic of the mapping is shown in figure 3-7.

In order to compute the distortion of the sulfur sublattice in the conductor materials, we find the affine transformation that maps supercells of the ideal bcc, fcc, and hcp lattices onto the anion sublattice of the conductor crystal structure, and apply the inverse of this affine transformation onto the conventional cell of the sulfur sublattice. We also report the rms distance of the computed mapping.

To calculate the structural mappings shown in figure 3-1 between the anion lattice and the ideal bcc, fcc, and hcp configurations, we apply the matching algorithm described with

supercell lattice vector length tolerances of 5%, supercell lattice angle tolerances of 3°, and rms atomic displacements of $0.3(\frac{V}{n})^{\frac{1}{3}}$, where V/n is the volume of the structure normalized by the number of atoms.

For the results of the ICSD screening, shown in figure 3-6, a looser mapping tolerance of supercell lattice vector length tolerances of 20%, supercell lattice angle tolerances of 5° were used. With these tolerances, it is possible that a structure matches to more than one framework type, for example allowing the hcp lattices of γ-Li_3PS_4 and Li_4GeS_4 to map to a bcc sublattice, albeit with relatively large lattice length deviations.

3.6.2 Li-ion migration barrier calculations

Density functional theory based on the Perdew-Burke-Ernzerhof (PBE) generalized gradient approximation[115] with interactions between ion cores and valence electrons described by the projector augmented wave (PAW) method[10] as implemented in the VASP package[76] was employed in the present work. The VASP pseudopotential set of Li (PAW_PBE Li 17Jan2003), S (PAW_PBE S 17Jan2003), P (PAW_PBE P 17Jan2003), Ge (PAW_PBE Ge 05Jan2001), Si (PAW_PBE Si 05Jan2001) and Sn (PAW_PBE Sn_d 06Sep2000) was used. Activation barriers for a Li-ion in sulfur bcc/fcc/hcp lattices were calculated using the climbing-image nudged elastic band method (CI-NEB)[46] in a large supercell comprising $3 \times 3 \times 3$ conventional unit-cells to minimize the interaction between the periodic images. A $2 \times 2 \times 2$ k-point grid was used and the cutoff of the kinetic energy was set to 500 eV for all CI-NEB calculations. The supercells containing excess electrons were compensated with a uniform background charge. All S atoms were fixed and only the migration Li atom is allowed to relax. The calculated charge distribution and the Li-ion migration barrier in

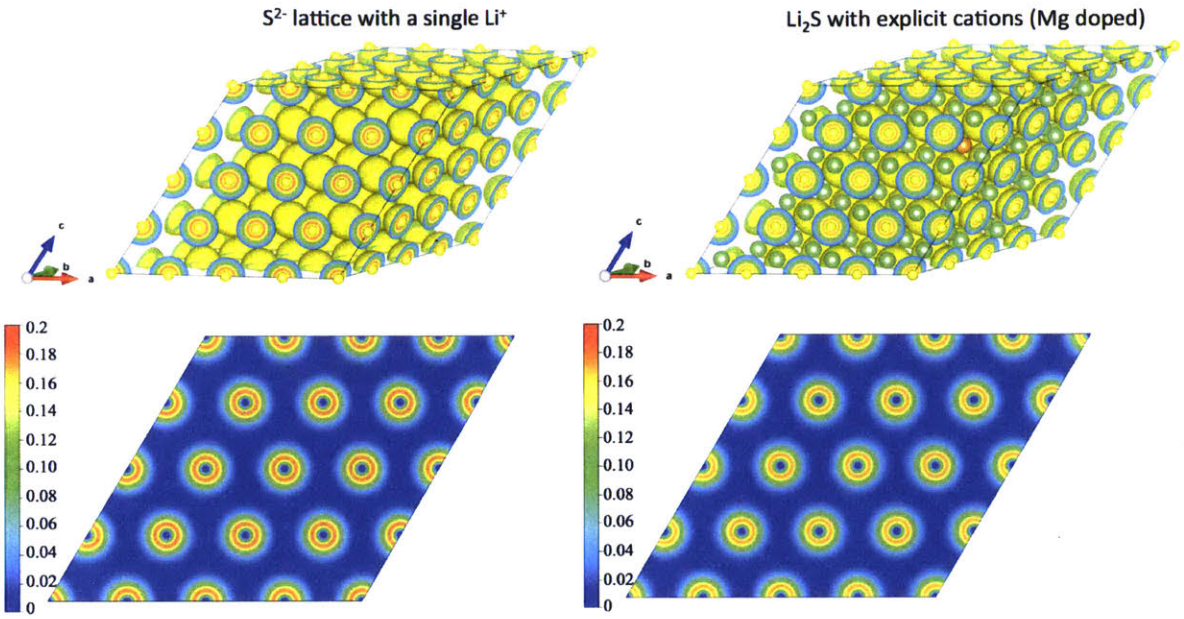

Figure 3-8: **Charge density of framework with compensating background charge.**

the S^{2-} supercells with a single Li^{+} are in good agreement to those from calculations with explicit cations (Figures 3-8 and 3-9).

To evaluate the validity of the approximations made in these barrier calculations, we compare the charge density of a charge-compensated structure with that of one containing explicit cations in figure 3-8. Because of the low electronegativity of the Li-ions, they give up all of their charge to the sulfur framework and do not strongly effect the charge density.

We also compare the resulting activation energies from the NEB calculation in the charge compensated and explicit case in 3-9. The calculated activation energies are in very close agreement, though there is a small effect of interaction with neighboring Li in the shape of the barrier. Nevertheless, these discrepancies are small compared to the differences obtained between the different anion lattices investigated in this chapter.

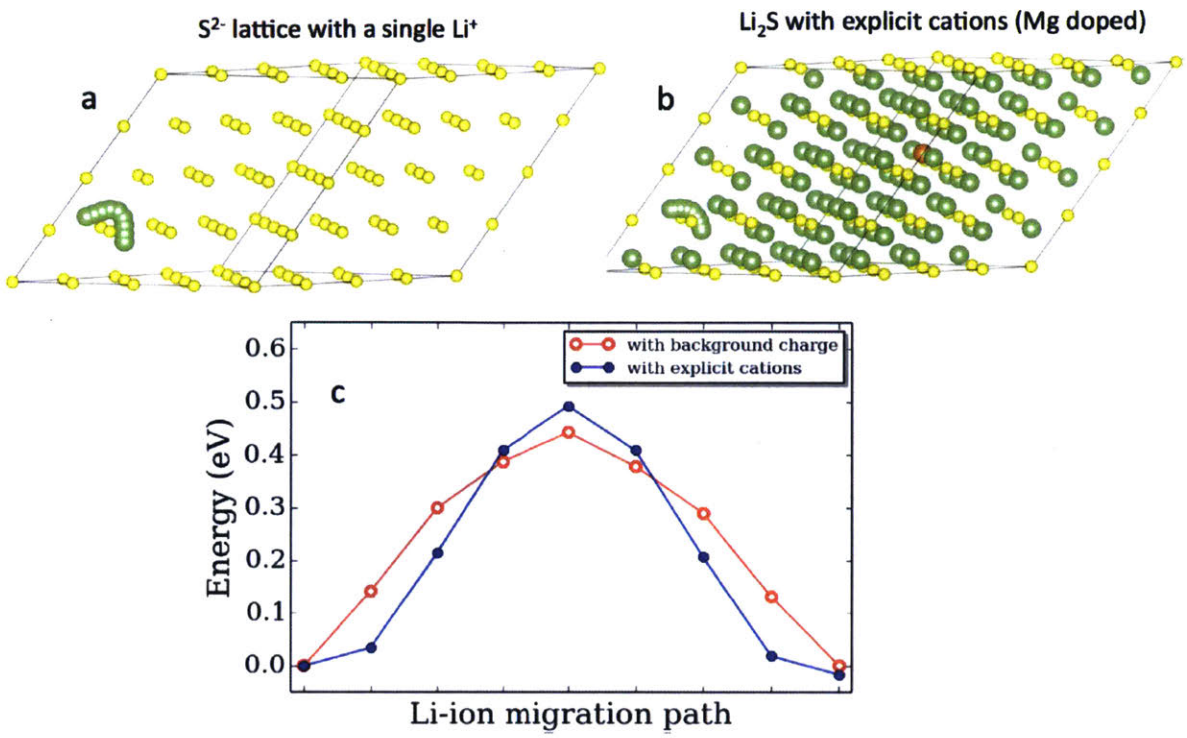

Figure 3-9: **Comparison of charge compensated NEB with explicit cations.**

3.6.3 Li-ion probability density calculations

The lithium ionic probability densities (IPD) were calculated from the atom trajectories monitored during the ab initio molecular dynamics (AIMD) simulations. The simulations were taken on the canonical ensemble with a time step of 2 femtoseconds, with simulations lasting 200 picoseconds for statistical analysis. A gamma-point-only sampling of k-space and a lower plane-wave energy cutoff of 280 eV was used for all AIMD simulations. Details of the AIMD simulation process can be found in previous works[110, 95]. The IPD values within a structure were calculated by subdividing the supercell into a grid of cubic cells with an edge length of 0.2 Åand counting the number of time steps for which each cell is occupied by a Li-ion. The total ionic probability density $\int_{\Omega} P_i = \frac{N}{\Omega}$, where N is the number of Li ions in the unit-cell and is the volume of the unit-cell. Li vacancies are introduced in calculations

of Li_2S and Li_4GeS_4 (6% and 9% of the Li ions are removed from the supercell of Li_2S and Li_4GeS_4, respectively), as stoichiometric Li_2S and Li_4GeS_4 do not show significant Li diffusion and a converged AIMD simulation requires much longer simulation time.

Chapter 4

Engineering of a new bcc ionic conductor: $Li_{1+2x}Zn_{1-x}PS_4$

The structural analyses performed in the previous chapter showed that that a body-centered-cubic (bcc) anion arrangement leads to high ionic conductivity in a number of fast lithium-ion conducting materials[157]. Using this bcc framework as a screening criterion reveals a number of existing materials that match closely to this framework (Figure 3-6). The majority of these close-to-bcc structures are known solid electrolytes, but we also find that the $I\bar{4}$ material $LiZnPS_4$ contains a bcc framework and has the potential for very high ionic conductivity. In this section, we apply ab initio computational techniques to investigate in detail the ionic conductivity and defect properties of this material.

We find that while the stoichiometric structure has poor ionic conductivity, engineering of its composition to introduce interstitial lithium defects is able to exploit the low migration barrier of the bcc anion structure. DFT calculations predict a solid-solution regime

extending to $x = 0.5$ in $Li_{1+2x}Zn_{1-x}PS_4$, and yield a new ionic conductor with exceptionally high lithium-ion conductivity, potentially exceeding 50 mS cm^{-1} at room temperature. We apply ab initio molecular dynamics (AIMD) simulations to probe its conductivity, and nudged elastic band simulations to investigate the transport mechanisms in greater detail. To investigate the defect solubility and therefore the feasibility of experimentally obtaining off-stoichiometric compositions in this structure, we compute the finite-temperature phase diagram using cluster expansion Monte Carlo and frozen phonon calculations to capture the effects of configurational and vibrational entropy respectively.

4.1 Crystal structure analysis

The crystal structure of $LiZnPS_4$ has previously been characterized,[63] but to the best of our knowledge it has never been studied in the context of ionic conduction. It can be described as two alternating layers of corner sharing sulfur tetrahedra perpendicular to the c-axis (Figure 4-1a). In the stoichiometric structure, one layer is half occupied by phosphorus (P layer) and the other contains an ordered arrangement of Li and Zn atoms (Zn layer). Using an affine-mapping transformation as implemented in the pymatgen software package[110] we match the sulfur sublattice to a body centered tetragonal (bct) framework. This affine mapping transforms the LZPS lattice exactly onto lattice points belonging to the bct lattice, while minimizing the root-mean-square distance between the atom positions in the two lattices. We find that the S^{2-} sublattice in LZPS is very close to bcc, having an a/c ratio of 0.9 and with sulfur atoms each displaced only 0.29 Å from their ideal positions (Figure 4-2). This compares favorably with the crystal structure of other known lithium

superionic conductors.[157]

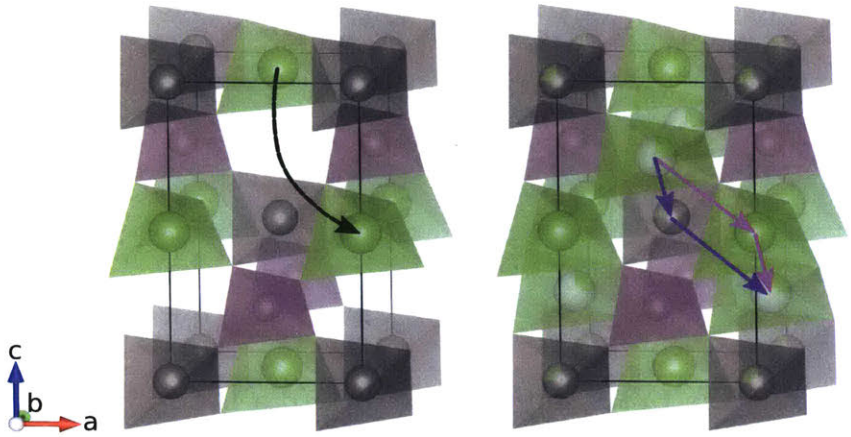

Figure 4-1: **Structures of a) ordered $LiZnPS_4$, and b) off-stoichiometric disordered $Li_{1+2x}Zn_{1-x}PS_4$.** Purple PS_4, grey ZnS_4, and green LiS_4 tetrahedra. When the Li concentration is increased, Li^+-ions begin to occupy vacant tetrahedral sites in the P layer, compensated by substitution of a Li^+ for a nearby Zn^{2+}. The primary transport mechanisms of each structure are shown schematically with an arrow indicating the atom motion. Each color represents a separate mechanism

In addition to the stoichiometric structure, we are interested in studying the conduction properties of the Li-rich compositions of $Li_{1+2x}Zn_{1-x}PS_4$ with $x > 0$. As excess lithium is introduced, we expect lithium ions to occupy vacant sites in the P layer (which we will refer to as Li^+-interstitials) since there are no remaining non-edge-sharing sites available in the Zn layer (Figure 4-1b). This is confirmed by DFT calculations of the alternative interstitial configurations; Li-ions initialized in the edge sharing tetrahedral site in the Zn-layer or in the octahedral site between the Zn and P layers both relax to the corner-sharing tetrahedral site in the P layer. Preferred Li-occupancy of the P layer is also shown by the Li-ion probability density calculated from AIMD simulations (Figure 4-4). Because of the relatively small size of the PS_4 tetrahedron, the P layer is slightly thinner than the Zn layer and these remaining tetrahedral sites are high energy in comparison to the standard Li_{Li}-sites. Each interstitial

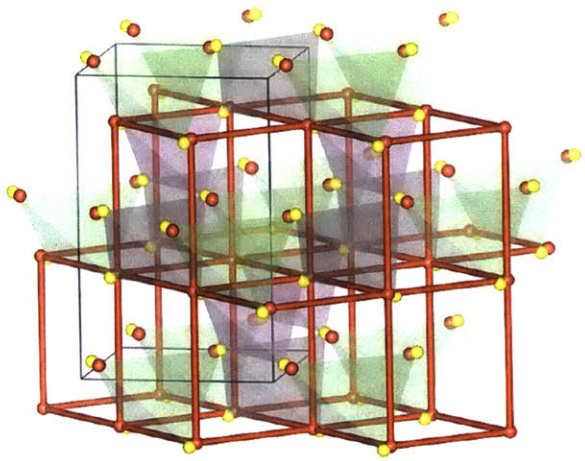

Figure 4-2: **Mapping the LZPS sulfur framework to a bcc sublattice.** Ideal body-centered-tetragonal (bct) lattice (red) with an a/c ratio of 0.90 overlaid on the sulfur framework (yellow) of $Li_{1+2x}Zn_{1-x}PS_4$. Transparent tetrahedra are: PS_4 (purple), ZnS_4 (grey), and LiS_4 (green). The sulfur atoms are each displaced 0.29 Å from the idealized bct position

Li^+ is charge compensated by substitution of a nearby Zn^{2+} atom with Li^+. Our calculations will show that this occupancy is crucial for improving ionic transport.

4.2 Ionic conductivity

The bcc anion sublattice of LZPS suggests that it will have high lithium ion mobility, which we confirm using ab initio molecular dynamics simulations (AIMD), and nudged elastic band (NEB) calculations, both using DFT to calculate energies and forces. The presence of defects can have very significant effects on ionic transport; we calculate the diffusivity and ionic conductivity of the pristine structure and at a range of defect concentrations on $Li_{1+2x}Zn_{1-x}PS_4$, from $x = 0$ to $x = 0.75$. This compositional range was selected for the expected high mobility and low defect energy of this interstitial defect. All DFT calculations are use the Perdew-Burke-Ernzerhof (PBE) generalized gradient approximations[115] using the projector augmented wave (PAW) method[10] as implemented in the Vienna Ab initio

Simulation Package (VASP).[76] Pseudopotentials used were PAW_PBE Zn 06Sep2000, PAW_PBE Li 17Jan2003, PAW_PBE P 17Jan2003, and PAW_PBE S 17Jan2003. For AIMD and NEB calculations, the energy cutoff was 280 eV.

4.2.1 Ab initio molecular dynamics

For these AIMD calculations, an NVT ensemble was simulated using a time step of 2 fs and a Nosé-Hoover thermostat[105] with a period of 80 fs. A minimal Γ-point only k-point grid was used, and calculations were non-spin-polarized. The lowest energy atomic arrangement on a $2 \times 2 \times 1$ supercell of the conventional cell (Figure 4-1) was simulated for each composition. AIMD simulations were run every 100 K between 400 and 900 K for 240,000 time steps (480 ps). Results of the simulations are shown in Figure 4-3, and calculated diffusivities, activation energies, and extrapolated room temperature conductivities in Table 4.1. For the stoichiometric structure $LiZnPS_4$, diffusion calculations below 700 K did not converge due to the low amount of atomic motion in the simulations.

Table 4.1: **Calculated activation energy (E_a) and extrapolated room temperature (RT) conductivity for $Li_{1+2x}Zn_{1-x}PS_4$ from MD simulations.**

Composition	E_a / eV	RT Conductivity / mS cm^{-1}
$LiZnPS_4$	1.07	1.81×10^{-9}
$Li_{1.25}Zn_{0.875}PS_4$	0.252	3.44
$Li_{1.5}Zn_{0.75}PS_4$	0.181	27.7
$Li_2Zn_{0.5}PS_4$	0.165	53.8
$Li_{2.5}Zn_{0.25}PS_4$	0.140	114

The AIMD simulations show a very strong trend of increasing conductivity with lithium-ion concentration, with extrapolated room temperature conductivity increasing by ten orders of magnitude between the $x = 0$ and $x = 0.75$ compositions. The maximum RT conductivity obtained, 114 mS cm^{-1} at $Li_{2.5}Zn_{0.25}PS_4$ is significantly higher than that of any known

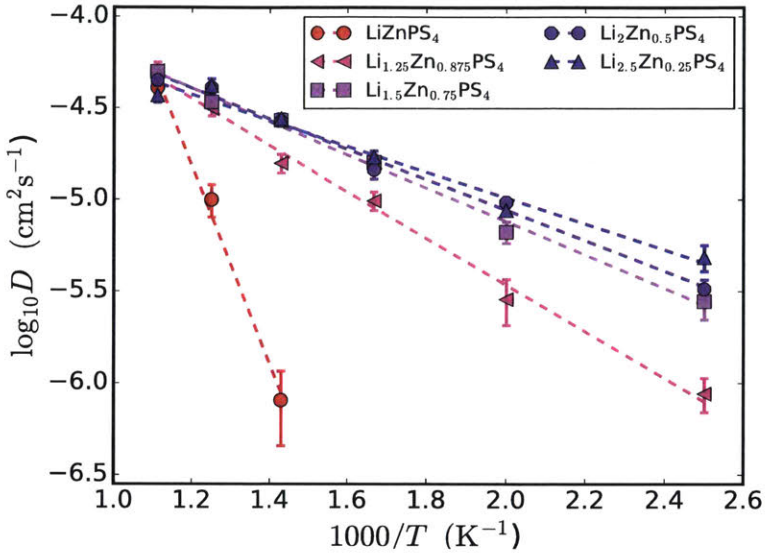

Figure 4-3: **Arrhenius plot of Li-ion diffusivity in $Li_{1+2x}Zn_{1-x}PS_4$ from AIMD simulations.** Dotted lines are least-squares fits to the data.

solid Li-ion conductor. While the stoichiometric compound has a very high activation energy, reflecting the need to thermally create carriers, as soon as Li-excess is introduced the activation energy drops to the low values expected for the bcc anion framework. The mechanisms of this diffusion process and the feasibility of attaining these compositions, will be investigated in the next sections.

4.2.2 Nudged elastic band calculations

To better understand the transport mechanisms in this material, we performed nudged elastic band (NEB)[62] calculations of the vacancy migration barrier and cooperative migration in $Li_{10}Zn_7P_8S_{32}$, along the ion paths shown schematically in Figure 4-1. NEB calculations determine the migration energy required to reach the transition state, which is closely related to the activation energy for transport in the Arrhenius relation of the ionic conductivity.

We distinguish three mechanisms: the *vacancy migration* mechanism (Figure 4-1a) tracks

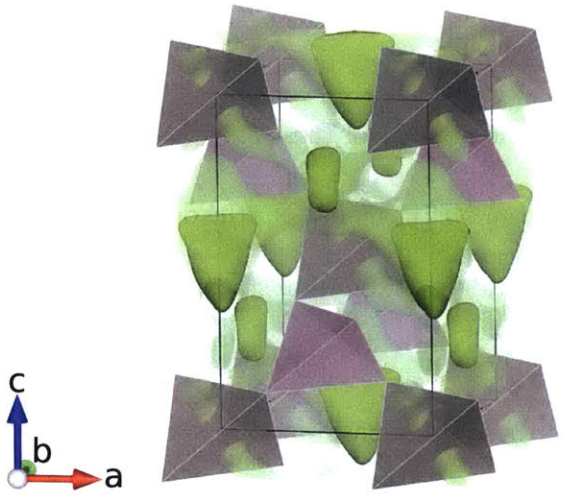

Figure 4-4: **Representative Li-ion probability density isosurfaces in LZPS.** Data calculated from AIMD of $Li_{1.25}Zn_{0.875}PS_4$ at 800 K and projected onto the conventional cell. Since there is some Li_{Zn} occupancy, some diffusion occurs through the Zn site (grey tetrahedra). The high-probability regions (dark green) correspond to the tetrahedral lithium sites shown in Figure 4-1b. The lower probability (lighter transparent green) regions show the Li-ion conducting pathways through the crystal structure.

the motion of a Li-vacancy from one Zn layer to another, with a Li-ion passing through the empty tetrahedral site in the phosphorus layer; in *Li^+-interstitial migration*, there are two relevant cooperative mechanisms (Figure 4-1b) that result in net motion of one Li^+-interstitial moving between P layers. Because of the difference in Li-site energy between the P and Zn layers, lithium vacancies in the Zn layer are unstable and migration must start and end with full occupancy of the Zn layer. In both cooperative pathways, an interstitial Li-ion moves from the P to Zn layer, displacing a second Li-ion that moves to a vacant site in the P layer. Under Li-excess, some of the zinc atoms in the stoichiometric structure are replaced by lithium, so this cooperative mechanism can occur either through a Li_{Li}-site (purple arrow), or through a Li_{Zn} site (blue arrow). These sites are structurally very similar, but differ in the occupancy of their in-layer tetrahedral neighbors: Zn for the Li_{Li} site, Li

for the Li_{Zn} site. Whereas the vacancy migration and cooperative path through the Li_{Li}-site are percolating 3d conduction pathways, percolation of the Li_{Zn} pathway requires a high lithium content to increase the number of these sites.

For the vacancy mechanism NEB calculation, the defect charge is compensated by a uniform background charge to retain the oxidation states of the pristine structure. The calculations for the cooperative mechanisms use a structure with the composition $Li_{1.25}Zn_{0.875}PS_4$. The calculated energies of these three pathways are shown in Figure 4-5.

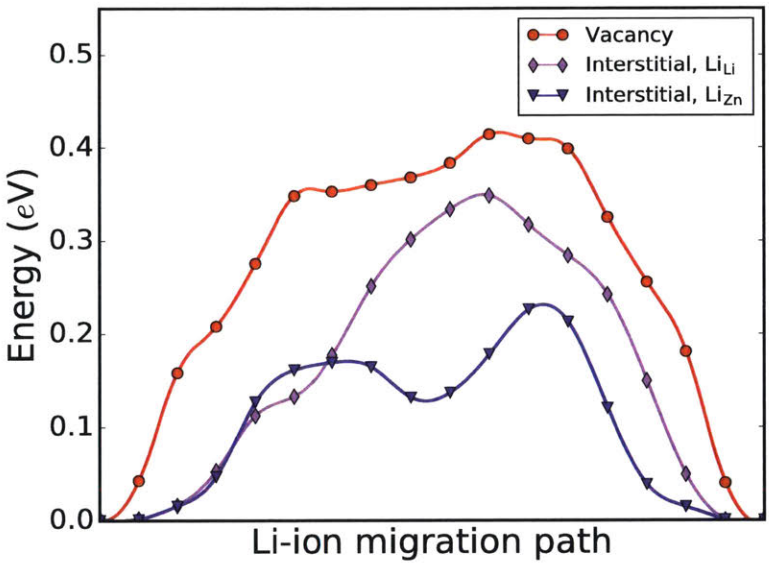

Figure 4-5: **NEB barriers for Li-defect migration in LZPS.** Energy along the minimal energy pathway for a charge-compensated vacancy defect (red) and an interstitial with cooperative motion (blue, through Li_{Zn}, and purple, through Li_{Li}) in $Li_{1.25}Zn_{0.875}PS_4$.

The vacancy migration barrier is calculated to be 414 meV, much higher than that of interstitial lithium through the Li_{Zn} site, 226 meV, and the interstitial path through the Li_{Li} site calculated to be 358 meV. At room temperature the difference between the high and low barriers corresponds approximately to three orders of magnitude in lithium diffusivity, emphasizing the importance of achieving interstitial rather than vacancy defects

for conductivity.

The vacancy migration barrier (414 meV) is, however, still much lower than the activation energy calculated from AIMD in stoichiometric $LiZnPS_4$ (1070 meV). This is to be expected as there are no extrinsic defects at the stoichiometric composition and their formation energy will contribute significantly to the measured activation energy. The large increase in the AIMD calculated conductivity with increasing lithium concentration (Table 4.1) is due to a combination of 1) the introduction of extrinsic defects, 2) the lower energy barrier of the cooperative Li migration, and 3) an increase in the number of Li_{Zn} sites, allowing percolation by this lower energy mechanism. It is clear that LZPS can achieve a very high conductivity if high enough off-stoichiometry can be achieved. In the next section we use ab initio phase diagram methods which investigate the solubility limits in LZPS.

4.3 Defect solubility

4.3.1 Cluster expansion

Because of the high conductivity of the interstitial defect in $Li_{1+2x}Zn_{1-x}PS_4$, it is particularly important to understand its solubility limit. We calculate the finite-temperature pseudo-binary phase diagram between the $I\bar{4}$ $LiZnPS_4$ and the $Pmn2_1$ phase of γ-Li_3PS_4 [48], the ground state structure at the Li_3PS_4 composition, to determine the accessible compositional range of this solid solution. Two high temperature polymorphs of Li_3PS_4, β and α, are also observed in this system,[48] but the DFT enthalpy and phonon free energies predict a transition from the γ to β-phase above 850 K, and so inclusion of these polymorphs would have a minimal effect on the calculated defect solubility of $Li_{1+2x}Zn_{1-x}PS_4$ over the

considered temperature range of 0 to 1000 K. We confirm that the pseudo-binary equilibrium is the relevant decomposition along this tieline (i.e. that no other phases, or lower energy equilibrium of other phases, exists in the quaternary phase diagram between these end members) by calculating the energies of all known compounds in the Li-Zn-P-S chemical space and those generated by applying a data-mined ionic substitution algorithm[40] to known crystal structures in other chemical systems using a probability threshold of 10^{-4}. From these energies, we construct the ground state (0 K) phase diagram (Figure 4-6) using the convex hull implementation of the pymatgen software package.[110] This methodology finds all compositions that cannot lower their energy by decomposing into any combination of other phases. From these calculations, we find that the end members, $LiZnPS_4$ and γ-Li_3PS_4, are indeed stable, and that compositions between these phases decompose to a mixture of these end members at 0 K.

Cluster expansions represent the energy of a periodic arrangement of atoms as a function of their local environments, and are a well-established techniques for calculating configurational entropy for phase diagrams.[125, 127, 30, 18, 112, 149] The cluster expansion methodology developed for this work is described in further detail in section 4.6.1. Total energy calculations for the phase diagram and for fitting the cluster expansion use an energy cutoff of 520 eV, a k-point grid containing at least $1000/n_{\text{atoms}}$, and are spin-polarized for compatibility with previous total energy calculations and phase diagrams.[56] For both the γ-Li_3PS_4 and $Li_{1+2x}Zn_{1-x}PS_4$ structures we build an energy model consisting of a short range cluster expansion containing point terms, pair terms to 8 Å, and triplet terms to 5 Å, and a long range electrostatic component modeling the interactions between ideal charges on each ion (i.e. Li^+, Zn^{2+}, P^{5+}, S^{2-}) parameterized by the relative permittivity. The cluster

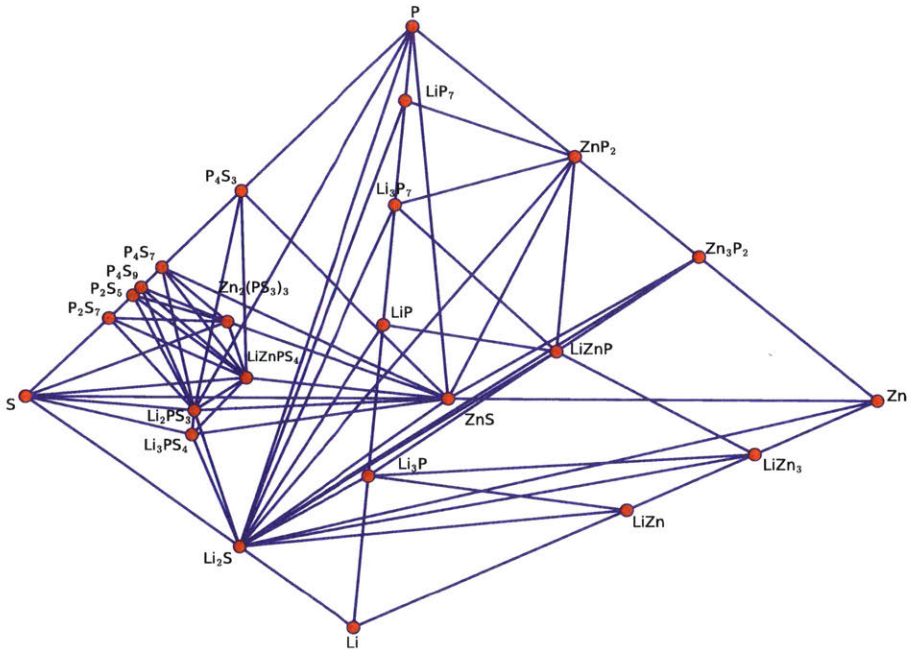

(a)

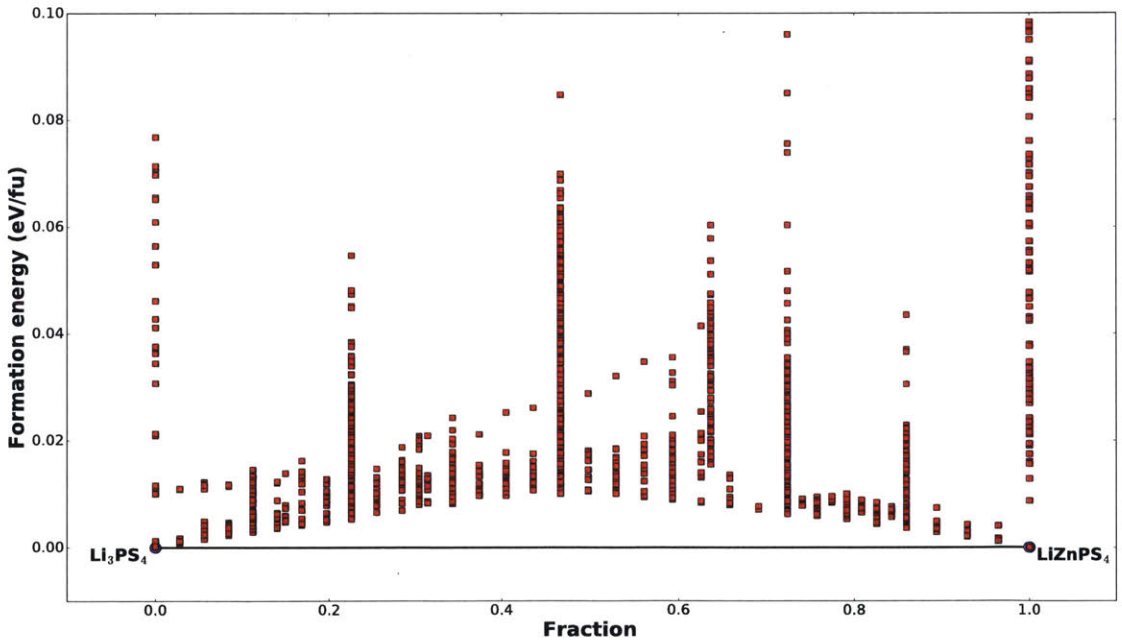

(b)

Figure 4-6: **0K phase diagram of the Li-Zn-P-S system.** a) DFT calculated 0 K phase diagram of the Li-Zn-P-S chemical system. Note the tieline between the $LiZnS_4$ and Li_3PS_4 compositions indicating their coexistence. b) DFT calculated formation energies of calculated structures along the $LiZnS_4$-Li_3PS_4 tieline. These structures were generated either with the cluster expansion Monte Carlo simulation or the ionic substitution algorithm from known materials in other chemical systems.

expansion and long range electrostatic interactions are fit simultaneously to ensure that the electrostatic model captures only the long range effects.

The $I\bar{4}$ structure requires a coupled-cluster expansion[141] with a lattice of Li/Vacancy and another of Li/Zn occupancy, and the $Pmn2_1$ structure a ternary cluster expansion with Li/Zn/Vacancy occupancy on two distinct sites. This model is fit to DFT computed structures using a compressive sensing approach[16, 35, 103] penalizing the L_1-norm of the effective cluster interactions (ECI's, u) according to equation 4.1, in which A is the feature matrix and f the DFT computed structure energies, using the split-Bregman algorithm.[35] The error term weight (μ) was chosen for each lattice to minimize the out-of-sample root mean square error.

$$u = \underset{u}{\operatorname{argmin}} \left\{ \|u\|_1 + \frac{\mu}{2} \|Au - f\|_2^2 \right\} \tag{4.1}$$

The out-of-sample root mean square error of these cluster expansions, as calculated from 5-fold cross validation, was 3.1 meV per formula unit (1.6 meV p.f.u in-sample error; 2 Li/Zn sites and one Li/Vacancy site) for the $I\bar{4}$ lattice, and 3.5 meV p.f.u (2.1 meV p.f.u. in-sample error; 3 sites with Li/Zn/Vacancy occupancy) for the $Pmn2_1$ lattice. These errors are very small on the energy scale of the disordering transformation ($\sim$ 75 meV p.f.u.). We calculate the internal energy as a function of temperature for each of these phases from canonical ensemble (constant composition) Monte Carlo simulations using the Metropolis-Hastings algorithm[39] (see Section 4.6.2) at 33 evenly-spaced compositions between $LiZnPS_4$ and Li_3PS_4. In these calculations, each Monte Carlo cell contains 64 formula units and has lattice vectors of at least 20 Å. Ten million Monte Carlo perturbations (MC steps) were simulated at each temperature after an initial equilibration period of one million MC steps.

Twenty temperatures between 0 K and 1200 K were simulated at each composition, with internal energies at intermediate values computed by reweighting the observed energies from nearby temperatures.[29] Entropies and free energies are obtained from these calculation by thermodynamic integration at each composition from 0 K according to equation 4.2, where C_{p} is the heat capacity, k_{B} Boltzmann's constant, and Ω_{gs} the degeneracy of the ground state structure.

$$S = k_{\mathrm{B}} \log(\Omega_{\mathrm{gs}}) + \int_0^T \frac{C_{\mathrm{p}}}{T}\, dT \tag{4.2}$$

The degeneracy of the ground state is included here because we have confined the system to a specific periodicity and composition, and therefore the ground state entropy of this system is not defined to be 0 at 0 K.

4.3.2 Phonon calculations

The effects of phonons are calculated using the phonopy software package.[143] Because of the large computational expense of these calculations, especially for low symmetry structures, phonon free energy calculations were calculated for x=0, 0.5, and 1 compositions within each lattice, and values for intermediate compositions were interpolated from these calculations. At each of these compositions, the lowest energy configuration on the orthorhombic conventional cell containing 2 formula units was used. The phonon calculation calculated the Hessian matrix for orthorhombic supercells with lattice vectors as close as possible to 20 Å.

The results of the phonon calculations, shown in Table 4.2, show a stabilizing effect on the high-conductivity $I\bar{4}$ structures. To display the effects on relative phase stability more

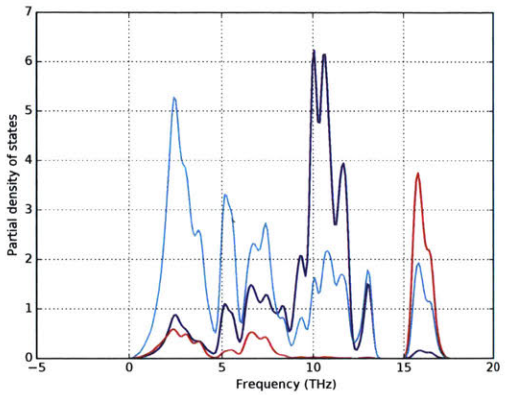

(a)

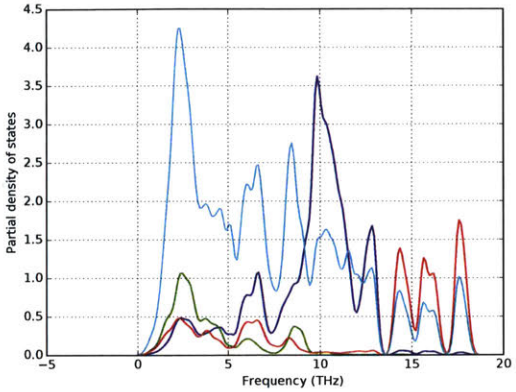

(b)

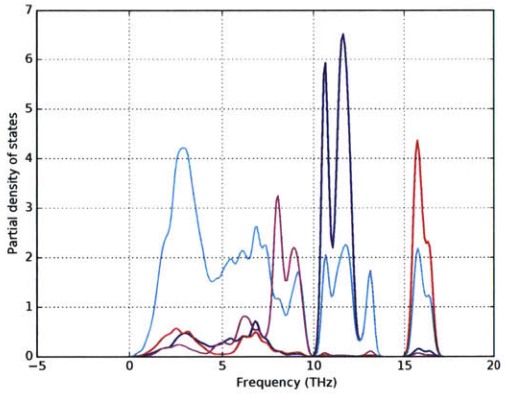

(c)

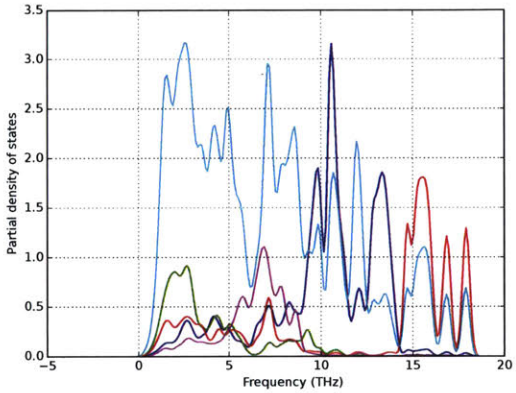

(d)

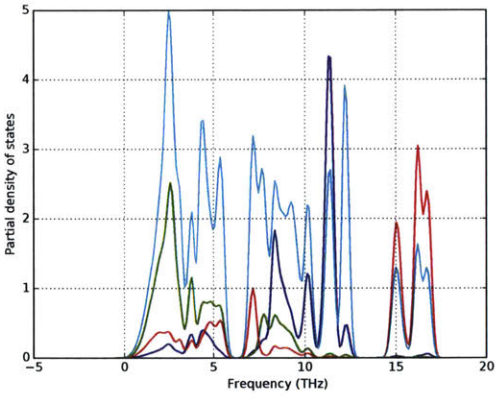

(e)

Figure 4-7: **Phonon density of states for LZPS.** Partial phonon densities of states for a) $Pmn2_1$ Li_3PS_4, b) $Pmn2_1$ $Li_2Zn_{0.5}PS_4$, c) $I\bar{4}$-Li_3PS_4, d) $I\bar{4}$ $Li_2Zn_{0.5}PS_4$, and e) $I\bar{4}$ $LiZnPS_4$. Blue – Li in the Li/Zn layer or in the $Pmn2_1$ structure. Green – Zn. Red – P. Teal – S. Purple – Li in the Li/P layer in the $I\bar{4}$ structure.

easily, we have referenced all thermodynamic values to those of the $I\bar{4}$ phase at $LiZnPS_4$ and of the $Pmn2_1$ phase at Li_3PS_4. While the magnitude of the effect of the phonons is roughly similar to that of the configurational entropy, the phonons have a much greater effect on phase selection in the off-stoichiometric structures - a difference of almost 30 meV p.f.u in phonon free energy between phases at 600 K, compared to a difference of 7.5 meV p.f.u for the configurational entropy. From the projected phonon densities of states (shown in Figure 4-7), this stabilization is seen to be a result of the lower phonon frequency of the lithium in the phosphorus layers relative to the non-defect Li, which is consistent with the low activation energy of the cooperative defect mechanism.

Table 4.2: **0 K enthalpy and free energy contributions from phonons and configurational entropy of LZPS and competing phases.** Data is tabulated for various compositions of the $I\bar{4}$ and $Pmn2_1$ phases at 600 K. All values have been referenced to the $I\bar{4}$ phase at $LiZnPS_4$ and the $Pmn2_1$ phase at Li_3PS_4.

		Composition	
	$LiZnPS_4$	$Li_2Zn_{0.5}PS_4$	Li_3PS_4
0 K Enthalpy (meV / f.u.)			
$I\bar{4}$	0	77.1	90.2
$Pmn2_1$	n/a	73.0	0
Configurational free energy (meV / f.u.)			
$I\bar{4}$	0	-35.2	0
$Pmn2_1$	n/a	-28.7	0
Phonon free energy (meV / f.u.)			
$I\bar{4}$	0	-42.7	9.8
$Pmn2_1$	n/a	-13.9	0

4.3.3 Finite temperature phase diagram

We combine the results of the phonon and cluster expansion Monte Carlo calculations to produce the pseudo-binary phase diagram in Figure 4-8a. For calculation of the phase diagram, configurational free energies are smoothed across compositional space to eliminate artifacts from the finite cell size of the Monte Carlo calculations, and the behavior at the

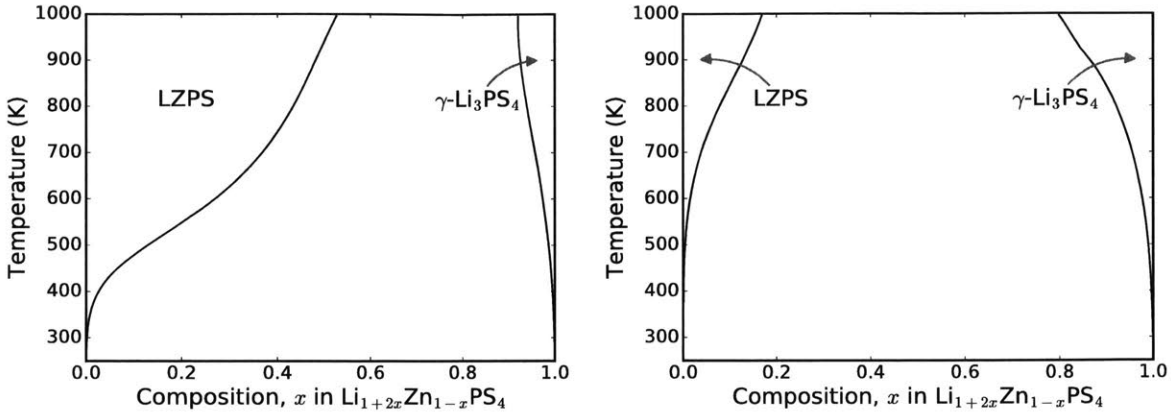

Figure 4-8: **Pseudo-binary phase diagram of the $LiZnPS_4$—γ-Li_3PS_4 system, with and without phonon energies.** a) Phase diagram including phonons. b) Phase diagram excluding phonons. Free energies generated from cluster expansion Monte Carlo and phonon calculations.

extremes of composition (i.e. in the very low-defect limits) is fit to a regular solution model to ensure physically reasonable solubilities at these extrema. The free energies from phonon calculations were added to these configurational free energies, and the solubility limits found by the intersection of the common tangent with the free energy curves at each temperature. The calculated phase diagram shows that the $Li_2Zn_{0.5}PS_4$ ($x = 0.5$) composition is stabilized above ~950 K. Emphasizing the importance of the phonon free energy on the defect solubility, the phase diagram calculated without phonons shows a maximum solubility of only $x = 0.15$ (Figure 4-8b).

4.4 Discussion

LZPS can be added to the short but growing list of ionic conductors with a bcc anion framework and exceptionally high mobility. Computational analysis of this material demon-

strates that the bcc structural framework guarantees that there is a low barrier between the interconnected tetrahedral sites only if the sites themselves have similar energies; the introduction of interstitial Li-ion defects is key to unlocking the high performance of LZPS due to the different character of the Li/Zn and P layers. Analysis of this material via the kinetically resolved activation barrier technique[153] (i.e. by comparing the energy of the transition state to the average of the endpoint energies) yields a barrier of ~150 meV, which would yield exceptionally fast diffusion, and is very much in line with the estimate for the idealized sulfur lattice in reference [157]. By adding interstitial defects, there is at least one atom in the higher energy state at all times that smooths out the energy landscape considerably, evidenced by the lower activation energies both in the NEB (Figure 4-5) and MD calculations (Table 4.1 and Figure 4-3).

The extremely high solubility of the Li-interstitial defect in the LZPS structure can be understood by considering the coupling between the Zn layer and the Li-interstitials. At low temperatures, order on the Zn layer makes the insertion of Li-interstitials energetically unfavorable. At moderate temperatures, above around 400 K across the compositional range, adding lithium interstitials and replacing some Zn with Li allows this layer to disorder more easily, increasing the entropic driving force for interstitial incorporation.

Many thiophosphate conductor materials, in particular those containing metal or metalloid elements, are not stable against pure lithium.[95, 109, 161, 121] Contact with a lithium metal anode may reduce the Zn^{2+} in LZPS and result in electrical conductivity similar to $Li_{10}GeP_2S_{12}$ and related materials. However, $Li_{9.54}Si_{1.74}P_{1.44}S_{11.7}Cl_{0.3}$ has been shown to be effective in combination with a $Li_4Ti_5O_{12}$ anode in a high-rate cell.[71] The more negative formation energy per sulfur atom of ZnS compared to SiS_2[77] suggests that the low voltage

stability limit of Zn-containing sulfides will be $\sim$ 0.5 V lower than Si-containing sulfides. Interfacial stability may alternately be achieved with the use of an electronically insulating anode coating.

LZPS also illustrates the importance of phonon stabilization in ionic conductors. The two competing lattices, based on the $LiZnPS_4$ and γ-Li_3PS_4 structures, have similar configurational entropy and enthalpy for the $Li_2Zn_{0.5}PS_4$ composition (Table 4.2), but the excess phonon free energy is much higher for the LZPS structure with its highly mobile Li sublattice. Our calculations show the typical phenomenon of the effects of phonon free energies being similar in magnitude to those of configurational entropy.[3, 150] The importance of phonons in stabilizing ionically conducting materials has been noted previously in similar materials including $Na_{10}GeP_2S_{12}$ [122, 66] and $Li_7P_3S_{11}$ [19], but here it is especially apparent also in its stark effect on defect solubility.

The calculated migration barriers (Figure 4-5) are significantly lower for the Li interstitial through the Li_{Zn} site, compared to the Li_{Li} site. It is therefore desirable to increase the number of such sites to achieve percolation through the low energy pathway. This can be done either by increasing the Li content through the $Zn^{2+} \rightarrow 2\ Li^{+}$ substitution, as has been investigated here. An alternative method may be by replacing the Zn with a Li atom and charge compensating that substitution by doping on the anion lattice (e.g. $S^{2-} \rightarrow Cl^{-}$) or by doping on the Zn site (e.g. $Zn^{2+} \rightarrow Ga^{3+}$). This would reduce the number of (high energy) lithium interstitials required for the low energy pathway to become percolating, and so higher Li_{Zn} concentrations may be achievable by these means.

4.5 Conclusions

We have applied the recently discovered design criterion of a bcc anion sublattice together with ab initio computational methods to predict a new lithium thiophosphate conductor with a large range of solubility, $Li_{1+2x}Zn_{1-x}PS_4$ ($0 \leq x < 0.5$), and extraordinarily high conductivity. We show that the highly defective compositions on this framework have the potential for the greatest room temperature conductivity of any solid lithium ion conductor, and that the maximum conductivity is limited by the defect solubility. If the solubility range could somehow be extended further to $Li_{2.5}Zn_{0.25}PS_4$ ($x = 0.75$), a conductivity in excess of 100 mS cm^{-1} may be attainable. Even with the $x < 0.5$ limitation, the high defect solubility yields an expected ionic conductivity of 54 mS cm^{-1}, exceeding the performance of current state-of-the-art. The combination of molecular dynamics studies across a range of compositions and detailed mechanistic analysis of lithium ion transport leads to an in-depth understanding of the factors governing ionic diffusion in this new class of materials, as well as identifying pathways to further improve conductivity.

4.6 Methods

4.6.1 Cluster Expansions

Cluster expansions[126] represent configuration-dependent quantities, most commonly the internal energy, of an arrangement of atoms on a lattice by the sum of a finite set of cluster interactions.

$$f(\sigma) = f_0 + \sum_{\alpha} \sum_{s} f_{\alpha s} \Phi_{\alpha s}(\sigma) \tag{4.3}$$

The functions Φ are the cluster functions, which represent the occupancy of each cluster α, which is defined as a subset of sites in the structure. Typically it is assumed that the values of $f_{\alpha s}$ decay rapidly with increasing cluster radii and number of sites, so the system can be well described by considering a small subset of α. This allows accurate models to be fit with reasonably small amounts of training data.

Electrostatic energy in cluster expansions

Cluster expansions were originally used to solve problems concerning magnetic materials (the Ising model), or metallic systems. In both of these cases, the strength of the relevant interactions decays rapidly with cluster radius. In ionic systems, the electrostatic interactions which are inherently longer-range become important to consider. The electrostatic energy between two point charges is given by equation 4.4

$$U_E = \frac{1}{4\pi\epsilon_0} \frac{q_1 q_2}{r_{12}} \tag{4.4}$$

The pairwise nature of these interactions appears to fit nicely into the framework of cluster expansions, and suggests that electrostatics can be taken into consideration by allowing the model to fit this U_E term for each pair of atoms in the structure. Unfortunately, this summation doesn't converge easily with increasing radius r_{12}, and $f_{\alpha s}$ is no longer sparse. This electrostatic part of the crystal energy is well known as the Madelung constant[89], and even for simple systems doesn't even converge in the expanding spheres method. Picking a

maximum cluster radius, therefore, cannot accurately model the electrostatic component of the total energy.

Fortunately, there exist other methods of calculating the Madelung energy of periodic systems. The Ewald summation method [27] partitions the sum into a short range contribution calculated in real space, and a long-range contribution via a Fourier transform in reciprocal space. We add the electrostatic energy to the cluster expansion with the addition of an explicit electrostatic term E_{ewald}

$$f(\boldsymbol{\sigma}) = \frac{1}{\epsilon_r} E_{\text{ewald}} + f_0 + \sum_{\alpha} \sum_{s} f_{\alpha s} \Phi_{\alpha s}(\boldsymbol{\sigma}) \tag{4.5}$$

When fitting the cluster expansion, the relative dielectric constant ϵ_r is fit along with the cluster expansion coefficients $f_{\alpha s}$. It should be noted that E_{ewald} must be calculated for every structure, using the idealized lattice positions of the input structure. For computational efficiency when performing many calculations on the same supercell, E_{ewald} can be decomposed into its pairwise interactions, such that $E_{\text{ewald}} = \mathbf{x}^{\mathbf{T}} M \mathbf{x}$, where $\mathbf{x}$ is a binary vector representing the occupancy of each site.

In practice, the addition of electrostatic interactions is particularly important when fitting cluster expansions involving multiple positive or multiple negatively charged species on the same lattice. With multiple competing attractive and repulsive forces, the best fitting cluster expansions often do not enforce local charge neutrality. Running Monte Carlo simulations to find minimum energy structures without electrostatics often leads to unphysical structures with high electrostatic energy.

4.6.2 Monte Carlo simulation

Determining finite-temperature thermodynamic quantities usually requires computing the probability distribution across possible system configurations. For example, the entropy of a system is given by

$$S = -k_B \sum_i p_i \ln p_i \tag{4.6}$$

The evaluation of this quantity requires a summation over all possible microstates i. For most systems of interest, this number is too large to enumerate directly – for a binary cluster expansion of 100 sites, the number of microstates is over 10^{30}. Instead of integration over the entire distribution, the entropy can be computed for an approximation of this distribution. One method to do this is to use Markov chain Monte Carlo to obtain a sequence of random samples from this distribution. A popular method for this sampling is the Metropolis-Hastings algorithm[94, 39].

For each iteration, the algorithm:

1. Generate a candidate x' by picking from a distribution $g(x'|x_t)$. This function g can be as simple as allowing a change on a single site in a cluster expansion, or in a canonical ensemble a swapping of two sites.

2. Calculate an acceptance ratio, $\alpha = P(x')/P(x_t)$. Though the absolute probabilities cannot be computed, this ratio is calculated simply by $\exp(-\Delta E/k_{\mathrm{B}}T)$.

3. If $\alpha \geq 1$, automatically accept the candidate, else accept the new candidate with probability α.

This algorithm asymptotically reaches the unique stationary distribution, so system averages, including internal energy, approach the exact value.

Chapter 5

Interfacial and chemical compatibility in electrolyte-electrode systems

Development of high conductivity solid state electrolytes for lithium ion batteries has proceeded rapidly in recent years, but incorporating these new materials into high-performing batteries has proven difficult[137, 135]. Interfacial resistance is now the limiting factor in many systems, but the exact mechanisms of this resistance have not been fully explained - in part because experimental evaluation of the interface can be very difficult. Chemical incompatibility, electrochemical reaction, and mechanical issues may all play a role in degrading battery performance. Coating of cathode particles with an oxide barrier layer has been necessary to suppress development of extreme interfacial resistance and enable high-rate cycling[65, 161, 136, 106], but many of these cells still see significant degradation after relatively few cycles. The future of solid-state batteries depends on engineering better interfaces to allow high rate capability and extended cycle life in this new generation of

batteries, but direct experimental investigation is tedious as accessing the interface between two solids is difficult and the reaction layers are often only a small fraction of the total solids. For this reason, a predictive modeling approach that formally includes the chemical and electrochemical driving force is highly valuable.

In this chapter, we develop a computational methodology to examine the thermodynamics of formation of resistive interfacial phases. The results of this model, including the predicted interfacial phase formation, are well correlated with experimental interfacial observations and battery performance. We find that the bulk thermodynamic driving force for reaction between the electrolyte and cathode is a good proxy for interfacial stability, and that this contribution to the reaction energy dominates the effects of interfacial energy. We calculate that thiophosphate electrolytes have especially high reactivity with high voltage cathodes and a narrow electrochemical stability window. We also find that a number of known electrolytes are not inherently stable, but react in situ with the electrode to form passivating but ionically conducting barrier layers. As a reference for experimentalists, we tabulate the stability and expected decomposition products for a wide range of electrolyte, coating, and electrode materials including a number of high-performing combinations that have not yet been attempted experimentally.

We apply our methodology over a broad range of cathode/electrolyte combinations and suggest new strategies for improving device performance. These calculations require only basic thermodynamic data for the electrolytes, cathodes, and possible decomposition products.

To obtain this starting data, we leverage the scalability and transferability of Density Functional Theory (DFT) calculations to augment available experimental values. This en-

ables the examination of a wide range of cathode and electrolyte combinations including materials whose thermodynamic properties have not yet been determined experimentally while retaining the accuracy of experimental data in systems where this data is available.

We find that the chemical composition of electrode and electrolyte phases is the primary determinant of interfacial stability, but that the performance of these interfaces can be improved by engineering systems where the decomposition phases are passivating (electronically insulating) but still ionically conductive. For example, LiPON[165], one of the few commercialized solid electrolytes, is calculated to be unstable against a lithium metal anode but forms an ionically conducting passivation layer in situ. In particular, the choice of anion is the most critical factor determining the high voltage stability limit. When paired with high voltage cathodes, thiophosphate electrolytes have a high driving force for reaction to form ionically insulating barrier layers, explaining the high internal resistance seen experimentally. We also identify a number of potentially high performance cathode/solid-electrolyte combinations which have yet to be attempted experimentally. These results are also useful for suggesting combinations of electrolytes, one stable against the anode and one against the cathode, to widen the effective stability window.

The design of solid-state electrolyte materials is challenging due to the extreme conditions they experience in contact with both the anode and cathode. To evaluate interfacial stability we proceed in two stages. We first evaluate the electrochemical stability of the electrolyte by itself by subjecting it to Li chemical potentials (μ_{Li}) typically observed at the anode or cathode. We then extend this model allowing chemical reaction between the electrolyte and electrodes. All of these calculations consider the reaction energy of the bulk phases as the contribution of the actual interfacial energy is relatively small. For example, considering an

upper bound for the change in surface energy of 0.5 J m^{-2} with an atomically thin interfacial product, the contribution to the total energy remains only ~100 meV per atom, which we will show is small compared to the bulk driving forces in most relevant systems.

5.1 Stability versus lithium potential

High energy density batteries necessarily have anodes and cathodes with very different lithium electrochemical potential. We consider first the effects of subjecting the electrolyte to these extreme lithium potentials, without allowing other reactions between the electrolyte and the anode or cathode material. The stability window is determined by the voltages at which lithium is extracted from the electrolyte to form a Li-deficient decomposition layer between the electrolyte and the cathode (figure 5-1a, anodic stability), and at which lithium is inserted into the electrolyte, reducing another species and forming a Li-reduced decomposition layer (figure 5-1b, cathodic stability).

For each considered electrolyte, we calculate the range of μ_{Li} over which it is stable by constructing the relevant 0 K grand potential phase diagrams. We consider the grand potential Φ, the characteristic state function of the grand canonical ensemble[92], for systems open to Li at applied voltages between 0 V and 7 V vs Li/Li^+ (μ_{Li} between 0 and -7 eV vs Li metal) according to equation 5.1, in which $E[c]$ is the enthalpy and $n_{Li}[c]$ the lithium concentration of composition c, and μ_{Li} the lithium chemical potential. Phase diagrams are constructed using a database of DFT computed bulk energies of materials with crystal structures obtained from the Inorganic Crystal Structure Database (ICSD)[9] and those generated by applying data-mined chemical substitutions[41]. In general, all known

crystalline compounds in a given chemical space are included in this database. Similar datasets can be found online as part of the Materials Project[58].

$$\Phi[c, \mu_{\mathrm{Li}}] = E[c] - n_{\mathrm{Li}}[c]\mu_{\mathrm{Li}} \tag{5.1}$$

For any lithium potential μ_{Li}, we then find the resulting stable structures by computing the lower convex hull of Φ in composition space, similar to the approach taken in earlier work[111]. In general, the convex hull is formed by the set of ground state phases in a composition diagram. For any composition, the lowest energy is achieved by a linear combination of these phases. Compounds that are on the convex hull in Φ-composition space are stable in contact with a lithium reservoir at μ_{Li}, and cannot lower their energy by decomposition or exchange of Li with the reservoir. Known electrolyte materials that DFT calculates to be metastable at 0 K, e.g. $Li_{10}GeP_2S_{12}$, are placed exactly on the convex hull (i.e. their formation energy from the nearby phases is set to 0) for the stability and reaction energy calculations to account for the small changes in free energy when going from 0 K to elevated temperature. For each structure, we find the range of μ_{Li} over which it is present on the convex hull and therefore stable. As a simple example, the stability ranges for common ionic lithium binary materials are shown in figure 5-2. In all of these binary materials, the anion is fully reduced so further reaction with lithium metal cannot occur and they are therefore stable down to 0 V. At voltages above the stability window, lithium is extracted from these materials yielding the oxidized anion, shown schematically in figure 5-1a. These results are in good agreement with the conventional understanding that the halide anions are the most stable at high potential, and materials such as sulfides, nitrides, and phosphides display low

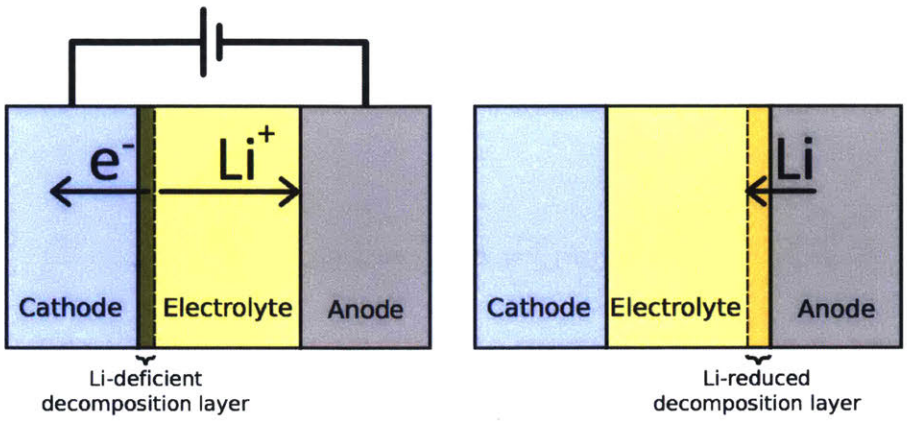

(a) (b)

Figure 5-1: **Schematic of decomposition reactions in a full battery cell.** a) decomposition of the electrolyte at the cathode/electrolyte interface during charging, and b) reduction of the electrolyte by the lithium metal anode

anodic limits.

To evaluate the stability of technologically relevant electrolytes, we construct grand potential phase diagrams for a broad range of known solid-electrolyte chemistries using the pymatgen software package[110]. To obtain bulk energies, we employ DFT within the Projector Augmented Wave (PAW) formalism[10] using the generalized gradient approximation[115] to the exchange-correlation energy as implemented in Vienna ab initio simulation package (VASP)[76] to calculate the formation energy of each electrolyte from the nearest phases present in the NIST-JANAF[90] or Kubaschewski[77] thermochemical tables or from the elements. A cutoff energy of 520 eV and a k-point grid of at least $500/n_{\text{atoms}}$ was used for all calculations. We apply the mixing scheme of [57] to combine generalized gradient approximation (GGA) calculations with and without the rotationally invariant Hubbard (+U) correction[2, 22] to properly treat insulators and metals. The nearest phases are uniquely defined as those that define the Gibbs triangle (the low energy facet) containing the desired

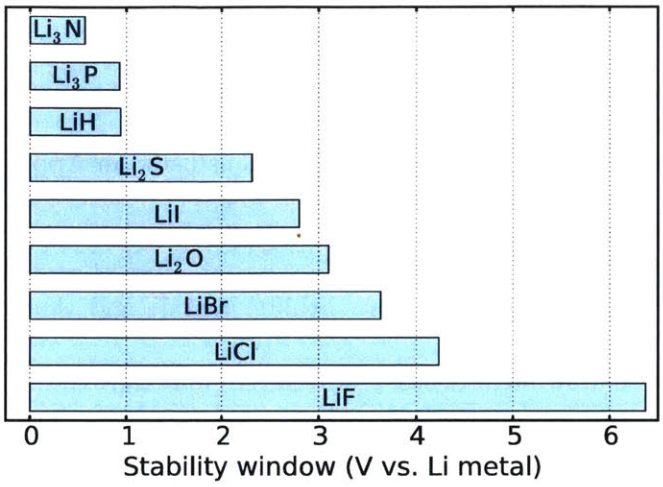

Figure 5-2: **Electrochemical stability ranges of lithium binary compounds.** Where available, these ranges are computed from experimental thermodynamic data.

composition in the phase diagram. This phase diagram is generated using only materials for which we have the experimental formation energy, using the DFT computed energies to determine the convex hull. As an example, to calculate the formation energy of $LiYF_4$, a compound whose formation energy is not present in the experimental tables, we use DFT to calculate the energy of the reaction LiF + YF_3 $\rightarrow$ $LiYF_4$ and add the experimental formation energies of LiF and YF_3. This method results in a more accurate formation energy than computing the reaction from the elements since DFT reaction energies have improved accuracy when considering the energetics of systems in which the oxidation state of ions are unchanged [42]. For Li_3PS_4 and similar materials, where the formation energy of Li_2S is present in the thermochemical tables but P_2S_5 is not, we use DFT to calculate the energy of the reaction 3 Li_2S + 2 P + 5 S $\rightarrow$ 2 Li_3PS_4. When possible, such as for $LiAlO_2$, this strategy results in using the experimentally determined formation energy directly. By using experimental energies as much as possible and supplementing them with DFT calculated formation energies when no thermochemical data is available, we maximize our predictive

capability.

The calculated stability ranges for common solid-electrolyte materials are shown in figure 5-3, with the limiting anodic and cathodic reactions listed in Appendix B as table B.2. In a typical battery, the electrolyte must be stable at lithium potentials between the anode chemical potential (close to 0 eV/atom vs. lithium metal) and that set by the cathode (typically around -4 eV/atom for a layered oxide). We find that the anodic stability is determined primarily by the stability window of the related binary, or in the case of mixed anion materials, by that of the least stable related binary material, e.g. the anodic stability of Li_6PS_5Cl is determined primarily by the stability of Li_2S. This phenomenon is explained by considering the pathway of decomposition first to the Li_nX (n=1, 2, 3, X=anion) binary and resulting phase equilibrium and then dissociation of this binary to extract lithium. According to this two step process, any removal of lithium from the electrolyte must overcome both the formation energy of Li_nX and the energy of mixing with the other binary materials. The energy of mixing widens the electrochemical window over which the electrolyte is stable. In most cases this mixing energy is small and the anodic limit is close to that of the binary, but materials with strongly bound polyanions such as the phosphates and $LiBH_4$ have much wider stability windows since extraction of Li must be accompanied by the dissociation of the polyanion. The exceptions to this rule are those electrolytes that can lose lithium by oxidation of another of their components: e.g. oxidation of Mn^{2+} in Li_2MnBr_4. Figure 5-3 also shows the expected trend of increasing anodic stability with increasing anion electronegativity.

In some cases, the stability windows of the electrolyte do not need to extend to the voltages of the anode and cathode. Li_3PS_4, Li_3PO_4, and LiPON are predicted to be unstable

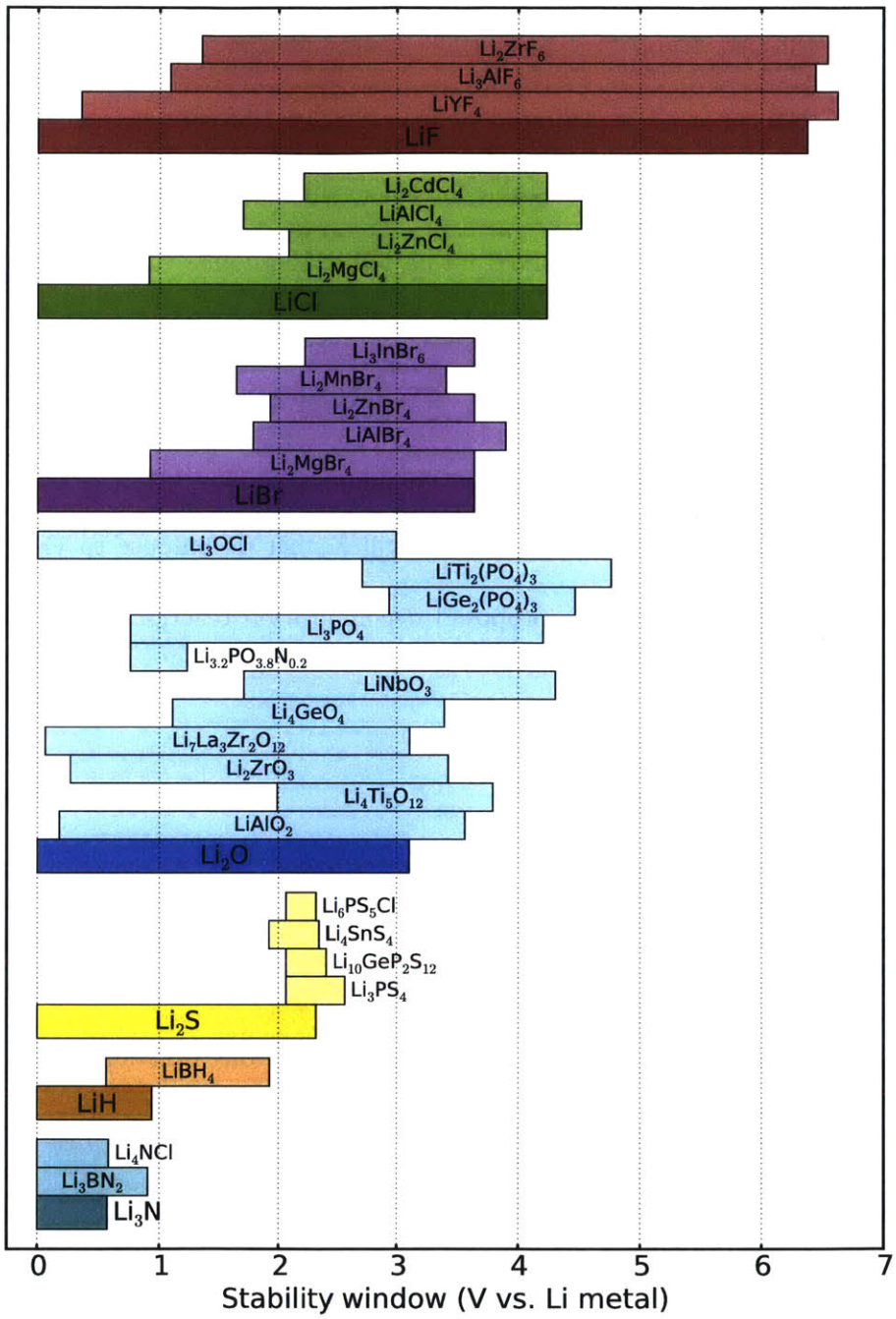

Figure 5-3: **Electrochemical stability ranges of various electrolyte materials grouped by anion.** Corresponding binary stabilities are included for comparison. The high-voltage stability of these materials is determined primarily by the anion. The predicted anodic and cathodic reactions that determine these stability windows are listed in Appendix Table B.2.

against Li-metal from our calculations, but these materials are known experimentally to form a stable interface[165, 86]. Table B.1 shows that at this interface, a layer of Li_2S/Li_2O and Li_3P is expected to form. Li_3P is a known ionic conductor[102], and so can passivate the decomposition reaction and result in a stable interface still able to conduct lithium. In fact, recent experimental work[128] has observed formation of these passivating products at the interface between a LiPON electrolyte and lithium metal anode. Similarly, our calculations predict passivating phases to extend the anodic stability of LiPON to higher voltages. Above 1.2 V, we calculate decomposition to Li_3PO_4 and Li_2PO_2N[130]. This crystalline LiPON phase has a wider voltage stability window, but will further decompose to yield $Li_4P_2O_7$ above 2.75 V, in agreement with the proposed decomposition reaction mechanism of ref. 165.

5.2 Stability in contact with electrodes

The μ_{Li} stability window yields great insight into the performance of an electrolyte in battery systems, but does not consider the more complex reactions that may occur between electrolyte and cathode. At the interface between two phases, there is the possibility of reaction to form an intermediate phase or equilibrium of intermediate phases. We now extend the model to investigate the driving forces for such reactions. Since the reaction can consume arbitrary amounts of either phase, we consider the energy of all possible reactions of the form $xc_a + (1-x)c_b \rightarrow c_{equil}$ where c_a and c_b are the compositions of the two phases in contact, c_{equil} the low energy phase equilibrium determined from the phase diagram, and x a mixing parameter which can vary between 0 and 1. We calculate the reaction of this form

with the highest driving force, given by equation 5.2. In this equation, the function $E_{\text{pd}}[c]$ describes the energy of the ground state structure or phase equilibrium at composition c determined from the phase diagram. Essentially, this approach finds the products that form with the largest driving force when combining two materials.

$$\Delta E[c_a, c_b] = \min_{x \in [0,1]} \{E_{\text{pd}}[xc_a + (1-x)c_b] - xE[c_a] - (1-x)E[c_b]\} \tag{5.2}$$

To illustrate the approach of equation 5.2, we consider first a relatively simple system: an interface of Li_2S with $ZnCl_2$. The calculated quaternary phase diagram is shown in figure 5-4a. The products of the mixing reaction can lie anywhere between Li_2S and $ZnCl_2$. The resulting reaction energies are obtained from the phase diagram, and plot as a function of the mixing parameter x in figure 5-4b. The interface is not thermodynamically stable and will react to form the lower energy equilibrium of 2 LiCl + ZnS with a driving force of 0.27 eV atom^{-1}. In contrast, an interface between LiCl and ZnS is predicted to be thermodynamically stable, which can be immediately seen from the presence of a tieline connecting those phases in figure 5-4a.

In battery conditions, the interface system is open to lithium. We adapt equation 5.2 to account for this by replacing $E_{\text{pd}}[c]$ and $E[c]$ with their corresponding quantities under the grand potential, $\Phi_{\text{pd}}[c, \mu_{\text{Li}}]$ and $\Phi[c, \mu_{\text{Li}}]$. Similar to $E_{\text{pd}}[c]$, $\Phi_{\text{pd}}[c, \mu_{\text{Li}}]$ describes the energy of the ground state structure or phase equilibrium at composition c and lithium chemical potential μ_{Li}, as determined from the grand-potential phase diagram (equation 5.3). We apply the lithium potential determined by the computed average cathode voltage. During

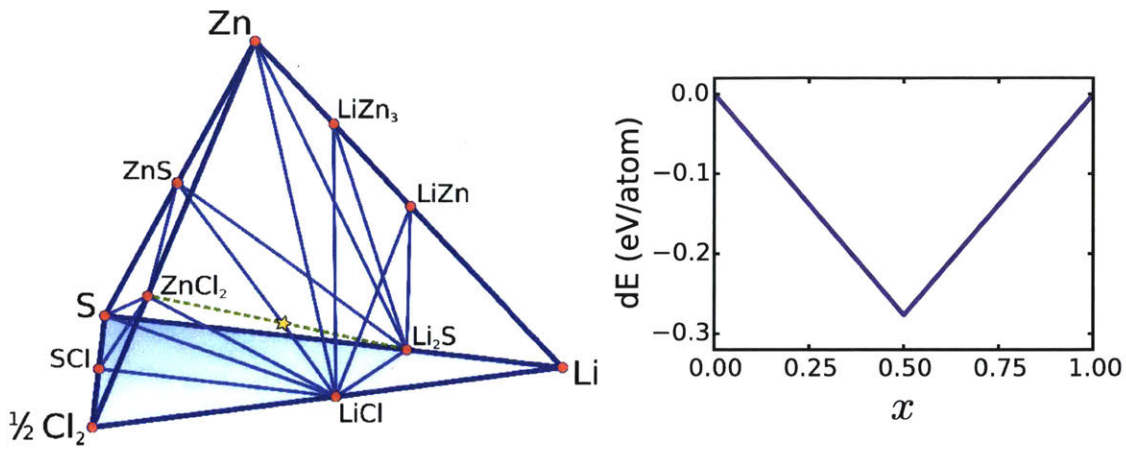

(a) (b)

Figure 5-4: **Schematic of mixing energy calculations.** a) Quaternary Li-Zn-S-Cl phase diagram, with stable phases labeled. The reaction vector between $ZnCl_2$ and Li_2S has been marked with a dotted green line, with a star marking the low energy equilibrium at the intersection of the $ZnCl_2$-Li_2S and LiCl-ZnS tielines. b) Energy of the reaction x $ZnCl_2$ + (1-x) Li_2S $\rightarrow$ c_{equil} as a function of x. The maximum reaction energy is for the complete reaction $ZnCl_2$ + Li_2S $\rightarrow$ 2 LiCl + ZnS.

cycling, the lithium chemical potential is a function of depth of discharge, but this effect on the reaction energy is small. Because the system is open to Li, reaction energies are normalized by the number of non-Li atoms. The resulting expression (equation 5.4) is the change in the grand potential of the interfacial region from allowing the electrolyte to equilibrate with the external lithium potential and react with the cathode and determines the interfacial stability as a function of μ_{Li}.

$$\Phi_{\mathrm{pd}}[c, \mu_{\mathrm{Li}}] = \min_{n_{\mathrm{Li}}} \{E_{\mathrm{pd}}[c + n_{\mathrm{Li}}] - n_{\mathrm{Li}}[c]\mu_{\mathrm{Li}}\} \tag{5.3}$$

$$\begin{aligned}\Delta\Phi[c_{\mathrm{cathode}}, c_{\mathrm{electrolyte}}, \mu_{\mathrm{Li}}] = \min_{x\in[0,1]} \{&\Phi_{\mathrm{pd}}[xc_{\mathrm{cathode}} + (1-x)c_{\mathrm{electrolyte}}, \mu_{\mathrm{Li}}] \\ &- x\Phi[c_{\mathrm{cathode}}, \mu_{\mathrm{Li}}] - (1-x)\Phi[c_{\mathrm{electrolyte}}, \mu_{\mathrm{Li}}]\}\end{aligned} \tag{5.4}$$

The magnitude of $\Delta\Phi$ ultimately governs the thermodynamic stability of the interface, but we can obtain a deeper understanding of the two contributions to this value by comparing it to that of $\Delta\Phi_{\text{no mixing}}$ (equation 5.5), in which we do not allow mixing of the cathode with the electrolyte by enforcing $x = 0$ in equation 5.4. $\Delta\Phi_{\text{no mixing}}$ measures only the reaction energy from equilibration with the external lithium reservoir, and is therefore correlated with the distance between the cathode voltage and the stability range of the electrolyte shown in figure 5-3. By this definition, the magnitude of $\Delta\Phi$ is guaranteed to be at least as large as $\Delta\Phi_{\text{no mixing}}$. In systems where $\Delta\Phi$ and $\Delta\Phi_{\text{no mixing}}$ are approximately equal, the driving force from decomposition arises mainly from extraction or insertion of lithium as opposed to reaction with the other components of the electrode.

$$\Delta\Phi_{\text{no mixing}}[c_{\text{electrolyte}}, \mu_{\text{Li}}] = \Phi_{\text{pd}}[c_{\text{electrolyte}}, \mu_{\text{Li}}] - \Phi[c_{\text{electrolyte}}, \mu_{\text{Li}}] \tag{5.5}$$

Results of calculations of $\Delta\Phi$ and $\Delta\Phi_{\text{no mixing}}$ for various cathode/electrolyte combinations are shown in figure 5-5. The results of these calculations for all of the electrolytes in figure 5-3 are available in Appendix B as figures B-1 to B-7. Generally, electrolyte materials that are predicted to be stable at the cathode voltage show low reaction energies as they come entirely from the mixing of cathode and electrolyte compositions and do not involve redox activity. Thiophosphate materials tend to have high reaction energies, a large part as a result of applying the cathode lithium potential, but also from strong reactions between the PS_4^{3-} groups and oxide cathodes to form PO_4^{3-} groups and transition metal sulfides. The details of these predicted reactions can be found in Appendix B table B.2. For the

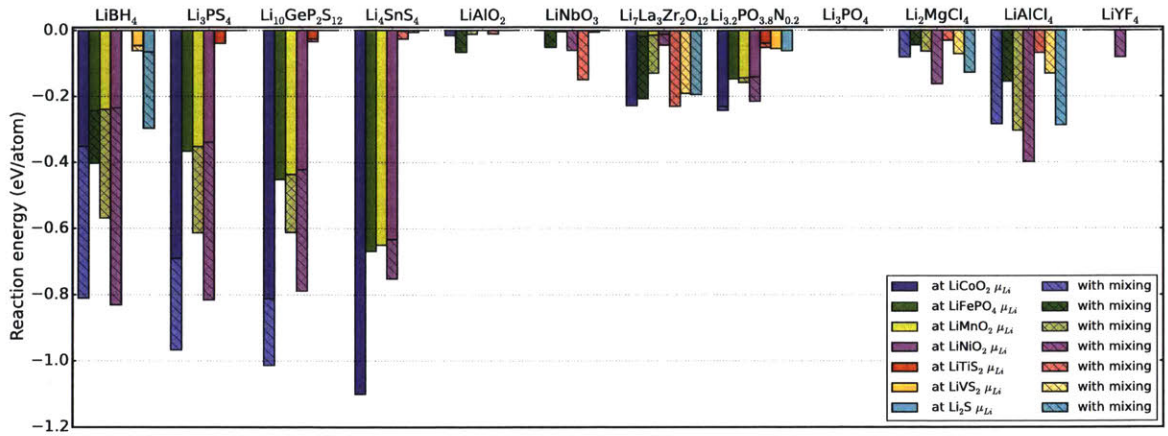

Figure 5-5: **Reaction energies for the interfaces of a selection of cathode and electrolyte combinations.** Calculations apply a lithium electrochemical potential μ_{Li} corresponding to the average cathode voltage. Energies are given both for the energy of the lithium extraction only (no mixing) and for energy of cathode/electrolyte mixing open to lithium. Combinations with decomposition energies close to zero are expected to form stable interfaces. The results of these calculations for all of the electrolytes in figure 5-3 are available in Appendix B as figures B-1 to B-7.

sulfide electrolytes, the largest reaction energies are with the layered $LiCoO_2$ and $LiNiO_2$ due to their high voltage and oxygen chemical potential, but even against $LiFePO_4$ these electrolytes are unstable. In contrast, the oxide materials are considerably more stable.

In systems which have been attempted experimentally, there is good correlation between cycle life and the magnitude of the calculated decomposition energy. Most notably, the stability range for the thiophosphate electrolytes in figure 5-3 are very narrow, with predicted stability only between 2 and 2.5 V vs. Li metal. In these systems, including Li_4SnS_4[123] or $Li_{10}GeP_2S_{12}$[65, 161] electrolytes, oxide coatings on the cathode and high voltage (low μ_{Li}) anode materials, e.g. indium metal, must be used. Additionally, recent work[38] has shown that $Li_{10}GeP_2S_{12}$ can be used as an anode, cathode, and electrolyte in a battery, with carbon added to increase the electrical conductivity of the electrode materials.

A few full-cell configurations have been shown experimentally to require minimal over-

potential and to exhibit good cycle life. A cell utilizing $LiTiS_2$ cathode with Li_2S-P_2S_5 electrolyte [144] has been shown to be relatively stable over many cycles even at elevated temperatures. Our calculations predict only a small driving force for insertion of lithium into the Li_3PS_4 electrolyte (chemically very similar to a Li_2S-P_2S_5 glass) due to the very low voltage of the cathode. Good performance has also been achieved in a wide variety of cells using a LiPON electrolyte[23, 83], which we calculate to be stabilized by the formation of a passivating layer of Li_3PO_4 at high voltages. This is another example of where the decomposition reaction (see table B.1) must be examined for passivating products that retain Li-ion conductivity.

This thermodynamic analysis can also be applied to find mitigating solutions in systems where we predict cathode/electrolyte combinations to react. Typically cathode coatings such as $Li_4Ti_5O_{12}$[106, 136], $LiAlO_2$[161], $LiTaO_3$ [136], or $LiNbO_3$[65, 136] are used at the cathode-electrolyte interface. Figures 5-3 and 5-5 show clearly why such a barrier layer is effective - the stability window of these materials is much wider than any of the sulfide materials, and all of these are stable at oxide cathode voltage.

5.3 Discussion

Interfacial stability is a key problem for solid state battery devices. In this chapter we have developed the foundation of a predictive approach to establish the electrochemical and chemical reactivity between electrodes and electrolytes. Our thermodynamic analysis of electrolyte materials enables an understanding of the processes governing interfacial stability, and is easily scalable to examine electrolyte/electrode combinations across a wide range of

chemical systems. We combine DFT with experimental data to expand the thermodynamic data available for our analysis. The same methods can be applied to purely experimental thermochemistry data in systems where it is available.

Though our methodology does not consider explicitly the kinetics of interfacial layer formation, these are intimately related to the bulk thermodynamics. Typically, solid state reaction rates are limited by either diffusion or nucleation kinetics. For the formation of a thin interfacial layer, the diffusion distance for all reacting species is very small and hence the diffusion time constant is expected to be short. The heterogeneous nucleation rate of the interfacial layer is determined by the free energy of the critical nucleus $\Delta G^* = 16\pi\gamma^3/(3\Delta G^2) \cdot S(\theta)$, where ΔG is the change in energy of the bulk, γ is the interfacial energy and S a shape factor less than 1[118]. Since incoherent interfacial energies do not vary much among ionic solids, for an interface to be kinetically stabilized by a nucleation barrier it must have a small reaction energy.

One major area of battery research is the use of newly developed thiophosphate materials having extremely high lithium conductivity in conjunction with relatively high voltage cathodes. These interfaces have two pathways leading to device failure. First, considering only the lithium chemical potentials experienced by the electrolyte shows that attempting to charge a typical oxide cathode is likely to lead to the formation of a passivating but highly resistive sulfur layer by lithium extraction. Secondly, in contact with an oxide cathode, mixing of the cathode and electrolyte is to be expected due to the high stability of the phosphate anion and Li_3PO_4 phases. This is in good agreement with experimental observation of P and Co transport across the interface in a $LiCoO_2/Li_2S$-P_2S_5 battery[124].

There has been speculation that the interfacial resistance is caused by a space charge

region with Li segregation into the cathode decreasing conductivity[106]. While this segregation is certainly possible and is likely to occur to some extent, it would result in an increase in conductivity by increasing the number of charge carriers. Our calculations suggest that complete breakdown of the electrolyte including oxidation of S^{2-} to form a blocking layer is more likely at the chemical potentials of typical oxide cathode materials. Commonly, cyclic voltammetry is used to evaluate and report electrolyte stability. Somewhat surprisingly given the inherent stability limitations of the sulfide materials, extremely wide stability windows have been reported, in some reports extending as high as 10 V vs. Li metal[65, 129, 119]. This may be caused by a thin layer of oxidized, lithium deficient, electrolyte at the electrode, for example elemental sulfur in systems containing thiophosphate electrolytes. Such an interfacial layer will significantly impede lithium mobility, so CV curves should be augmented by Li transport measurements at these high voltages to confirm electrolyte function under extreme applied potentials.

A significant difficulty in finding a good solid electrolyte is finding one that is stable at both the cathode and anode. From figure 5-3, the $Li_7La_3Zr_2O_{12}$ garnet[100] and $LiAlO_2$ materials meet the stability requirements for high voltage cathodes. Because of its chemical similarity to $LiAlO_2$, ion exchanged Li β''-alumina also shows a wide stability window and with higher room temperature conductivity[11]. Incorporation of these oxide electrolytes into solid state batteries is typically difficult, as many suffer from high grain boundary resistance or require high temperature sintering to obtain good contact with the electrodes. The binary halides have extraordinarily wide stability windows, but ionic conductivity is prohibitively low for all but the lowest power applications unless a second cation is added[33, 132, 20, 88, 160, 68, 69]. Unfortunately, the addition of such a cation typically makes these materials

unstable against reduction by low voltage anodes (figure 5-3).

Cathode coatings improve the performance of high voltage electrolytes by isolating the electrolyte materials from the low lithium potential, and imperfections in the coating allow reactions between cathode and electrolyte that yield passivating and ionically insulating reaction products. Because of this resilience to imperfections, thin coatings of lower conductivity materials can be used. Coating of the anode is in principle more difficult because lithium reduction of the electrolyte usually yields an electronically conductive (and therefore not passivating) decomposition product. One solution to this problem may be to combine two electrolytes in a single cell such that the high-voltage electrolyte protects the low-voltage electrolyte from oxidation, and the low-voltage electrolyte protects the other from reduction. Due to the thickness of the electrolyte vs. a barrier coating, both materials needs to have high ionic conductivity. One such solution would be to use a combination of Li_3PS_4 against the anode and Li_2MgCl_4 against the cathode. The Li_2MgCl_4 protects the Li_3PS_4 from oxidation by the cathode, and Li_3PS_4 protects the Li_2MgCl_4 from reduction by the anode. The most basic requirement for compatibility of the two electrolytes is that their μ_{Li} stability ranges overlap so there is no driving force for Li transfer between them, but they should also be chosen such that they do not react in other ways, which can be verified using the methodology of equation 5.2.

While complete thermodynamic stability of the bulk electrolyte and cathode phases in contact with each other is ideal, this is difficult to achieve and our calculations show that this is likely not the case in a number of high performing systems. In batteries utilizing thiophosphate electrolytes our calculations show that the anode is likely to reduce the electrolyte, and in cells using a LiPON electrolyte we predict oxidation of nitrogen by the high cathode

voltage. In both of these cases, the decomposition products are electronically insulating and have significant lithium concentration, and so can support lithium ion conductivity. Optimization of the electrolyte/electrode combinations to produce similar passivating decomposition products may be a viable route towards creating high-performance systems and overcoming bulk chemical incompatibilities.

Our results suggest a few combinations of known cathode and electrolyte materials that may be combined to create high-performance batteries which have not been previously attempted. One such combination is that of Li_3PS_4 or the higher conductivity $Li_7P_3S_{11}$ glass-ceramic electrolyte combined with $LiVS_2$. This combination shows minimal decomposition energy according to figure 5-5. This cell is expected to have a higher voltage and slightly better stability than the similar $LiTiS_2$ cathode with Li_2S-P_2S_5 electrolyte of ref. 144, which is also predicted by our calculations to have good performance, and was able to cycle for over 50 cycles without a barrier coating. Another possible combination predicted by our calculations is a $LiBH_4$-$LiTiS_2$ cell. $LiBH_4$ is unstable against the high voltage of $LiCoO_2$ and a steadily increasing interfacial resistance is seen experimentally[138], but is predicted to be more stable against the lower voltage $LiTiS_2$.

5.4 Conclusions

In this chapter, we developed a computational method to screen cathode/electrolyte combinations for compatibility and interfacial stability in solid-state batteries. We find that the bulk material stability or passivation by ionically conductive products at the cathode μ_{Li} is essential for long-term device performance and that thermodynamic calculations allowing

mass transfer across the interface are also required to provide a more thorough analysis of the interfacial reaction and better predict experimental results. We use our methodology to screen a wide range of electrolyte/electrode combinations, finding good agreement with available experimental results and also suggesting numerous novel cells with improved stabilities compared to current state-of-the-art. The breadth of our calculated data also serves as a valuable reference for experimentalists wishing to construct cells with new combinations of battery materials.

5.5 Methods: Referencing DFT formation energies to experiment

For interface calculations, especially those that consider the Grand Potential (as these are open to a metal ion, and therefore are open to redox reactions), it is important that the relative energies of different elemental oxidation states be correctly determined, otherwise spurious reactions can be predicted. Various corrections schemes have been proposed in literature to more accurately capture charge transfer in DFT calculations[57]. Perhaps one of the more successful of these schemes is the GGA/GGA+U mixing scheme of Jain et al.[57], which simultaneously applies a U value[2] to the d-electrons of different transition metals to reproduce experimental formation energies of different oxidation states in oxide materials, while calibrating the oxygen reference energy to the formation energies of known binary compounds. For the calculation of properties such as battery voltages, this method works well. Similar schemes have also been fit to the sulfides [19]. These schemes, however, run into difficulties when attempting to calculate reactions including sulfates, because the

oxidation state, and therefore the types of DFT errors, differ from those made in the sulfide materials. As a result, using the GGA/GGA+U mixing scheme results in overstabilization of the sulfate materials by over 1 eV per sulfate polyanion. For Li_2SO_4, this error is 1.3 eV/f.u., for Na_2SO_4, 1.2 eV/atom. In principle, it is possible to extend this model further, and to apply corrections to different types of polyanion, i.e. a different correction to sulfate, sulfites, etc, but a significant downside to this approach is that it must be fit to every anion and polyanion individually.

For maximal generalizability, we instead use the observation that DFT calculated energy differences are typically very accurate when comparing energy differences between structures where the oxidation states of the species do not change. For any chemical system, to compute the formation energy, we compute a phase diagram using compositions that DFT predicts to be the ground state, and where an experimental formation energy is known. The experimental referencing scheme is equivalently formulated as a correction to the DFT computed energy. For every composition where the DFT and experimental energy is known, the difference between these two numbers is the correction to be applied to that composition. For intermediate compositions, the decomposition of a composition into the Gibbs triangle (using barycentric coordinates) is used to create a weighted average of corrections to apply to any given composition. The value of the 'correction' formulation is that it is easier to visualize the expected sources of DFT error. An example of calculating these corrections is shown in figure 5-6b.

To evaluate the efficacy of this corrections scheme, we cross validate the calculated formation energy on materials with a known formation energy with a leave-one-out CV on ternary compounds. The results of this cross-validation, for a dataset of 192 computed

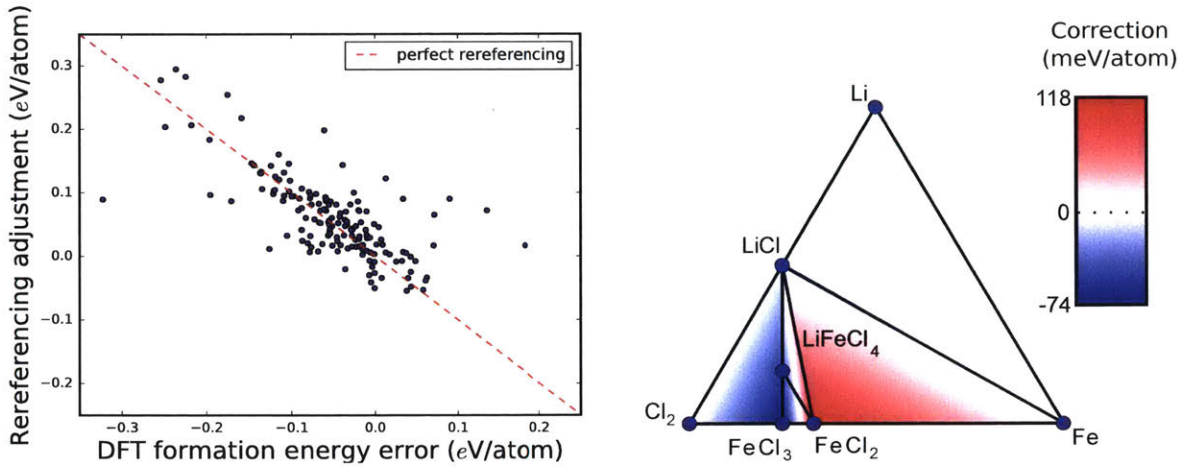

(a) (b)

Figure 5-6: **Referencing DFT data to experimental formation energies.** a) Leave-one-out error analysis of the formation energy referencing scheme using a dataset of ternary DFT computed structures. MAE error is reduced from 55 meV/atom to 20 meV/atom and RMSE error reduced from 89 meV/atom to 53 meV/atom. Points on the dotted line represent structures whose energies match experiment after the experimental referencing. The accuracy of points un the upper left and lower right quadrants are improved by the scheme b) Difference in energy as function of composition between typical DFT formation energy calculations and this reference scheme in the Li-Fe-Cl ternary phase diagrams. In this system, calculations are referenced to the $FeCl_3$ and $FeCl_2$ formation energies (in addition to the pure elements).

ternary structures, are shown in figure 5-6a. For most materials, the DFT formation energy error is reduced significantly, resulting in reduction of the mean absolute error (MAE) from 55 meV/atom to 20 meV per atom, and a reduction in root mean square (rms) error from 89 to 53 meV/atom.

Conclusions and Outlook

In this thesis, we have used a variety of first-principles calculation methodologies to investigate the transport and interfacial properties of solid electrolytes. We find that that the structure of the anion lattice is crucial to allow high conductivity, and that the chemistry of the conductor is the primary determinant of stability in contact with electrodes and cause of interfacial resistance in battery cells. Using thermodynamic stability calculations, we predicted the existence of two new high conductivity solid electrolyte materials, $Na_{10}SnP_2S_{12}$ and $Li_{1+2x}Zn_{1-x}PS_4$[122, 121].

The newly predicted sodium conductor $Na_{10}SnP_2S_{12}$ electrolyte has a DFT calculated conductivity of 0.94 mS cm^{-1} at room temperature, rivaling the best existing sulfide sodium-electrolytes, and the Si and Ge versions may surpass this conductivity. This is in good agreement with the subsequent experimental synthesis and characterization, which showed conductivity of 0.4 mS cm^{-1} at room temperature and activation energy of 0.35 eV. Through site-occupancy analysis of the AIMD simulations, we showed how the various metal substitutions in this framework can affect cation mobility by modulating the free energy landscape.

$Li_{1+2x}Zn_{1-x}PS_4$ ($0 \leq x < 0.5$) is predicted to have extremely high ionic conductivity, potentially 50 mS cm^{-1}, due to its highly mobile interstitial defects, and this maximum

conductivity is limited by the defect solubility. Because of the low electronegativity of Zn, LZPS is predicted to be more resistant to reduction than those in the LMPS system, which contain one of (Si, Ge, Sn). The thermodynamic stability calculations that predict the high interstitial defect solubility in LZPS illustrate the importance of phonon stabilization in ionic conductors. To enable calculation of configurational entropy in this system, we developed cluster expansion methodology to add electrostatic interactions, properly accounting for their non-convergent nature.

The importance of structural features governing diffusion, developed in chapter 3, places these new materials into a larger group of ionic conductors including $Li_{10}GeP_2S_{12}$ [65], $Li_7P_3S_{11}$[129], α-AgI, and lithium antiperovskites Li_3OCl, among others. Calculations of the migration barriers within a carefully controlled model system of ideal fcc, hcp, and bcc anion lattices (which can only exist in simulation) demonstrate that the bcc anion lattice leads to the highest ionic conductivity of these common frameworks. We used structural framework mapping algorithms to show that this sublattice is present in many of the highest conductivity materials.

To investigate the performance limitations of electrolytes in conjunction with electrode materials, we developed a thermodynamic method to compute interfacial reactivity. The method demonstrated thiophosphate materials are unstable in conjunction with most oxide cathodes and exposed to high driving forces to form more the more stable phosphate groups. This mixing methodology provided an explanation of why battery cells incorporating these electrolytes can only achieve high rates and cycle life when the cathodes are coated by a redox-inactive oxide material. Because the theoretical framework relies only on bulk energies, it is computationally efficient and can be transferred easily to new systems, even

when surfaces are complex. Understanding of the specifics of the decomposition mechanism is useful for limiting the scope of the search for new coating materials - the most promising chemistries are likely to be oxide, chloride, or fluoride materials because of their high voltage stability.

The results of this thesis are useful for strategies to further improve device performance. Our thermodynamic reactivity calculations show that bulk material stability or passivation by ionically conductive products at the cathode μ_{Li} is essential for long-term device performance. When a thiophosphate cathode is used in conjunction with an electronically insulating cathode coating, imperfections in coating coverage are not catastrophic. Though they are reactive, when thiophosphate materials come into contact with high-voltage oxide cathodes, they become ionic and electronic insulators – though they decompose, this reaction often passivates the interface. The fact that they are embedded in a solid matrix means that this passivated surface will likely remain at the interface, and will not consume cell components. This is in contrast to organic solvent electrolytes, many of whose reaction products with high voltage cathodes are soluble.

Lithium extraction and reactivity at the cathode are typically not seen in cyclic voltammetry measurements of electrolytes, as they do not measure the effect of the voltage on the ionic transport at the interface. CV curves however are useful in testing materials for this passivation property, which is especially critical at the interface between the cathode current collector and the electrolyte, since coating of the full cathode+current collector assemblage is impractical, especially in typical powder-based cells (thin-film cathodes may be the exception to this rule).

Solid electrolytes, even those without high voltage stability, have a promising future for

increasing accessible voltage range of lithium batteries. Though still short of the 10,000 cycles demonstrated for thin film LiPON batteries, improvements in cathode coatings have yielded thiophosphate-based high-power batteries showing 1,000 cycles with little capacity fade[71]. This experiment used a layered cobalt cathode, but our thermodynamic calculations do not immediately suggest any reasons why similar performance could not be obtained with a higher voltage cathode such as nickel-manganese oxide, provided that a cathode coating layer is used ($LiNbO_3$ and $LiTi_2(PO_4)_3$ are both calculated to be stable to around 4.5 V (figure 5-3), and Li_3PO_4 has been used as an electrolyte to 5 V[83]).

With high performance having been demonstrated for cathode materials and high-voltage intercalation anodes, the engineering of the integration of cells with higher capacity, lower voltage, anodes appears to be the next target for improvement. Coating of the anode is in principle more difficult because lithium reduction of the electrolyte usually yields an electronically conductive (and therefore not passivating) decomposition product. There are currently very few electrolytes stable against low-voltage anodes, principally because there exist very few elements that can resist reduction by lithium metal. An alternate solution to this problem may be to mix multiple electrolytes in a solid-state battery. In batteries employing lithium metal anodes, a thin layer of Li-stable electrolyte could be employed for the separator layer, with a higher conductivity electrolyte mixed with the cathode. This higher conductivity layer would not have to be stable against lithium metal, so wider variety of materials, including LZPS and materials in the LGPS family, could conceivably be used. Using mixed conductors in the cathode layer seems attractive as it could increase cathode loading, but unfortunately will be problematic if they do not show high voltage stability (this rules out sulfide mixed conductors), since they cannot passivate the lithium extraction

from the electrolyte.

None of the highest conductivity solid electrolytes are thermodynamically stable at 0 K, and many are not the thermodynamic ground state even at room temperature. All of the LGPS-type materials, their sodium analogs, the high conductivity phases of LZPS, $Li_7P_3S_{11}$, lithium garnets, the high conductivity phases of Li_3PS_4 and Na_3PS_4 are stabilized at higher temperature, and more recent results on the lithium antiperovskites[84] suggest that their performance may stem from hydrogen or other defects, which entropically stabilize the high conductivity cubic phase. Computational prediction of new materials therefore relies heavily on the accuracy of finite-temperature thermodynamic calculations, with contributions coming from both phonons and configurational entropy. The computational prediction of new completely new (rather than a compositional modification of a known materials) stable phase relies on both the high accuracy of the DFT functional, as well as in the calculation of the finite temperature effects. Comprehensive finite temperature calculations in the Li-P-S system, which is important as it is one of the few that is stable (albeit through passivation) against Li-metal, are especially difficult because there are a number of liquid phases that begin to compete at typical processing temperatures.

Another computational challenge is the modeling of dendrite formation. Some models suggest that physical properties of the solid electrolyte can suppress dendrite formation[97], but the presence of grain boundaries and pores in the electrolyte can lead to cracking of the electrolyte at rates above 1 mA cm^{-2}, though at rates below 0.01 mA cm^{-2} homogenous deposition without cracking was observed[101]. To put these currents into perspective, a typical 0.5 mm thick oxide cathode requires approximately 20 mA cm^{-2} to achieve a 1 C rate. Additionally, this interface is complicated by the reaction of lithium with the electrolyte to

form a thin interfacial region with different mechanical and electronic and ionic conduction characteristics. For example, the formation of Li_3P at the interface could lead to higher ionic conductivity[102], and is also accompanied by a volume expansion that can affect both the mechanical suppression of dendrite formation and crack formation. The effects of these processes on the dendrite formation are currently not well understood, and could benefit from further modeling efforts to suggest strategies for device improvement.

Bibliography

[1] J. Allen, J. Wolfenstine, E. Rangasamy, and J. Sakamoto. Effect of substitution (Ta, Al, Ga) on the conductivity of $Li_7La_3Zr_2O_{12}$. *J. Power Sources*, 206:315–319, 2012.

[2] V. I. Anisimov, J. Zaanen, and O. K. Andersen. Band theory and Mott insulators: Hubbard U instead of Stoner I. *Phys. Rev. B*, 44(3):943–954, 1991.

[3] L. Anthony, L. J. Nagel, J. K. Okamoto, and B. Fultz. Magnitude and Origin of the Difference in Vibrational Entropy between Ordered and Disordered Fe3Al. *Phys. Rev. Lett.*, 73(22):3034–3037, 1994.

[4] H. Aono. Ionic Conductivity of Solid Electrolytes Based on Lithium Titanium Phosphate. *J. Electrochem. Soc.*, 137(4):1023–1027, 1990.

[5] P. Arora, R. E. White, and M. Doyle. Capacity Fade Mechanisms and Side Reactions in Lithium-Ion Batteries. *J. Electrochem. Soc.*, 145(10):3647–3667, 1998.

[6] D. Aurbach, B. D. McCloskey, L. F. Nazar, and P. G. Bruce. Advances in understanding mechanisms underpinning lithium-air batteries. *Nat. Energy*, 1(9):16128, 2016.

[7] P. G. Balakrishnan, R. Ramesh, and T. Prem Kumar. Safety mechanisms in lithium-ion batteries. *J. Power Sources*, 155(2):401–414, 2006.

[8] J. B. Bates, N. J. Dudney, B. Neudecker, A. Ueda, and C. D. Evans. Thin-film lithium and lithium-ion batteries. *Solid State Ionics*, 135(1-4):33–45, 2000.

[9] A. Belsky, M. Hellenbrandt, V. L. Karen, and P. Luksch. New developments in the Inorganic Crystal Structure Database (ICSD): accessibility in support of materials research and design. *Acta Crystallogr. Sect. B Struct. Sci.*, 58(3):364–369, 2002.

[10] P. E. Blöchl. Projector augmented-wave method. *Phys. Rev. B*, 50(24):17953–17979, 1994.

[11] J. Briant and G. Farrington. Ionic Conductivity in Lithium and Lithium Sodium Beta Alumina. *J. Electrochem. Soc.*, 128(9):1830–1834, 1981.

[12] P. Bron, S. Johansson, K. Zick, J. Schmedt auf der Günne, S. Dehnen, and B. Roling. $Li_{10}SnP_2S_{12}$: an affordable lithium superionic conductor. *J. Am. Chem. Soc.*, 135(42):15694–15697, 2013.

[13] P. G. Bruce and A. R. West. The A-C Conductivity of Polycrystalline LISICON, $Li_{2+x}Zn_{1-x}GeO_4$, and a Model for Intergranular Constriction Resistances. *J. Electrochem. Soc.*, 130(3):662–669, 1983.

[14] P. G. Bruce, S. A. Freunberger, L. J. Hardwick, and J.-M. Tarascon. Li-O_2 and Li-S batteries with high energy storage. *Nat. Mater.*, 11(02):172–172, 2011.

[15] H. Burzlaff and Y. Malinovsky. A Procedure for the Clasification of Non-Organic Crystal Structures. I. Theoretical Background. *Acta Crystallogr. Sect. A Found. Crystallogr.*, 53(2):217–224, 1997.

[16] E. Candes and M. Wakin. An Introduction To Compressive Sampling. *IEEE Signal Process. Mag.*, 25(2):21–30, 2008.

[17] K. Capelle. A bird's-eye view of density-functional theory. *arXiv:cond-mat/0211443*, page 69, 2002.

[18] G. Ceder, P. D. Tepesch, A. F. Kohan, and A. Van der Ven. A model to Predict Ionic Disorder and Phase Diagrams: Application to CaO-MgO, Gd_2O_3-ZrO_2, and to Sodium β''-alumina. *J. Electroceramics*, 1(1):15–26, 1997.

[19] I.-H. Chu, H. Nguyen, S. Hy, Y.-C. Lin, Z. Wang, Z. Xu, Z. Deng, Y. S. Meng, and S. P. Ong. Insights into the Performance Limits of the $Li_7P_3S_{11}$ Superionic Conductor: A Combined First-Principles and Experimental Study. *ACS Appl. Mater. Interfaces*, 8(12):7843–7853, 2016.

[20] C. Cros, L. Hanebali, L. Latie, G. Villeneuve, and W. Gang. Structure, ionic motion and conductivity in some solid-solutions of the LiCl-MCl_2 systems (M=Mg,V,Mn). *Solid State Ionics*, 9-10:139–147, 1983.

[21] H.-j. Deiseroth, S.-t. Kong, H. Eckert, J. Vannahme, C. Reiner, T. Zaiß, and M. Schlosser. Li_6PS_5X : A Class of Crystalline Li-Rich Solids With an Unusually High Li^+ Mobility. *Angew. Chem. Int. Ed. Engl.*, 47:755–758, 2008.

[22] S. L. Dudarev, S. Y. Savrasov, C. J. Humphreys, and A. P. Sutton. Electron-energy-loss spectra and the structural stability of nickel oxide: An LSDA+U study. *Phys. Rev. B*, 57(3):1505–1509, 1998.

[23] N. J. Dudney. Nanocrystalline $Li_xMn_{2-y}O_4$ Cathodes for Solid-State Thin-Film Rechargeable Lithium Batteries. *J. Electrochem. Soc.*, 146(7):2455–2464, 1999.

[24] B. L. Ellis and L. F. Nazar. Sodium and sodium-ion energy storage batteries. *Curr. Opin. Solid State Mater. Sci.*, 16(4):168–177, 2012.

[25] A. Emly, E. Kioupakis, and A. Van der Ven. Phase Stability and Transport Mechanisms in Antiperovskite Li_3OCl and Li_3OBr Superionic Conductors. *Chem. Mater.*, 25:4663–4670, 2013.

[26] M. Ernzerhof and G. E. Scuseria. Perspective on "Inhomogeneous electron gas". *Theor. Chem. Accounts Theory, Comput. Model. (Theoretica Chim. Acta)*, 103(3-4):259–262, 2000.

[27] P. P. Ewald. Die Berechnung optischer und elektrostatischer Gitterpotentiale. *Ann. Phys.*, 369(3):253–287, 1921.

[28] J. W. Fergus. Ion transport in sodium ion conducting solid electrolytes. *Solid State Ionics*, 227:102–112, 2012.

[29] A. M. Ferrenberg and R. H. Swendsen. New Monte Carlo technique for studying phase transitions. *Phys. Rev. Lett.*, 61(23):2635–2638, 1988.

[30] D. D. Fontaine. Cluster Approach to Order-Disorder Transformations in Alloys. In *Solid State Phys. - Adv. Res. Appl.*, volume 47, pages 33–176. Academic Press, Inc., 1994.

[31] S. Gallagher. Boeing's Dreamliner batteries 'inherently unsafe' - and yours may be too. *Ars Tech.*, 2013.

[32] P. Geerlings, F. De Proft, and W. Langenaeker. Conceptual density functional theory. *Chem. Rev.*, 103(5):1793–873, 2003.

[33] D. C. Ginnings and T. E. Phipps. Temperature-Conductance Curves of Solid Salts. III. Halides of Lithium. *J. Am. Chem. Soc.*, 52(4):1340–1345, 1930.

[34] N. A. Godshall, I. D. Raistrick, and R. A. Huggins. Relationships among Electrochemical, Thermodynamic, and Oxygen Potential Quantities in Lithium-Transition Metal-Oxygen Molten Salt Cells. *J. Electrochem. Soc.*, 131(3):543, 1984.

[35] T. Goldstein and S. Osher. The Split Bregman Method for L1-Regularized Problems. *SIAM J. Imaging Sci.*, 2(2):323–343, 2009.

[36] J. B. Goodenough and K.-s. Park. The Li-Ion Rechargeable Battery: A Perspective. *J. Am.*

Chem. Soc., 135:1167–1176, 2013.

[37] I. Gyuk, M. Johnson, J. Vetrano, K. Lynn, W. Parks, R. Handa, L. D. Kannberg, S. Hearne, K. Waldrip, R. Braccio, and US DOE. Grid Energy Storage. 2013.

[38] F. Han, T. Gao, Y. Zhu, K. J. Gaskell, and C. Wang. A Battery Made from a Single Material. *Adv. Mater.*, 27(23):3473–3483, 2015.

[39] W. K. Hastings. Monte Carlo sampling methods using Markov chains and their applications. *Biometrika*, 57(1):97–109, 1970.

[40] G. Hautier, C. Fischer, V. Ehrlacher, A. Jain, and G. Ceder. Data mined ionic substitutions for the discovery of new compounds. *Inorg. Chem.*, 50(2):656–663, 2011.

[41] G. Hautier, C. C. Fischer, A. Jain, T. Mueller, and G. Ceder. Finding Nature's Missing Ternary Oxide Compounds Using Machine Learning and Density Functional Theory. *Chem. Mater.*, 22(12):3762–3767, 2010.

[42] G. Hautier, S. P. Ong, A. Jain, C. J. Moore, and G. Ceder. Accuracy of density functional theory in predicting formation energies of ternary oxides from binary oxides and its implication on phase stability. *Phys. Rev. B*, 85(15):155208, 2012.

[43] A. Hayashi, K. Noi, A. Sakuda, and M. Tatsumisago. Superionic glass-ceramic electrolytes for room-temperature rechargeable sodium batteries. *Nat. Commun.*, 3:856, 2012.

[44] A. Hayashi, K. Noi, N. Tanibata, M. Nagao, and M. Tatsumisago. High sodium ion conductivity of glass-ceramic electrolytes with cubic Na_3PS_4. *J. Power Sources*, 258:420–423, 2014.

[45] E. Helfand. Transport Coefficients from Dissipation in a Canonical Ensemble. *Phys. Rev.*, 119(1):1–9, 1960.

[46] G. Henkelman, B. P. Uberuaga, and H. Jónsson. A climbing image nudged elastic band method for finding saddle points and minimum energy paths. *J. Chem. Phys.*, 113(22):9901, 2000.

[47] P. Hohenberg and W. Kohn. Inhomogeneous Electron Gas. *Phys. Rev.*, 136(3):B864–871, 1964.

[48] K. Homma, M. Yonemura, T. Kobayashi, M. Nagao, M. Hirayama, and R. Kanno. Crystal structure and phase transitions of the lithium ionic conductor Li_3PS_4. *Solid State Ionics*, 182(1):53–58, 2011.

[49] S. Hori, K. Suzuki, M. Hirayama, Y. Kato, T. Saito, M. Yonemura, and R. Kanno. Synthesis, structure, and ionic conductivity of solid solution, $Li_{10+\delta}M_{1+\delta}P_{2-\delta}S_{12}$(M = Si, Sn). *Faraday Discuss.*, 176:83–94, 2014.

[50] K. Hoshina, K. Dokko, and K. Kanamura. Investigation on Electrochemical Interface between $Li_4Ti_5O_{12}$ and $Li_{1+x}Al_xTi_{2-x}(PO_4)_3$ NASICON-Type Solid Electrolyte. *J. Electrochem. Soc.*, 152(11):A2138–A2142, 2005.

[51] K. B. Hueso, M. Armand, and T. Rojo. High temperature sodium batteries: status, challenges and future trends. *Energy Environ. Sci.*, 6(3):734–749, 2013.

[52] R. A. Huggins. Lithium alloy negative electrodes. *J. Power Sources*, 81-82:13–19, 1999.

[53] S. Hull. Superionics: crystal structures and conduction processes. *Rep. Prog. Phys.*, 67:1233–1314, 2004.

[54] R. Hundt, J. C. Schon, and M. Jansen. CMPZ - An algorithm for the efficient comparison of periodic structures. *J. Appl. Crystallogr.*, 39(1):6–16, 2006.

[55] Y. Inaguma, L. Chen, M. Itoh, and T. Nakamura. High Ionic Conductivity in Lithium Lanthanum Titanate. *Solid State Commun.*, 86(10):689–693, 1993.

[56] A. Jain, G. Hautier, C. J. Moore, S. P. Ong, C. C. Fischer, T. Mueller, K. A. Persson, and G. Ceder. A high-throughput infrastructure for density functional theory calculations. *Comput.*

Mater. Sci., 50(8):2295–2310, 2011.

[57] A. Jain, G. Hautier, S. P. Ong, C. J. Moore, C. C. Fischer, K. A. Persson, and G. Ceder. Formation enthalpies by mixing GGA and GGA + U calculations. *Phys. Rev. B*, 84(4):1–10, 2011.

[58] A. Jain, S. P. Ong, G. Hautier, W. Chen, W. D. Richards, S. Dacek, S. Cholia, D. Gunter, D. Skinner, G. Ceder, and K. A. Persson. Commentary: The Materials Project: A materials genome approach to accelerating materials innovation. *APL Mater.*, 1(1):011002, 2013.

[59] A. N. Jansen, A. J. Kahaian, K. D. Kepler, P. A. Nelson, K. Amine, D. W. Dees, D. R. Vissers, and M. M. Thackeray. Development of a high-power lithium-ion battery. *J. Power Sources*, 81-82:902–905, 1999.

[60] M. Jansen and U. Henseler. Synthesis, structure determination, and ionic conductivity of sodium tetrathiophosphate. *J. Solid State Chem.*, 99:110–119, 1992.

[61] R. Jonker and A. Volgenant. A shortest augmenting path algorithm for dense and sparse linear assignment problems. *Computing*, 340:325–340, 1987.

[62] H. Jonsson, G. Mills, and K. Jacobsen. Nudged elastic band method for finding minimum energy paths of transitions. In *Class. quantum Dyn. Condens. phase simulations*, pages 385–404. World Scientific, 1998.

[63] S. Jörgens, D. Johrendt, and A. Mewis. Motive dichtester Kugelpackungen: Die Verbindungen $Zn_3(PS_4)_2$ und $LiZnPS_4$. *Zeitschrift für Anorg. und Allg. Chemie*, 628(8):1765, 2002.

[64] H.-G. Jung, J. Hassoun, J.-B. Park, Y.-K. Sun, and B. Scrosati. An improved high-performance lithium-air battery. *Nat. Chem.*, 4(7):579–585, 2012.

[65] N. Kamaya, K. Homma, Y. Yamakawa, M. Hirayama, R. Kanno, M. Yonemura, T. Kamiyama, Y. Kato, S. Hama, K. Kawamoto, and A. Mitsui. A lithium superionic conductor. *Nat. Mater.*, 10(9):682–686, 2011.

[66] V. S. Kandagal, M. D. Bharadwaj, and U. V. Waghmare. Theoretical prediction of a highly conducting solid electrolyte for sodium batteries: $Na_{10}GeP_2S_{12}$. *J. Mater. Chem. A*, 3(24):12992–12999, 2015.

[67] K. Kang and G. Ceder. Factors that affect Li mobility in layered lithium transition metal oxides. *Phys. Rev. B*, 74:094105, 2006.

[68] R. Kanno, Y. Takeda, and O. Yamamoto. Ionic conductivity of solid lithium ion conductors with the spinel structure: Li_2MCl_4 (M=Mg, Mn, Fe, Cd). *Mater. Res. Bull.*, 16:999–1005, 1981.

[69] R. Kanno, Y. Takeda, and O. Yamamoto. Ionic Conductivity and Phase Transition of the Bromide Spinels, $Li_{2-2x}M_{1+x}Br_4$ (M=Mg, Mn). *J. Electrochem. Soc.*, 4:1052–1056, 1986.

[70] R. Kanno and M. Murayama. Lithium Ionic Conductor Thio-LISICON: The Li_2S-GeS_2-P_2S_5 System. *J. Electrochem. Soc.*, 148(7):A742, 2001.

[71] Y. Kato, S. Hori, T. Saito, K. Suzuki, M. Hirayama, A. Mitsui, M. Yonemura, H. Iba, and R. Kanno. High-power all-solid-state batteries using sulfide superionic conductors. *Nat. Energy*, 1(4):16030, 2016.

[72] H. Khireddine, P. Fabry, A. Caneiro, and B. Bochu. Optimization of NASICON composition for Na^+ recognition. *Sensors Actuators B Chem.*, 40:223–230, 1997.

[73] S.-W. Kim, D.-H. Seo, X. Ma, G. Ceder, and K. Kang. Electrode Materials for Rechargeable Sodium-Ion Batteries: Potential Alternatives to Current Lithium-Ion Batteries. *Adv. Energy Mater.*, 2(7):710–721, 2012.

[74] P. Knauth. Inorganic solid Li ion conductors: An overview. *Solid State Ionics*, 180(14-16):911–916, 2009.

[75] S. Komaba, W. Murata, T. Ishikawa, N. Yabuuchi, T. Ozeki, T. Nakayama, A. Ogata, K. Gotoh, and K. Fujiwara. Electrochemical Na Insertion and Solid Electrolyte Interphase for Hard-Carbon Electrodes and Application to Na-Ion Batteries. *Adv. Funct. Mater.*, 21(20):3859–3867, 2011.

[76] G. Kresse and J. Furthmüller. Efficient iterative schemes for ab initio total-energy calculations using a plane-wave basis set. *Phys. Rev. B*, 54(16):11169–11186, 1996.

[77] O. Kubaschewski, C. B. Alcock, and P. J. Spencer. *Materials Thermochemistry.* Pergamon Press, Oxford, 6th edition, 1993.

[78] A. Kuhn, V. Duppel, and B. V. Lotsch. Tetragonal $Li_{10}GeP_2S_{12}$ and Li_7GePS_8 - exploring the Li ion dynamics in LGPS Li electrolytes. *Energy Environ. Sci.*, 6(12):3548–3552, 2013.

[79] A. Kuhn, O. Gerbig, C. Zhu, F. Falkenberg, J. Maier, and B. V. Lotsch. A new ultrafast superionic Li-conductor: ion dynamics in $Li_{11}Si_2PS_{12}$ and comparison with other tetragonal LGPS-type electrolytes. *Phys. Chem. Chem. Phys.*, 16(28):14669–14674, 2014.

[80] A. Kuhn, J. Koehler, and B. V. Lotsch. Single-Crystal X-ray Structure Analysis of the Superionic Conductor $Li_{10}GeP_2S_{12}$. *Phys. Chem. Chem. Phys.*, 15(28):11620–11622, 2013.

[81] C. Lee, W. Yang, and R. G. Parr. Development of the Colle-Salvetti correlation-energy formula into a functional of the electron density. *Phys. Rev. B*, 37(2):785–789, 1988.

[82] N. Lepley and N. Holzwarth. Computer Modeling of Crystalline Electrolytes - Lithium Thiophosphates and Phosphates. *ECS Trans.*, 35(14):39–51, 2011.

[83] J. Li, C. Ma, M. Chi, C. Liang, and N. J. Dudney. Solid Electrolyte: the Key for High-Voltage Lithium Batteries. *Adv. Energy Mater.*, 5(4):1401408, 2015.

[84] Y. Li, W. Zhou, S. Xin, S. Li, J. Zhu, L. Xujie, Z. Cui, Q. Jia, J. Zhou, Y. Zhao, and J. B. Goodenough. Fluorine-Doped Antiperovskite Electrolyte for All-Solid-State Lithium-Ion Batteries. *Angew. Chemie - Int. Ed.*, 55(34):9965–9968, 2016.

[85] Z. Lin, Z. Liu, N. J. Dudney, and C. Liang. Lithium Superionic Sulfide Cathode for All-Solid Lithium-Sulfur Batteries. *ACS Nano*, 7(3):2829–2833, 2013.

[86] Z. Liu, W. Fu, E. A. Payzant, X. Yu, Z. Wu, N. J. Dudney, J. Kiggans, K. Hong, A. J. Rondinone, and C. Liang. Anomalous high ionic conductivity of nanoporous β-Li_3PS_4. *J. Am. Chem. Soc.*, 135(3):975–978, 2013.

[87] S. Lloyd. Least squares quantization in PCM. *Inf. Theory, IEEE Trans.*, 28(2):129–137, 1982.

[88] C. J. J. V. Loon and J. de Jong. Some chlorides with the inverse spinel structure. *Acta Crystallogr. Sect. B Struct. Crystallogr. Cryst. Chem.*, 2549(1966):2549–2550, 1975.

[89] E. Madelung. Das elektrische feld in systemen von regelmäßig angeordneten punktladungen. *Phys Z.*, XIX:524–533, 1918.

[90] J. Malcolm W. Chase. NIST-JANAF Thermochemical Tables. *J. Phys. Chem. Ref. Data*, Monogram 9, 1998.

[91] R. Marom, S. F. Amalraj, N. Leifer, D. Jacob, and D. Aurbach. A review of advanced and practical lithium battery materials. *J. Mater. Chem.*, 21(27):9938, 2011.

[92] D. A. McQuarrie. *Statistical Mechanics.* University Science Books, Sausalito, California, 2000.

[93] F. Meier and C. Woodyard. Feds review third Tesla fire as shares fall again, 2013.

[94] N. Metropolis, A. W. Rosenbluth, M. N. Rosenbluth, A. H. Teller, and E. Teller. Equation of State Calculations by Fast Computing Machines. *J. Chem. Phys.*, 21(6):1087, 1953.

[95] Y. Mo, S. P. Ong, and G. Ceder. First principles study of the $Li_{10}GeP_2S_{12}$ lithium super ionic conductor material. *Chem. Mater.*, 24(1):15–17, 2012.

[96] K. Momma and F. Izumi. VESTA: A three-dimensional visualization system for electronic and structural analysis. *J. Appl. Crystallogr.*, 41(3):653–658, 2008.

[97] C. Monroe and J. Newman. The Impact of Elastic Deformation on Deposition Kinetics at Lithium/Polymer Interfaces. *J. Electrochem. Soc.*, 152:A396, 2005.

[98] M. Murayama, N. Sonoyama, A. Yamada, and R. Kanno. Material design of new lithium ionic conductor, thio-LISICON , in the Li_2S - P_2S_5 system. *Solid State Ionics*, 170:173–180, 2004.

[99] G. Murch. The haven ratio in fast ionic conductors. *Solid State Ionics*, 7(3):177–198, 1982.

[100] R. Murugan, V. Thangadurai, and W. Weppner. Fast lithium ion conduction in garnet-type $Li_7La_3Zr_2O_{12}$. *Angew. Chem. Int. Ed. Engl.*, 46(41):7778–7781, 2007.

[101] M. Nagao, A. Hayashi, M. Tatsumisago, T. Kanetsuku, T. Tsuda, and S. Kuwabata. In situ SEM study of a lithium deposition and dissolution mechanism in a bulk-type solid-state cell with a Li_2S-P_2S_5 solid electrolyte. *Phys. Chem. Chem. Phys.*, 15(42):18600–6, 2013.

[102] G. Nazri. Preparation, structure and ionic conductivity of lithium phosphide. *Solid State Ionics*, 34(1-2):97–102, 1989.

[103] L. J. Nelson, G. L. W. Hart, F. Zhou, and V. Ozolins. Compressive sensing as a paradigm for building physics models. *Phys. Rev. B*, 87(3):035125, 2013.

[104] N. Nitta, F. Wu, J. T. Lee, and G. Yushin. Li-ion battery materials: Present and future. *Mater. Today*, 18(5):252–264, 2015.

[105] S. Nosé. A unified formulation of the constant temperature molecular dynamics methods. *J. Chem. Phys.*, 81(1):511–519, 1984.

[106] N. Ohta, K. Takada, L. Zhang, R. Ma, M. Osada, and T. Sasaki. Enhancement of the High-Rate Capability of Solid-State Lithium Batteries by Nanoscale Interfacial Modification. *Adv. Mater.*, 18(17):2226–2229, 2006.

[107] S. Ohta, T. Kobayashi, and T. Asaoka. High lithium ionic conductivity in the garnet-type oxide $Li_{7-X}La_3(Zr_{2-X}, Nb_X)O_{12}$ (X=0-2). *J. Power Sources*, 196(6):3342–3345, 2011.

[108] S. Ohta, J. Seki, Y. Yagi, Y. Kihira, T. Tani, and T. Asaoka. Co-sinterable lithium garnet-type oxide electrolyte with cathode for all-solid-state lithium ion battery. *J. Power Sources*, 265:40–44, 2014.

[109] S. P. Ong, Y. Mo, W. D. Richards, L. Miara, H. S. Lee, and G. Ceder. Phase stability, electrochemical stability and ionic conductivity of the $Li_{10\pm1}MP_2X_{12}$ (M = Ge, Si, Sn, Al or P, and X = O, S or Se) family of superionic conductors. *Energy Environ. Sci.*, 6(1):148–156, 2013.

[110] S. P. Ong, W. D. Richards, A. Jain, G. Hautier, M. Kocher, S. Cholia, D. Gunter, V. L. Chevrier, K. A. Persson, and G. Ceder. Python Materials Genomics (pymatgen): A robust, open-source python library for materials analysis. *Comput. Mater. Sci.*, 68:314–319, 2013.

[111] S. P. Ong, L. Wang, B. Kang, and G. Ceder. Li-Fe-P-O_2 Phase Diagram from First Principles Calculations. *Chem. Mater.*, 20(5):1798–1807, 2008.

[112] V. Ozolins, C. Wolverton, and A. Zunger. Cu-Au, Ag-Au, Cu-Ag, and Ni-Au intermetallics: First-principles study of temperature-composition phase diagrams and structures. *Phys. Rev. B*, 57(11):6427–6443, 1998.

[113] V. Palomares, M. Casas-Cabanas, E. Castillo-Martínez, M. H. Han, and T. Rojo. Update on Na-based battery materials. A growing research path. *Energy Environ. Sci.*, 6(8):2312–2337, 2013.

[114] H. Pan, Y.-S. Hu, and L. Chen. Room-temperature stationary sodium-ion batteries for large-scale electric energy storage. *Energy Environ. Sci.*, 6(8):2338, 2013.

[115] J. P. Perdew, K. Burke, and M. Ernzerhof. Generalized Gradient Approximation Made Simple. *Phys. Rev. Lett.*, 77(18):3865–3868, 1996.

[116] J. P. Perdew and A. Zunger. Self-interaction correction to density-functional approximations

for many-electron systems. *Phys. Rev. B*, 23(10):5048–5079, 1981.

[117] A. Ponrouch, E. Marchante, M. Courty, J.-M. Tarascon, and M. R. Palacín. In search of an optimized electrolyte for Na-ion batteries. *Energy Environ. Sci.*, 5(9):8572, 2012.

[118] D. A. Porter and K. E. Easterling. *Phase Transformations in Metals and Alloys.* Nelson Thornes Ltd, Cheltenham, United Kingdom, 2nd edition, 1981.

[119] E. Rangasamy, Z. Liu, M. Gobet, K. Pilar, G. Sahu, W. Zhou, H. Wu, S. Greenbaum, and C. Liang. An Iodide-Based $Li_7P_2S_8I$ Superionic Conductor. *J. Am. Chem. Soc.*, 137(4):1384–1387, 2015.

[120] Y. Ren, Y. Shen, Y. Lin, and C. W. Nan. Direct observation of lithium dendrites inside garnet-type lithium-ion solid electrolyte. *Electrochem. commun.*, 57:27–30, 2015.

[121] W. D. Richards, L. J. Miara, Y. Wang, J. C. Kim, and G. Ceder. Interface Stability in Solid-State Batteries. *Chem. Mater.*, 28(1):266–273, 2016.

[122] W. D. Richards, T. Tsujimura, L. J. Miara, Y. Wang, J. C. Kim, S. P. Ong, I. Uechi, N. Suzuki, and G. Ceder. Design and synthesis of the superionic conductor $Na_{10}SnP_2S_{12}$. *Nat. Commun.*, 7:11009, 2016.

[123] G. Sahu, Z. Lin, J. Li, Z. Liu, N. Dudney, and C. Liang. Air-stable, high-conduction solid electrolytes of arsenic-substituted Li_4SnS_4. *Energy Environ. Sci.*, 7(3):1053–1058, 2014.

[124] A. Sakuda, A. Hayashi, and M. Tatsumisago. Interfacial Observation between $LiCoO_2$ Electrode and Li_2S-P_2S_5 Solid Electrolytes of All-Solid-State Lithium Secondary Batteries Using Transmission Electron Microscopy. *Chem. Mater.*, 22(3):949–956, 2010.

[125] J. M. Sanchez, J. P. Stark, and V. L. Moruzzi. First-principles calculation of the Ag-Cu phase diagram. *Phys. Rev. B*, 44(11):5411–5418, 1991.

[126] J. Sanchez. Cluster expansions and the configurational energy of alloys. *Phys. Rev. B*, 48(18):13–15, 1993.

[127] J. Sanchez, F. Ducastelle, and D. Gratias. Generalized cluster description of multicomponent systems. *Phys. A Stat. Mech. its Appl.*, 128(1-2):334–350, 1984.

[128] A. Schwöbel, R. Hausbrand, and W. Jaegermann. Interface reactions between LiPON and lithium studied by in-situ X-ray photoemission. *Solid State Ionics*, 273:51–54, 2015.

[129] Y. Seino, T. Ota, K. Takada, A. Hayashi, and M. Tatsumisago. A sulphide lithium super ion conductor is superior to liquid ion conductors for use in rechargeable batteries. *Energy Environ. Sci.*, 7(2):627–631, 2014.

[130] K. Senevirathne, C. S. Day, M. D. Gross, A. Lachgar, and N. Holzwarth. A new crystalline LiPON electrolyte: Synthesis, properties, and electronic structure. *Solid State Ionics*, 233:95–101, 2013.

[131] D. Sheppard, R. Terrell, and G. Henkelman. Optimization methods for finding minimum energy paths. *J. Chem. Phys.*, 128(13):134106, 2008.

[132] T. G. Stoebe and R. A. Huggins. Measurement of ionic diffusion in lithium fluoride by nuclear magnetic resonance techniques. *J. Mater. Sci.*, 1(2):117–126, 1966.

[133] J. Sun, A. Ruzsinszky, and J. P. Perdew. Strongly Constrained and Appropriately Normed Semilocal Density Functional. *Phys. Rev. Lett.*, 036402(July):1–6, 2015.

[134] M. Tachez, J. Malugani, R. Mercier, and G. Robert. Ionic conductivity of and phase transition in lithium thiophosphate Li_3PS_4. *Solid State Ionics*, 14:181–185, 1984.

[135] K. Takada. Progress and prospective of solid-state lithium batteries. *Acta Mater.*, 61(3):759–770, 2013.

[136] K. Takada, N. Ohta, L. Zhang, K. Fukuda, I. Sakaguchi, R. Ma, M. Osada, and T. Sasaki. Interfacial modification for high-power solid-state lithium batteries. *Solid State Ionics*, 179(27-

32):1333–1337, 2008.

[137] K. Takada, N. Ohta, L. Zhang, X. Xu, B. T. Hang, T. Ohnishi, M. Osada, and T. Sasaki. Interfacial phenomena in solid-state lithium battery with sulfide solid electrolyte. *Solid State Ionics*, 225:594–597, 2012.

[138] K. Takahashi, K. Hattori, T. Yamazaki, K. Takada, M. Matsuo, S. Orimo, H. Maekawa, and H. Takamura. All-solid-state lithium battery with $LiBH_4$ solid electrolyte. *J. Power Sources*, 226:61–64, 2013.

[139] N. Tanibata, K. Noi, A. Hayashi, N. Kitamura, Y. Idemoto, and M. Tatsumisago. X-ray Crystal Structure Analysis of Sodium-Ion Conductivity in 94 Na_3PS_4 - 6 Na_4SiS_4 Glass-Ceramic Electrolytes. *ChemElectroChem*, 1(7):1130–1132, 2014.

[140] M. Tatsumisago, M. Nagao, and A. Hayashi. Recent development of sulfide solid electrolytes and interfacial modification for all-solid-state rechargeable lithium batteries. *J. Asian Ceram. Soc.*, 1(1):17–25, 2013.

[141] P. D. Tepesch, G. D. Garbulsky, and G. Ceder. Model for Configurational Thermodynamics in Ionic Systems. *Phys. Rev. Lett.*, 74(12):2272–2275, 1995.

[142] V. Thangadurai, S. Narayanan, and D. Pinzaru. Garnet-type solid-state fast Li ion conductors for Li batteries: critical review. *Chem. Soc. Rev.*, 43(13):4714–4727, 2014.

[143] A. Togo and I. Tanaka. First principles phonon calculations in materials science. *Scr. Mater.*, 108:1–5, 2015.

[144] J. E. Trevey, C. R. Stoldt, and S.-H. Lee. High Power Nanocomposite TiS_2 Cathodes for All-Solid-State Lithium Batteries. *J. Electrochem. Soc.*, 158(12):A1282–A1289, 2011.

[145] C. L. Tsai, V. Roddatis, C. V. Chandran, Q. Ma, S. Uhlenbruck, M. Bram, P. Heitjans, and O. Guillon. $Li_7La_3Zr_2O_{12}$ Interface Modification for Li Dendrite Prevention. *ACS Appl. Mater. Interfaces*, 8(16):10617–10626, 2016.

[146] C. Uebing and R. Gomer. Determination of Surface-Diffusion Coefficients by Monte-Carlo Methods - Comparison of Fluctuation and Kubo-Green Methods. *J. Chem. Phys.*, 100(10):7759–7766, 1994.

[147] A. Urban, J. Lee, and G. Ceder. The Configurational Space of Rocksalt-Type Oxides for High-Capacity Lithium Battery Electrodes. *Adv. Energy Mater.*, 4:1400478, 2014.

[148] L. O. Valøen and J. N. Reimers. Transport Properties of $LiPF_6$-Based Li-Ion Battery Electrolytes. *J. Electrochem. Soc.*, 152(5):A882, 2005.

[149] A. van de Walle and G. Ceder. Automating first-principles phase diagram calculations. *J. Phase Equilibria*, 23(4):348–359, 2002.

[150] A. van de Walle, G. Ceder, and U. V. Waghmare. First-principles computation of the vibrational entropy of ordered and disordered Ni_3Al. *Phys. Rev. Lett.*, 80(22):4911–4914, 1998.

[151] A. Van der Ven, V. Bhattacharya, and A. Belak. Understanding Li Diffusion in Li-Intercalation Compounds. *Acc. Chem. Res.*, 46(5):1216–1225, 2013.

[152] A. Van der Ven and G. Ceder. Lithium diffusion mechanisms in layered intercalation compounds. *J. Power Sources*, 97-98(June 2000):529–531, 2001.

[153] A. Van der Ven, G. Ceder, M. Asta, and P. D. Tepesch. First-principles theory of ionic diffusion with nondilute carriers. *Phys. Rev. B*, 64(18):184307, 2001.

[154] P. Verma, P. Maire, and P. Novák. A review of the features and analyses of the solid electrolyte interphase in Li-ion batteries. *Electrochim. Acta*, 55(22):6332–6341, 2010.

[155] J. Vetter, P. Novák, M. R. Wagner, C. Veit, K. C. Möller, J. O. Besenhard, M. Winter, M. Wohlfahrt-Mehrens, C. Vogler, and A. Hammouche. Ageing mechanisms in lithium-ion batteries. *J. Power Sources*, 147(1-2):269–281, 2005.

[156] P. Vinatier, P. Gravereau, M. Menetrier, L. Trut, and A. Levasseur. Li_3BS_3. *Acta Crystallogr. Sect. C*, 50(1990):1180–1183, 1994.

[157] Y. Wang, W. D. Richards, S. P. Ong, L. J. Miara, J. C. Kim, Y. Mo, and G. Ceder. Design principles for solid-state lithium superionic conductors. *Nat. Mater.*, 14(10):1026–1031, 2015.

[158] Y. Wang, R. Xiao, Y.-S. Hu, M. Avdeev, and L. Chen. P2-$Na_{0.6}[Cr_{0.6}Ti_{0.4}]O_2$ cation-disordered electrode for high-rate symmetric rechargeable sodium-ion batteries. *Nat. Commun.*, 6:6954, 2015.

[159] Y. Wang, X. Yu, S. Xu, J. Bai, R. Xiao, Y.-S. Hu, H. Li, X.-Q. Yang, L. Chen, and X. Huang. A zero-strain layered metal oxide as the negative electrode for long-life sodium-ion batteries. *Nat. Commun.*, 4:2635, 2013.

[160] W. Weppner and R. A. Huggins. Ionic conductivity of alkali metal chloroaluminates. *Phys. Lett. A*, 58(4):245–248, 1976.

[161] J. M. Whiteley, J. H. Woo, E. Hu, K.-W. Nam, and S.-H. Lee. Empowering the Lithium Metal Battery through a Silicon-Based Superionic Conductor. *J. Electrochem. Soc.*, 161(12):A1812–A1817, 2014.

[162] M. Winter and J. O. Besenhard. Electrochemical lithiation of tin and tin-based intermetallics and composites. *Electrochim. Acta*, 45(1):31–50, 1999.

[163] W. Xu, J. Wang, F. Ding, X. Chen, E. Nasybulin, Y. Zhang, and J.-G. Zhang. Lithium metal anodes for rechargeable batteries. *Energy Environ. Sci.*, 7(2):513–537, 2014.

[164] H. Yamane, M. Shibata, Y. Shimane, T. Junke, and Y. Seino. Crystal structure of a superionic conductor, $Li_7P_3S_{11}$. *Solid State Ionics*, 178:1163–1167, 2007.

[165] X. Yu, J. Bates, G. Jellison, and F. Hart. A Stable Thin-Film Lithium Electrolyte: Lithium Phosphorus Oxynitride. *J. Electrochem. Soc.*, 144(2):524–532, 1997.

[166] P. Zhang, M. Matsui, Y. Takeda, O. Yamamoto, and N. Imanishi. Water-stable lithium ion conducting solid electrolyte of iron and aluminum doped NASICON-type $LiTi_2(PO_4)_3$. *Solid State Ionics*, 263:27–32, 2014.

[167] W. J. Zhang. A review of the electrochemical performance of alloy anodes for lithium-ion batteries. *J. Power Sources*, 196(1):13–24, 2011.

[168] Y. Zhao and L. Daemen. Superionic conductivity in lithium-rich anti-perovskites. *J. Am. Chem. Soc.*, 134(36):15042–7, 2012.

Appendix A

Methods

A.1 Density Functional Theory (DFT)

The calculation of relevant thermodynamic and transport quantities for crystalline materials is a key part of this thesis. For these calculations, we desire an ab initio methodology - i.e. the energy functional can be determined without fitting to experimental measurements of the system, in contrast to empirical potentials - as they will show better transferability between systems. For all the work in this thesis, we apply Density Functional Theory (DFT) for these calculations. In principle, minimization of the Schrödinger equation (A.1) gives the ground state energy of any arrangement of atoms, but in practice because it must be solved (and minimize) simultaneously for every atom, this problem is computationally tractable only for very small systems.

$$\left[-\frac{\hbar^2\nabla^2}{2m} + v(\mathbf{r})\right]\Psi(\mathbf{r}) = \epsilon\Psi(\mathbf{r}) \tag{A.1}$$

There are numerous references describing DFT in greater detail[32, 17, 26, 47], but a very brief overview is instructive. Instead of simultaneously solving the Schrödinger equation for each electron, DFT reformulates the Schrödinger equation to a single hamiltonian (A.2) that acts on the total electron density. The Hohenberg-Kohn theorem[47] applies the variational principle to prove that the ground state energy of a system of interacting electrons can be completely characterized by its total electron density. The resultant hamiltonian is similar to that of a one-electron system, but under an augmented external potential $v_s(\mathbf{r})$. The additional term $v_H(\mathbf{r})$ is the Hartree potential, which is the electrostatic potential due to electron-electron repulsion, and $v_{xc}(\mathbf{r})$, which describes the exchange and correlation errors due to treating the system as a single particle. The exchange error is due to the electronic self-interaction that is not present in the many-particle case, and the correlation energy is due to Pauli repulsion. In principle, this equation is still exact, but simplifying approximations to these terms are required in order to use this in practice. There have been many advances in developing approximations to these terms, and it is still an area of active research[115, 133, 81, 116].

$$\left[-\frac{\hbar^2\nabla^2}{2m} + v_s(\mathbf{r})\right]\Psi(\mathbf{r}) = \epsilon\Psi(\mathbf{r}) \tag{A.2}$$

$$v_s(\mathbf{r}) = v(\mathbf{r}) + v_H(\mathbf{r}) + v_{xc}(\mathbf{r}) \tag{A.3}$$

$$v_H[n](\mathbf{r}) = q^2 \int \frac{n(\mathbf{r}')}{|\mathbf{r} - \mathbf{r}'|} d^3r' \tag{A.4}$$

A.2 Ab initio molecular dynamics

Ab initio molecular dynamics simulations (AIMD) determines the Li-ion diffusivity by simulating atomic motion at calculating from atom trajectories the diffusivity (D_{Li}) through the Einstein relation (Equation A.5, where d is the dimensionality of the system, t the elapsed time, and $\langle \|\Delta \mathbf{x}\|^2 \rangle$ the mean squared atom displacement). Ionic conductivity is obtained from the diffusivity using the Nernst-Einstein relation (Equation A.6, where $z_{\mathrm{Li}}e$ the charge on a Li^+ ion, c_{Li} is the concentration of Li ions, and T the temperature, and k_{B} Boltzmann's constant).

$$\langle \|\Delta \mathbf{x}\|^2 \rangle = 2dD_{\mathrm{Li}}t \tag{A.5}$$

$$\sigma_{\mathrm{Li}} = \frac{(z_{\mathrm{Li}}e)^2 c_{\mathrm{Li}} D_{\mathrm{Li}}}{k_{\mathrm{B}}T} \tag{A.6}$$

The activation energy for diffusion can be calculated from AIMD by performing simulations at multiple temperatures and fitting the diffusivity to an Arrhenius relation. This allows the extrapolation of high-temperature simulation results to room temperature, which is important because for many materials the conduction process is to slow to directly observe diffusion in reasonable time scales in ab initio simulation. When making these extrapolations, it is important to ensure that the diffusive mechanism of the simulation is the same as at lower temperatures. The most common discrepancies are due to ordering transformations at low T.

A.2.1 MD in highly correlated materials

Calculation of conductivity via the Einstein relation makes the assumption that the diffusion process is relatively uncorrelated between charge carriers. This is typically a good

approximation in simple diffusion mechanisms, for example in vacancy or interstitial diffusion. As diffusion mechanisms become more cooperative, however, this approximation can break down somewhat. This can lead to both overpredictions and underprediction of the true ionic conductivity. This can be understood by considering the extremes of correlation in two hypothetical materials: 1) a material in which ions can only move by swapping places with a neighbor – calculation via the Einstein relation will show an ionic conductivity, even though no net transport can ever occur; 2) a material in which all charge carriers must move in the same direction – the Einstein relation calculates a small diffusivity, but large net motion of ions is easy.

In materials where diffusion of adjacent ions is expected to be highly correlated, the driving force can be calculated by fitting to the mean square displacement of the net Na-ion motion using equation A.7:

$$\langle \| \sum_{i=1}^{n} \Delta \mathbf{x}_i \|^2 \rangle = 2dD_\sigma nt \tag{A.7}$$

Inserting D_σ into the Nernst-Einstein equation is equivalent to using the Green-Kubo expression for ionic conductivity when Na-ions are the only mobile charge carriers[45, 146]. Despite its better generality, this equation can be difficult to fit in practice because obtaining good statistics on the center of mass drift of a system requires much longer simulation time.

The Haven ratio, H_r, an indication of the cooperativity of ionic motion, is calculated from the ratio of D_self to the D_σ in each simulation. The Haven ratio can also be determined through experiment, so can be used to validate the degree of cooperativity in simulation results, even when there are discrepancies in total conductivity, or confounding factors such

as grain boundary resistance.

A.3 Nudged Elastic Band

The nudged elastic band method [62] can be used to investigate the minimum energy pathways between two local minimum (Figure A-1).

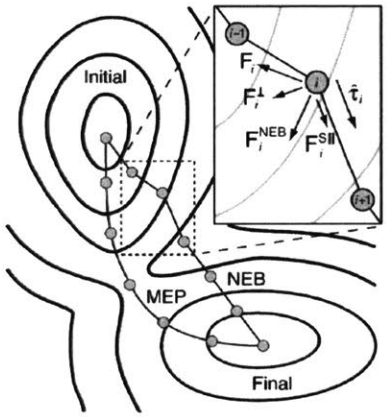

Figure A-1: **The NEB method.** The nudged elastic band method finds the minimum energy pathway (MEP) between local minima by allowing a string of images to relax perpendicular to its direction.[131]

For simple diffusion mechanisms, transition state theory (TST) gives a good approximation of the diffusivity. When there is a single charge carrier whose successive jumps are not well correlated (not ballistic) , diffusion occurs via a random, sequential process of the charge carrier jumping between adjacent lattice sites. On a discrete lattice, diffusivity can be expressed as a function of the lattice parameter and jump frequency:

$$D = \frac{\Gamma r_j^2 f}{2d} \tag{A.8}$$

where Γ is the jump frequency, r_j is the jump distance, d is the dimensionality of the system,

and f is a correlation factor which is introduced to account for the fact that jumps are not entirely random. In some cases, e.g. vacancy mediated diffusion, it is likely that after an atom has jumped to a neighboring vacancy, it will jump back to its original position due to the presence of the recently formed vacancy. In this case the correlation coefficient will have a value between 0 and 1. Similarly (though less frequently), there can be a tendency of a diffusing atom to continue in the direction of its most recent jump, and in this case the coefficient will be greater than 1.

Transition state theory can provide an estimate of this jump frequency Γ, modeling it as an Arrhenius process (equation A.9).

$$\Gamma = A \exp\left(-E_a / k_B T\right) \tag{A.9}$$

To obtain a conductivity from an NEB calculation, the prefactor A, corresponding to the attempt frequency of the hop process, must be determined. This is typically done with a harmonic approximation, but in practice it is often easier to compare trends E_a between different materials, or between NEB and MD calculations.

Appendix B

Interfacial Reactions

Table B.1: **Lithium insertion/extraction of common electrolytes.** Predicted anodic and cathodic reactions for the electrolytes of figure 5-3 at their stability limits.

Anodic reaction (low μ_{Li})	Cathodic reaction (high μ_{Li})
$2\ Li_3BN_2 \rightarrow 2\ BN + N_2$	$Li_3BN_2 \rightarrow Li_3BN_2$
$2\ Li_4NCl \rightarrow N_2 + 2\ LiCl$	$Li_4NCl \rightarrow Li_4NCl$
$6\ LiBH_4 \rightarrow Li_2B_6H_{12} + 9\ H_2$	$6\ LiBH_4 \rightarrow Li_2B_6H_{12} + 18\ LiH$
$Li_3PS_4 \rightarrow Li_2PS_3 + S$	$Li_3PS_4 \rightarrow Li_2PS_3 + Li_2S$
$Li_{10}Ge(PS_6)_2 \rightarrow Li_2GeS_3 + 2\ Li_3PS_4 + S$	$Li_{10}Ge(PS_6)_2 \rightarrow Li_4GeS_4 + 2\ Li_2PS_3 + 2\ Li_2S$
$Li_4SnS_4 \rightarrow S + Li_2SnS_3$	$Li_4SnS_4 \rightarrow 3\ Li_2S + SnS$
$Li_6PS_5Cl \rightarrow S + Li_3PS_4 + LiCl$	$Li_6PS_5Cl \rightarrow LiCl + Li_2PS_3 + 2\ Li_2S$
$5\ LiAlO_2 \rightarrow LiAl_5O_8 + O_2$	$4\ LiAlO_2 \rightarrow Li_3Al_2 + 2\ Li_5AlO_4$
$3\ Li_4Ti_5O_{12} \rightarrow 11\ TiO_2 + 2\ Ti_2O_7$	$5\ Li_4Ti_5O_{12} \rightarrow 3\ Li_5Ti_7O_{16} + 4\ Li_2TiO_3$
$2\ Li_2ZrO_3 \rightarrow 2\ ZrO_2 + O_2$	$7\ Li_2ZrO_3 \rightarrow 3\ Li_6Zr_2O_7 + Zr$
$4\ Li_7La_3Zr_2O_{12} \rightarrow 4\ Li_6Zr_2O_7 + O_2 + 6\ La_2O_3$	$4\ Li_7La_3Zr_2O_{12} \rightarrow 3\ Zr + 6\ La_2O_3 + 5\ Li_8ZrO_6$
$2\ Li_4GeO_4 \rightarrow 2\ Li_2GeO_3 + O_2$	$Li_4GeO_4 \rightarrow 4\ Li_2O + Ge$
$4\ LiNbO_3 \rightarrow O_2 + 2\ Nb_2O_5$	$2\ LiNbO_3 \rightarrow LiNbO_2 + Li_3NbO_4$
$4\ Li_{16}P_5O_{19}N \rightarrow N_2 + 2\ Li_2PO_2N + 18\ Li_3PO_4$	$Li_{16}P_5O_{19}N \rightarrow Li_2PO_2N + 17\ Li_2O + 4\ Li_3P$
$4\ Li_3PO_4 \rightarrow 2\ Li_4P_2O_7 + O_2$	$Li_3PO_4 \rightarrow 4\ Li_2O + Li_3P$
$4\ LiGe_2(PO_4)_3 \rightarrow 2\ GeO_2 + O_2 + 6\ GeP_2O_7$	$2\ LiGe_2(PO_4)_3 \rightarrow 3\ GeO_2 + 6\ LiPO_3 + Ge$
$12\ LiTi_2(PO_4)_3 \rightarrow Ti_5P_6O_{25} + 2\ Ti_2O_7 + 15\ TiP_2O_7$	$LiTi_2(PO_4)_3 \rightarrow Li_2Ti_2(PO_4)_3$
$3\ Li_3ClO \rightarrow ClO_3 + 2\ LiCl$	$Li_3ClO \rightarrow Li_3ClO$

$Li_2MgBr_4 \rightarrow 2\ Br + MgBr_2$	$Li_2MgBr_4 \rightarrow Mg + 4\ LiBr$
$LiAlBr_4 \rightarrow AlBr_3 + Br$	$LiAlBr_4 \rightarrow Al + 4\ LiBr$
$Li_2ZnBr_4 \rightarrow ZnBr_2 + 2\ Br$	$Li_2ZnBr_4 \rightarrow Zn + 4\ LiBr$
$Li_2MnBr_4 \rightarrow MnBr_3 + LiBr$	$Li_2MnBr_4 \rightarrow Mn + 4\ LiBr$
$Li_3InBr_6 \rightarrow 3\ Br + InBr_3$	$Li_3InBr_6 \rightarrow 6\ LiBr + In$
$Li_2MgCl_4 \rightarrow MgCl_2 + Cl_2$	$Li_2MgCl_4 \rightarrow Mg + 4\ LiCl$
$Li_2ZnCl_4 \rightarrow ZnCl_2 + Cl_2$	$Li_2ZnCl_4 \rightarrow Zn + 4\ LiCl$
$2\ LiAlCl_4 \rightarrow 2\ AlCl_3 + Cl_2$	$LiAlCl_4 \rightarrow Al + 4\ LiCl$
$Li_2CdCl_4 \rightarrow CdCl_2 + Cl_2$	$Li_2CdCl_4 \rightarrow 4\ LiCl + Cd$
$2\ LiYF_4 \rightarrow 2\ YF_3 + F_2$	$LiYF_4 \rightarrow 4\ LiF + Y$
$Li_3AlF_6 \rightarrow LiAlF_4 + F_2$	$4\ Li_3AlF_6 \rightarrow 3\ Li_5AlF_8 + Al$
$8\ Li_2ZrF_6 \rightarrow 2\ Li_3Zr_4F_{19} + 5\ F_2$	$4\ Li_2ZrF_6 \rightarrow Zr + 3\ Li_4ZrF_8$

Table B.2: **Interfacial decomposition reactions of common electrolytes.** Predicted decomposition reactions for the electrolytes of figure 5-3 at cathode chemical potentials and mixing reactions with the cathode.

cathode/electrolyte	reaction at cathode voltage	reaction with mixing
$LiBH_4/LiCoO_2$	$2\ LiBH_4 \rightarrow 2\ BH_3 + H_2$	$7\ LiCoO_2 + 4\ LiBH_4 \rightarrow 4\ B(OH)_3 + 2\ H_2O + 7\ Co$
$LiBH_4/LiFePO_4$	$2\ LiBH_4 \rightarrow 2\ BH_3 + H_2$	$3\ LiFePO_4 + 8\ LiBH_4 \rightarrow 3\ FeP + 16\ H_2 + 4\ B_2O_3$
$LiBH_4/LiMnO_2$	$2\ LiBH_4 \rightarrow 2\ BH_3 + H_2$	$3\ LiMnO_2 + 2\ LiBH_4 \rightarrow Mn_3(BO_3)_2 + 4\ H_2$
$LiBH_4/LiNiO_2$	$2\ LiBH_4 \rightarrow H_2 + 2\ BH_3$	$3\ LiNiO_2 + 2\ LiBH_4 \rightarrow 2\ NiH + Ni + 2\ B(OH)_3$
$LiBH_4/LiTiS_2$	none	none
$LiBH_4/LiVS_2$	$6\ LiBH_4 \rightarrow Li(BH)_6 + 9\ H_2$	$57\ LiVS_2 + 10\ LiBH_4 \rightarrow 19\ V_3S_4 + 2\ Li_3B_5(HS_5)_2 + 18\ H_2S$
$LiBH_4/Li_2S$	$6\ LiBH_4 \rightarrow 9\ H_2 + Li(BH)_6$	$19\ Li_2S + 5\ LiBH_4 \rightarrow Li_3B_5(HS_5)_2 + 9\ H_2S$
$Li_3PS_4/LiCoO_2$	$2\ Li_3PS_4 \rightarrow S + P_2S_7$	$3\ LiCoO_2 + 2\ Li_3PS_4 \rightarrow Co(PO_3)_2 + 2\ CoS_2 + 4\ S$
$Li_3PS_4/LiFePO_4$	$2\ Li_3PS_4 \rightarrow P_2S_7 + S$	$2\ Li_3PS_4 \rightarrow P_2S_7 + S$
$Li_3PS_4/LiMnO_2$	$2\ Li_3PS_4 \rightarrow S + P_2S_7$	$14\ LiMnO_2 + 8\ Li_3PS_4 \rightarrow 3\ Mn_2S_3 + 4\ Mn_2P_2O_7 + 23\ S$
$Li_3PS_4/LiNiO_2$	$2\ Li_3PS_4 \rightarrow P_2S_7 + S$	$117\ LiNiO_2 + 44\ Li_3PS_4 \rightarrow 22\ Li_4P_2O_7 + 39\ Ni_3S_4 + 20\ Li_2SO_4$
$Li_3PS_4/LiTiS_2$	$Li_3PS_4 \rightarrow P + 4\ Li_2S$	$Li_3PS_4 \rightarrow 4\ Li_2S + P$
$Li_3PS_4/LiVS_2$	none	none
Li_3PS_4/Li_2S	none	none

$Li_{10}GeP_2S_{12}/LiCoO_2$	$Li_{10}Ge(PS_6)_2 \rightarrow GeS_2 + P_2S_7 + 3\ S$	$7\ LiCoO_2 + 2\ Li_{10}Ge(PS_6)_2 \rightarrow 2\ GeP_2O_7 + 10\ S + 7\ CoS_2$
$Li_{10}GeP_2S_{12}/LiFePO_4$	$Li_{10}Ge(PS_6)_2 \rightarrow 3\ S + P_2S_7 + GeS_2$	$Li_{10}Ge(PS_6)_2 \rightarrow 3\ S + P_2S_7 + GeS_2$
$Li_{10}GeP_2S_{12}/LiMnO_2$	$Li_{10}Ge(PS_6)_2 \rightarrow P_2S_7 + GeS_2 + 3\ S$	$14\ LiMnO_2 + 4\ Li_{10}Ge(PS_6)_2 \rightarrow 4\ Mn_2P_2O_7 + 31\ S + 4\ GeS_2 + 3\ Mn_2S_3$
$Li_{10}GeP_2S_{12}/LiNiO_2$	$Li_{10}Ge(PS_6)_2 \rightarrow 3\ S + P_2S_7 + GeS_2$	$171\ LiNiO_2 + 22\ Li_{10}Ge(PS_6)_2 \rightarrow 36\ Li_2SO_4 + 22\ GeO_2 + 22\ Li_4P_2O_7 + 57\ Ni_3S_4$
$Li_{10}GeP_2S_{12}/LiTiS_2$	$Li_{10}Ge(PS_6)_2 \rightarrow 2\ P + 8\ Li_2S + Li_4GeS_4$	$8\ LiTiS_2 + Li_{10}Ge(PS_6)_2 \rightarrow 2\ P + Li_4GeS_4 + 8\ Li_2TiS_3$
$Li_{10}GeP_2S_{12}/LiVS_2$	none	none
$Li_{10}GeP_2S_{12}/Li_2S$	none	none
$Li_4SnS_4/LiCoO_2$	$Li_4SnS_4 \rightarrow SnS_2 + 2\ S$	$Li_4SnS_4 \rightarrow SnS_2 + 2\ S$
$Li_4SnS_4/LiFePO_4$	$Li_4SnS_4 \rightarrow 2\ S + SnS_2$	$Li_4SnS_4 \rightarrow 2\ S + SnS_2$
$Li_4SnS_4/LiMnO_2$	$Li_4SnS_4 \rightarrow 2\ S + SnS_2$	$Li_4SnS_4 \rightarrow 2\ S + SnS_2$
$Li_4SnS_4/LiNiO_2$	$Li_4SnS_4 \rightarrow SnS_2 + 2\ S$	$27\ LiNiO_2 + 11\ Li_4SnS_4 \rightarrow 11\ SnO_2 + 9\ Ni_3S_4 + 8\ Li_2SO_4$
$Li_4SnS_4/LiTiS_2$	$Li_4SnS_4 \rightarrow 3\ Li_2S + SnS$	$3\ LiTiS_2 + Li_4SnS_4 \rightarrow 3\ Li_2TiS_3 + SnS$
$Li_4SnS_4/LiVS_2$	none	$LiVS_2 + 2\ Li_4SnS_4 \rightarrow 2\ Li_2SnS_3 + Li_3VS_4$
Li_4SnS_4/Li_2S	none	none
$LiAlO_2/LiCoO_2$	$5\ LiAlO_2 \rightarrow LiAl_5O_8 + O_2$	$5\ LiAlO_2 \rightarrow LiAl_5O_8 + O_2$
$LiAlO_2/LiFePO_4$	none	$4\ LiFePO_4 + 15\ LiAlO_2 \rightarrow 4\ Li_3PO_4 + 3\ LiAl_5O_8 + 2\ Fe_2O_3$
$LiAlO_2/LiMnO_2$	none	$7\ LiMnO_2 + 5\ LiAlO_2 \rightarrow LiAl_5O_8 + Li_5Mn_7O_{16}$
$LiAlO_2/LiNiO_2$	none	none
$LiAlO_2/LiTiS_2$	none	$6\ LiTiS_2 + 10\ LiAlO_2 \rightarrow 4\ Li_2TiS_3 + 2\ LiAl_5O_8 + LiTi_2O_4$
$LiAlO_2/LiVS_2$	none	none
$LiAlO_2/Li_2S$	none	none
$LiNbO_3/LiCoO_2$	none	none
$LiNbO_3/LiFePO_4$	none	$2\ LiFePO_4 + 6\ LiNbO_3 \rightarrow Fe_2O_3 + 3\ Nb_2O_5 + 2\ Li_3PO_4$
$LiNbO_3/LiMnO_2$	none	$7\ LiMnO_2 + 4\ LiNbO_3 \rightarrow 2\ Nb_2O_5 + Li_5Mn_7O_{16}$
$LiNbO_3/LiNiO_2$	none	$LiNiO_2 + LiNbO_3 \rightarrow Li_3NbO_4 + NiO$
$LiNbO_3/LiTiS_2$	none	$LiTiS_2 + LiNbO_3 \rightarrow Li_2TiO_3 + LiNbS_2$
$LiNbO_3/LiVS_2$	none	$91\ LiVS_2 + 56\ LiNbO_3 \rightarrow 5\ Li_5(NbS_2)_7 + 21\ Li_2NbV_3O_8 + 28\ Li_3VS_4$
$LiNbO_3/Li_2S$	none	none

$Li_7La_3Zr_2O_{12}/LiCoO_2$	$4\ Li_7La_3Zr_2O_{12} \rightarrow 2\ La_2O_3 + 4\ La_2Zr_2O_7 + 7\ O_2$	$4\ Li_7La_3Zr_2O_{12} \rightarrow 4\ La_2Zr_2O_7 + 7\ O_2 + 2\ La_2O_3$
$Li_7La_3Zr_2O_{12}/LiFePO_4$	$4\ Li_7La_3Zr_2O_{12} \rightarrow 2\ La_2O_3 + 4\ La_2Zr_2O_7 + 7\ Li_2O_2$	$10\ LiFePO_4 + 3\ Li_7La_3Zr_2O_{12} \rightarrow 5\ Fe_2O_3 + 7\ Li_3PO_4 + 3\ LaPO_4 + 3\ La_2Zr_2O_7$
$Li_7La_3Zr_2O_{12}/LiMnO_2$	$4\ Li_7La_3Zr_2O_{12} \rightarrow 8\ LiLaZrO_4 + 5\ Li_2O_2 + 2\ La_2O_3$	$7\ LiMnO_2 + 2\ Li_7La_3Zr_2O_{12} \rightarrow La_2O_3 + 2\ La_2Zr_2O_7 + 7\ Li_2MnO_3$
$Li_7La_3Zr_2O_{12}/LiNiO_2$	$4\ Li_7La_3Zr_2O_{12} \rightarrow 2\ La_2O_3 + 8\ LiLaZrO_4 + 5\ Li_2O_2$	$7\ LiNiO_2 + 2\ Li_7La_3Zr_2O_{12} \rightarrow 2\ La_2Zr_2O_7 + La_2O_3 + 7\ Li_2NiO_3$
$Li_7La_3Zr_2O_{12}/LiTiS_2$	none	$147\ LiTiS_2 + 50\ Li_7La_3Zr_2O_{12} \rightarrow 15\ La_{10}S_{14}O + 72\ ZrO_2 + 28\ Li_2ZrS_3 + 147\ Li_2TiO_3$
$Li_7La_3Zr_2O_{12}/LiVS_2$	none	$63\ LiVS_2 + 36\ Li_7La_3Zr_2O_{12} \rightarrow 72\ ZrO_2 + 8\ La_{10}S_{14}O + 63\ Li_3VO_4 + 14\ La_2SO_2$
$Li_7La_3Zr_2O_{12}/Li_2S$	none	$11\ Li_2S + 4\ Li_7La_3Zr_2O_{12} \rightarrow 6\ La_2SO_2 + 8\ ZrO_2 + 5\ Li_2SO_4$
$Li_{3.2}PO_{3.8}N_{0.2}/LiCoO_2$	$Li_{16}P_5O_{19}N \rightarrow LiPO_3 + 2\ Li_4P_2O_7 + NO_2$	$LiCoO_2 + Li_{16}P_5O_{19}N \rightarrow LiNO_3 + 2\ Li_4P_2O_7 + LiCoPO_4$
$Li_{3.2}PO_{3.8}N_{0.2}/LiFePO_4$	$2\ Li_{16}P_5O_{19}N \rightarrow N_2 + 2\ Li_4P_2O_7 + 6\ Li_3PO_4$	$2\ Li_{16}P_5O_{19}N \rightarrow N_2 + 2\ Li_4P_2O_7 + 6\ Li_3PO_4$
$Li_{3.2}PO_{3.8}N_{0.2}/LiMnO_2$	$2\ Li_{16}P_5O_{19}N \rightarrow 6\ Li_3PO_4 + 2\ Li_4P_2O_7 + N_2$	$LiMnO_2 + 2\ Li_{16}P_5O_{19}N \rightarrow 9\ Li_3PO_4 + N_2 + LiMnPO_4$
$Li_{3.2}PO_{3.8}N_{0.2}/LiNiO_2$	$2\ Li_{16}P_5O_{19}N \rightarrow 6\ Li_3PO_4 + 2\ Li_4P_2O_7 + N_2$	$4\ LiNiO_2 + Li_{16}P_5O_{19}N \rightarrow 5\ Li_3PO_4 + 4\ NiO + LiNO_3$
$Li_{3.2}PO_{3.8}N_{0.2}/LiTiS_2$	$4\ Li_{16}P_5O_{19}N \rightarrow N_2 + 2\ Li_2PO_2N + 18\ Li_3PO_4$	$LiTiS_2 + 2\ Li_{16}P_5O_{19}N \rightarrow 9\ Li_3PO_4 + Li_2PO_2N + TiN + 2\ Li_2S$
$Li_{3.2}PO_{3.8}N_{0.2}/LiVS_2$	$4\ Li_{16}P_5O_{19}N \rightarrow 18\ Li_3PO_4 + 2\ Li_2PO_2N + N_2$	$4\ Li_{16}P_5O_{19}N \rightarrow 18\ Li_3PO_4 + N_2 + 2\ Li_2PO_2N$
$Li_{3.2}PO_{3.8}N_{0.2}/Li_2S$	$4\ Li_{16}P_5O_{19}N \rightarrow 2\ Li_2PO_2N + N_2 + 18\ Li_3PO_4$	$4\ Li_{16}P_5O_{19}N \rightarrow 18\ Li_3PO_4 + 2\ Li_2PO_2N + N_2$
$Li_3PO_4/LiCoO_2$	none	none
$Li_3PO_4/LiFePO_4$	none	none
$Li_3PO_4/LiMnO_2$	none	none
$Li_3PO_4/LiNiO_2$	none	none
$Li_3PO_4/LiTiS_2$	none	none
$Li_3PO_4/LiVS_2$	none	none
Li_3PO_4/Li_2S	none	none

$Li_2MgCl_4/LiCoO_2$	none	$20\ LiCoO_2 + 7\ Li_2MgCl_4 \rightarrow 6\ LiCoCl_4 + 4\ LiClO_3 + 7\ Mg(CoO_2)_2$
$Li_2MgCl_4/LiFePO_4$	none	$2\ LiFePO_4 + 3\ Li_2MgCl_4 \rightarrow 8\ LiCl + Mg_3(PO_4)_2 + 2\ FeCl_2$
$Li_2MgCl_4/LiMnO_2$	none	$11\ LiMnO_2 + 10\ Li_2MgCl_4 \rightarrow 32\ LiCl + 5\ Mg_2MnO_4 + 2\ Mn_3Cl_4O$
$Li_2MgCl_4/LiNiO_2$	none	$2\ LiNiO_2 + 2\ Li_2MgCl_4 \rightarrow Mg_2NiO_3 + NiO + 8\ LiCl$
$Li_2MgCl_4/LiTiS_2$	none	$2\ LiTiS_2 + Li_2MgCl_4 \rightarrow Ti_2S_3 + 4\ LiCl + MgS$
$Li_2MgCl_4/LiVS_2$	none	$3\ LiVS_2 + 2\ Li_2MgCl_4 \rightarrow 8\ LiCl + 2\ MgS + V_3S_4$
Li_2MgCl_4/Li_2S	none	$Li_2S + Li_2MgCl_4 \rightarrow 4\ LiCl + MgS$
$LiAlCl_4/LiCoO_2$	none	$3\ LiCoO_2 + 4\ LiAlCl_4 \rightarrow Li_5CoCl_8 + 2\ Al_2O_3 + 2\ LiCoCl_4$
$LiAlCl_4/LiFePO_4$	none	$LiFePO_4 + LiAlCl_4 \rightarrow AlPO_4 + 2\ LiCl + FeCl_2$
$LiAlCl_4/LiMnO_2$	none	$3\ LiMnO_2 + 4\ LiAlCl_4 \rightarrow 3\ LiMnCl_4 + 2\ Al_2O_3 + 4\ LiCl$
$LiAlCl_4/LiNiO_2$	none	$4\ LiNiO_2 + 5\ LiAlCl_4 \rightarrow 4\ NiCl_2 + 12\ LiCl + LiAl_5O_8$
$LiAlCl_4/LiTiS_2$	none	$4\ LiTiS_2 + LiAlCl_4 \rightarrow LiAlS_2 + 4\ LiCl + 2\ Ti_2S_3$
$LiAlCl_4/LiVS_2$	none	$3\ LiVS_2 + LiAlCl_4 \rightarrow V_3S_4 + 4\ LiCl + LiAlS_2$
$LiAlCl_4/Li_2S$	none	$2\ Li_2S + LiAlCl_4 \rightarrow 4\ LiCl + LiAlS_2$
$LiYF_4/LiCoO_2$	none	none
$LiYF_4/LiFePO_4$	none	none
$LiYF_4/LiMnO_2$	none	none
$LiYF_4/LiNiO_2$	none	$3\ LiNiO_2 + 2\ LiYF_4 \rightarrow Y_2O_3 + 3\ NiO + 8\ LiF$
$LiYF_4/LiTiS_2$	none	none
$LiYF_4/LiVS_2$	none	none
$LiYF_4/Li_2S$	none	none

B.1 Nitrides

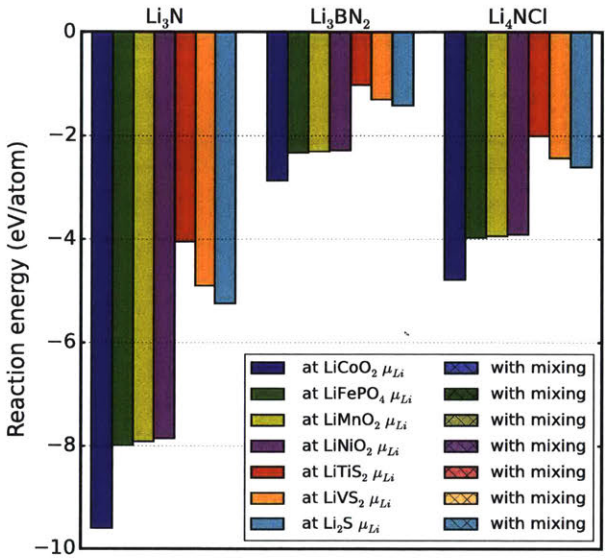

Figure B-1: **Reaction energies for the interfaces of nitride electrolytes.** Calculations performed at μ_{Li} corresponding to the average cathode voltage. Energies are given both for the energy of the lithium extraction only (no mixing) and for energy of cathode/electrolyte mixing open to lithium, following the procedure of figure 5-5.

Table B.3: **Decomposition reactions of nitride electrolytes.** Predicted decomposition reactions for the nitride electrolytes of figure B-1 at cathode chemical potentials and mixing reactions with the cathode.

cathode/electrolyte	reaction at cathode voltage	reaction with mixing
$Li_3N/LiCoO_2$	$2\ Li_3N \rightarrow N_2$	$2\ Li_3N \rightarrow N_2$
$Li_3N/LiFePO_4$	$2\ Li_3N \rightarrow N_2$	$2\ Li_3N \rightarrow N_2$
$Li_3N/LiMnO_2$	$2\ Li_3N \rightarrow N_2$	$2\ Li_3N \rightarrow N_2$
$Li_3N/LiNiO_2$	$2\ Li_3N \rightarrow N_2$	$2\ Li_3N \rightarrow N_2$
$Li_3N/LiTiS_2$	$2\ Li_3N \rightarrow N_2$	$2\ Li_3N \rightarrow N_2$
$Li_3N/LiVS_2$	$2\ Li_3N \rightarrow N_2$	$2\ Li_3N \rightarrow N_2$
Li_3N/Li_2S	$2\ Li_3N \rightarrow N_2$	$2\ Li_3N \rightarrow N_2$
$Li_3BN_2/LiCoO_2$	$2\ Li_3BN_2 \rightarrow 2\ BN + N_2$	$2\ Li_3BN_2 \rightarrow 2\ BN + N_2$
$Li_3BN_2/LiFePO_4$	$2\ Li_3BN_2 \rightarrow 2\ BN + N_2$	$2\ Li_3BN_2 \rightarrow 2\ BN + N_2$
$Li_3BN_2/LiMnO_2$	$2\ Li_3BN_2 \rightarrow N_2 + 2\ BN$	$2\ Li_3BN_2 \rightarrow 2\ BN + N_2$
$Li_3BN_2/LiNiO_2$	$2\ Li_3BN_2 \rightarrow N_2 + 2\ BN$	$2\ Li_3BN_2 \rightarrow 2\ BN + N_2$
$Li_3BN_2/LiTiS_2$	$2\ Li_3BN_2 \rightarrow 2\ BN + N_2$	$2\ Li_3BN_2 \rightarrow 2\ BN + N_2$
$Li_3BN_2/LiVS_2$	$2\ Li_3BN_2 \rightarrow N_2 + 2\ BN$	$2\ Li_3BN_2 \rightarrow N_2 + 2\ BN$
Li_3BN_2/Li_2S	$2\ Li_3BN_2 \rightarrow 2\ BN + N_2$	$2\ Li_3BN_2 \rightarrow 2\ BN + N_2$
$Li_4NCl/LiCoO_2$	$2\ Li_4NCl \rightarrow N_2 + 2\ LiCl$	$2\ Li_4NCl \rightarrow 2\ LiCl + N_2$
$Li_4NCl/LiFePO_4$	$2\ Li_4NCl \rightarrow 2\ LiCl + N_2$	$2\ Li_4NCl \rightarrow 2\ LiCl + N_2$
$Li_4NCl/LiMnO_2$	$2\ Li_4NCl \rightarrow 2\ LiCl + N_2$	$2\ Li_4NCl \rightarrow N_2 + 2\ LiCl$
$Li_4NCl/LiNiO_2$	$2\ Li_4NCl \rightarrow N_2 + 2\ LiCl$	$2\ Li_4NCl \rightarrow 2\ LiCl + N_2$
$Li_4NCl/LiTiS_2$	$2\ Li_4NCl \rightarrow N_2 + 2\ LiCl$	$2\ Li_4NCl \rightarrow N_2 + 2\ LiCl$
$Li_4NCl/LiVS_2$	$2\ Li_4NCl \rightarrow N_2 + 2\ LiCl$	$2\ Li_4NCl \rightarrow 2\ LiCl + N_2$
Li_4NCl/Li_2S	$2\ Li_4NCl \rightarrow N_2 + 2\ LiCl$	$2\ Li_4NCl \rightarrow N_2 + 2\ LiCl$

B.2 Hydrides

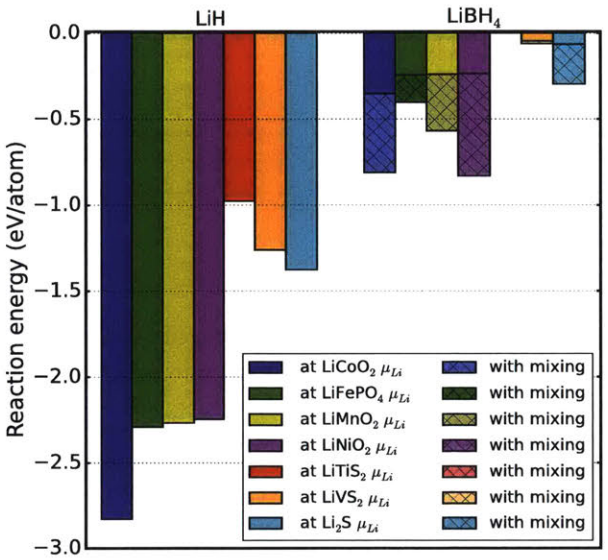

Figure B-2: **Reaction energies for the interfaces of hydride electrolytes.** Calculations performed at μ_{Li} corresponding to the average cathode voltage. Energies are given both for the energy of the lithium extraction only (no mixing) and for energy of cathode/electrolyte mixing open to lithium, following the procedure of figure 5-5.

Table B.4: **Decomposition reactions of hydride electrolytes.** Predicted decomposition reactions for the hydride electrolytes of figure B-2 at cathode chemical potentials and mixing reactions with the cathode.

cathode/electrolyte	reaction at cathode voltage	reaction with mixing
$LiH/LiCoO_2$	$2\ LiH \rightarrow H_2$	$2\ LiH \rightarrow H_2$
$LiH/LiFePO_4$	$2\ LiH \rightarrow H_2$	$2\ LiH \rightarrow H_2$
$LiH/LiMnO_2$	$2\ LiH \rightarrow H_2$	$2\ LiH \rightarrow H_2$
$LiH/LiNiO_2$	$2\ LiH \rightarrow H_2$	$2\ LiH \rightarrow H_2$
$LiH/LiTiS_2$	$2\ LiH \rightarrow H_2$	$2\ LiH \rightarrow H_2$
$LiH/LiVS_2$	$2\ LiH \rightarrow H_2$	$2\ LiH \rightarrow H_2$
LiH/Li_2S	$2\ LiH \rightarrow H_2$	$2\ LiH \rightarrow H_2$
$LiBH_4/LiCoO_2$	$2\ LiBH_4 \rightarrow 2\ BH_3 + H_2$	$7\ LiCoO_2 + 4\ LiBH_4 \rightarrow 4\ B(OH)_3 + 2\ H_2O + 7\ Co$
$LiBH_4/LiFePO_4$	$2\ LiBH_4 \rightarrow 2\ BH_3 + H_2$	$3\ LiFePO_4 + 8\ LiBH_4 \rightarrow 16\ H_2 + 4\ B_2O_3 + 3\ FeP$
$LiBH_4/LiMnO_2$	$2\ LiBH_4 \rightarrow H_2 + 2\ BH_3$	$3\ LiMnO_2 + 2\ LiBH_4 \rightarrow 4\ H_2 + Mn_3(BO_3)_2$
$LiBH_4/LiNiO_2$	$2\ LiBH_4 \rightarrow H_2 + 2\ BH_3$	$3\ LiNiO_2 + 2\ LiBH_4 \rightarrow Ni + 2\ NiH + 2\ B(OH)_3$
$LiBH_4/LiTiS_2$	none	none
$LiBH_4/LiVS_2$	$6\ LiBH_4 \rightarrow 9\ H_2 + Li(BH)_6$	$57\ LiVS_2 + 10\ LiBH_4 \rightarrow 2\ Li_3B_5(HS_5)_2 + 19\ V_3S_4 + 18\ H_2S$
$LiBH_4/Li_2S$	$6\ LiBH_4 \rightarrow 9\ H_2 + Li(BH)_6$	$19\ Li_2S + 5\ LiBH_4 \rightarrow Li_3B_5(HS_5)_2 + 9\ H_2S$

B.3 Sulfides

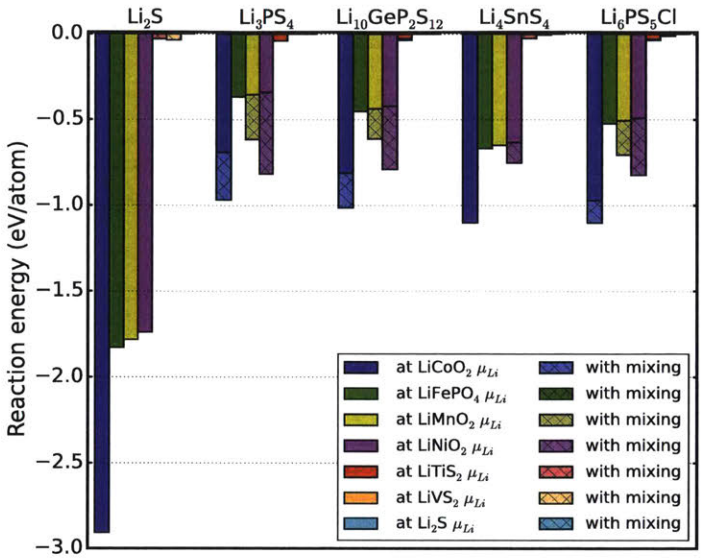

Figure B-3: **Reaction energies for the interfaces of sulfide electrolytes.** Calculations performed at μ_{Li} corresponding to the average cathode voltage. Energies are given both for the energy of the lithium extraction only (no mixing) and for energy of cathode/electrolyte mixing open to lithium, following the procedure of figure 5-5.

Table B.5: **Decomposition reactions of sulfide electrolytes.** Predicted decomposition reactions for the sulfide electrolytes of figure B-3 at cathode chemical potentials and mixing reactions with the cathode.

cathode/electrolyte	reaction at cathode voltage	reaction with mixing
$Li_2S/LiCoO_2$	$Li_2S \rightarrow S$	$Li_2S \rightarrow S$
$Li_2S/LiFePO_4$	$Li_2S \rightarrow S$	$Li_2S \rightarrow S$
$Li_2S/LiMnO_2$	$Li_2S \rightarrow S$	$Li_2S \rightarrow S$
$Li_2S/LiNiO_2$	$Li_2S \rightarrow S$	$Li_2S \rightarrow S$
$Li_2S/LiTiS_2$	none	$LiTiS_2 + Li_2S \rightarrow Li_2TiS_3$
$Li_2S/LiVS_2$	none	$LiVS_2 + 2\ Li_2S \rightarrow Li_3VS_4$
Li_2S/Li_2S	none	none
$Li_3PS_4/LiCoO_2$	$2\ Li_3PS_4 \rightarrow P_2S_7 + S$	$3\ LiCoO_2 + 2\ Li_3PS_4 \rightarrow 4\ S + 2\ CoS_2 + Co(PO_3)_2$
$Li_3PS_4/LiFePO_4$	$2\ Li_3PS_4 \rightarrow P_2S_7 + S$	$2\ Li_3PS_4 \rightarrow P_2S_7 + S$
$Li_3PS_4/LiMnO_2$	$2\ Li_3PS_4 \rightarrow S + P_2S_7$	$14\ LiMnO_2 + 8\ Li_3PS_4 \rightarrow 23\ S + 3\ Mn_2S_3 + 4\ Mn_2P_2O_7$
$Li_3PS_4/LiNiO_2$	$2\ Li_3PS_4 \rightarrow P_2S_7 + S$	$117\ LiNiO_2 + 44\ Li_3PS_4 \rightarrow 39\ Ni_3S_4 + 22\ Li_4P_2O_7 + 20\ Li_2SO_4$
$Li_3PS_4/LiTiS_2$	$Li_3PS_4 \rightarrow 4\ Li_2S + P$	$Li_3PS_4 \rightarrow P + 4\ Li_2S$
$Li_3PS_4/LiVS_2$	none	none
Li_3PS_4/Li_2S	none	none
$Li_{10}GeP_2S_{12}/LiCoO_2$	$Li_{10}Ge(PS_6)_2 \rightarrow P_2S_7 + GeS_2 + 3\ S$	$7\ LiCoO_2 + 2\ Li_{10}Ge(PS_6)_2 \rightarrow 10\ S + 7\ CoS_2 + 2\ GeP_2O_7$
$Li_{10}GeP_2S_{12}/LiFePO_4$	$Li_{10}Ge(PS_6)_2 \rightarrow P_2S_7 + GeS_2 + 3\ S$	$Li_{10}Ge(PS_6)_2 \rightarrow P_2S_7 + 3\ S + GeS_2$
$Li_{10}GeP_2S_{12}/LiMnO_2$	$Li_{10}Ge(PS_6)_2 \rightarrow GeS_2 + P_2S_7 + 3\ S$	$14\ LiMnO_2 + 4\ Li_{10}Ge(PS_6)_2 \rightarrow 4\ GeS_2 + 31\ S + 4\ Mn_2P_2O_7 + 3\ Mn_2S_3$
$Li_{10}GeP_2S_{12}/LiNiO_2$	$Li_{10}Ge(PS_6)_2 \rightarrow P_2S_7 + GeS_2 + 3\ S$	$171\ LiNiO_2 + 22\ Li_{10}Ge(PS_6)_2 \rightarrow 22\ Li_4P_2O_7 + 22\ GeO_2 + 36\ Li_2SO_4 + 57\ Ni_3S_4$
$Li_{10}GeP_2S_{12}/LiTiS_2$	$Li_{10}Ge(PS_6)_2 \rightarrow Li_4GeS_4 + 8\ Li_2S + 2\ P$	$8\ LiTiS_2 + Li_{10}Ge(PS_6)_2 \rightarrow Li_4GeS_4 + 2\ P + 8\ Li_2TiS_3$
$Li_{10}GeP_2S_{12}/LiVS_2$	none	none
$Li_{10}GeP_2S_{12}/Li_2S$	none	none
$Li_4SnS_4/LiCoO_2$	$Li_4SnS_4 \rightarrow SnS_2 + 2\ S$	$Li_4SnS_4 \rightarrow SnS_2 + 2\ S$
$Li_4SnS_4/LiFePO_4$	$Li_4SnS_4 \rightarrow SnS_2 + 2\ S$	$Li_4SnS_4 \rightarrow SnS_2 + 2\ S$
$Li_4SnS_4/LiMnO_2$	$Li_4SnS_4 \rightarrow SnS_2 + 2\ S$	$Li_4SnS_4 \rightarrow 2\ S + SnS_2$
$Li_4SnS_4/LiNiO_2$	$Li_4SnS_4 \rightarrow SnS_2 + 2\ S$	$27\ LiNiO_2 + 11\ Li_4SnS_4 \rightarrow 8\ Li_2SO_4 + 11\ SnO_2 + 9\ Ni_3S_4$
$Li_4SnS_4/LiTiS_2$	$Li_4SnS_4 \rightarrow 3\ Li_2S + SnS$	$3\ LiTiS_2 + Li_4SnS_4 \rightarrow 3\ Li_2TiS_3 + SnS$
$Li_4SnS_4/LiVS_2$	none	$LiVS_2 + 2\ Li_4SnS_4 \rightarrow Li_3VS_4 + 2\ Li_2SnS_3$
Li_4SnS_4/Li_2S	none	none

$Li_6PS_5Cl/LiCoO_2$	$2\ Li_6PS_5Cl \rightarrow 2\ SCl + P_2S_7 + S$	$11\ LiCoO_2 + 8\ Li_6PS_5Cl \rightarrow 8\ CoSCl + 30\ S + 2\ CoP_4O_{11} + CoS_2$
$Li_6PS_5Cl/LiFePO_4$	$2\ Li_6PS_5Cl \rightarrow 3\ S + P_2S_7 + 2\ LiCl$	$2\ Li_6PS_5Cl \rightarrow 3\ S + 2\ LiCl + P_2S_7$
$Li_6PS_5Cl/LiMnO_2$	$2\ Li_6PS_5Cl \rightarrow 3\ S + P_2S_7 + 2\ LiCl$	$2\ LiMnO_2 + Li_6PS_5Cl \rightarrow Mn_2PClO_4 + 5\ S$
$Li_6PS_5Cl/LiNiO_2$	$2\ Li_6PS_5Cl \rightarrow 3\ S + P_2S_7 + 2\ LiCl$	$21\ LiNiO_2 + 12\ Li_6PS_5Cl \rightarrow 40\ S + 6\ Li_4P_2O_7 + 5\ Ni_3S_4 + 6\ NiCl_2$
$Li_6PS_5Cl/LiTiS_2$	$Li_6PS_5Cl \rightarrow 5\ Li_2S + P + LiCl$	$5\ LiTiS_2 + Li_6PS_5Cl \rightarrow LiCl + 5\ Li_2TiS_3 + P$
$Li_6PS_5Cl/LiVS_2$	none	$LiVS_2 + 2\ Li_6PS_5Cl \rightarrow 2\ LiCl + 2\ Li_3PS_4 + Li_3VS_4$
Li_6PS_5Cl/Li_2S	none	none

B.4 Oxides

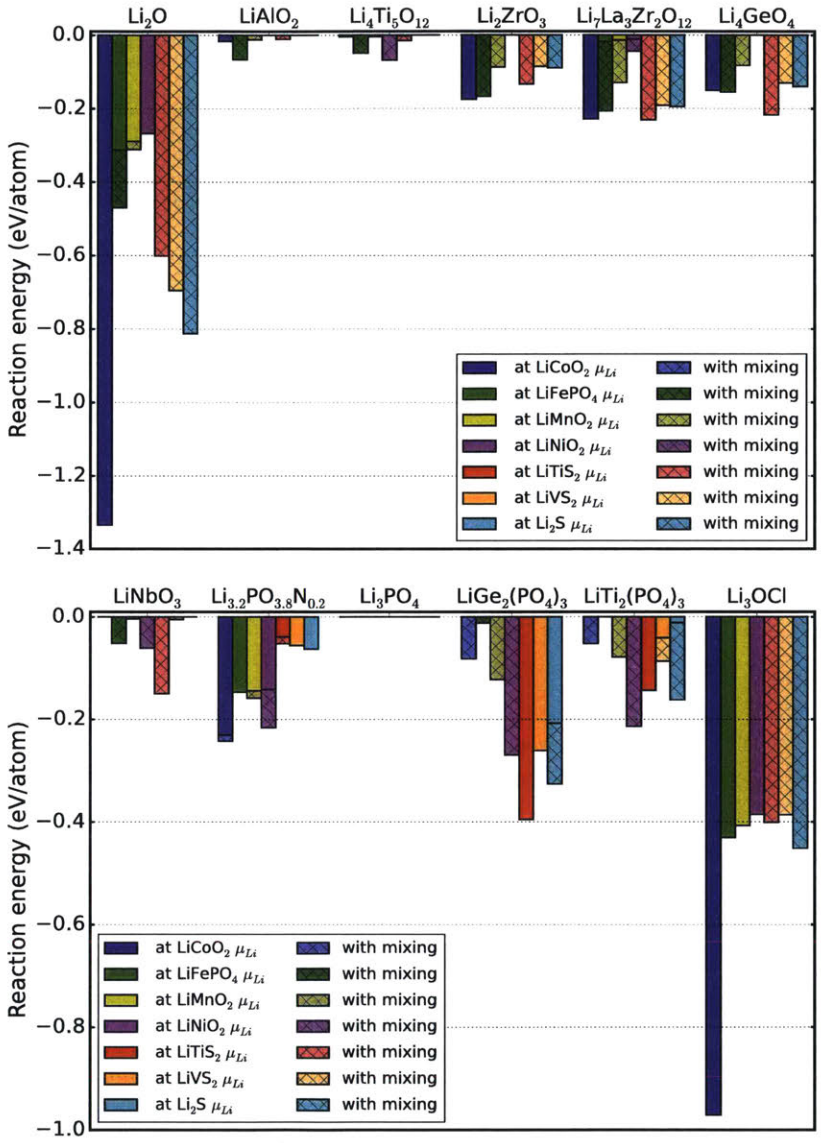

Figure B-4: **Reaction energies for the interfaces of oxide electrolytes.** Calculations performed at at μ_{Li} corresponding to the average cathode voltage. Energies are given both for the energy of the lithium extraction only (no mixing) and for energy of cathode/electrolyte mixing open to lithium, following the procedure of figure 5-5.

Table B.6: **Decomposition reactions of oxide electrolytes.** Predicted decomposition reactions for the oxide electrolytes of figure B-4 at cathode chemical potentials and mixing reactions with the cathode.

cathode/electrolyte	reaction at cathode voltage	reaction with mixing
$Li_2O/LiCoO_2$	$2\ Li_2O \rightarrow O_2$	$2\ Li_2O \rightarrow O_2$
$Li_2O/LiFePO_4$	$2\ Li_2O \rightarrow Li_2O_2$	$LiFePO_4 + 4\ Li_2O \rightarrow Li_3PO_4 + Li_3FeO_4$
$Li_2O/LiMnO_2$	$2\ Li_2O \rightarrow Li_2O_2$	$LiMnO_2 + Li_2O \rightarrow Li_2MnO_3$
$Li_2O/LiNiO_2$	$2\ Li_2O \rightarrow Li_2O_2$	$2\ Li_2O \rightarrow Li_2O_2$
$Li_2O/LiTiS_2$	none	$LiTiS_2 + 3\ Li_2O \rightarrow 2\ Li_2S + Li_2TiO_3$
$Li_2O/LiVS_2$	none	$LiVS_2 + 12\ Li_2O \rightarrow 2\ Li_2SO_4 + Li_3VO_4$
Li_2O/Li_2S	none	$Li_2S + 4\ Li_2O \rightarrow Li_2SO_4$
$LiAlO_2/LiCoO_2$	$5\ LiAlO_2 \rightarrow LiAl_5O_8 + O_2$	$5\ LiAlO_2 \rightarrow LiAl_5O_8 + O_2$
$LiAlO_2/LiFePO_4$	none	$4\ LiFePO_4 + 15\ LiAlO_2 \rightarrow 2\ Fe_2O_3 + 4\ Li_3PO_4 + 3\ LiAl_5O_8$
$LiAlO_2/LiMnO_2$	none	$7\ LiMnO_2 + 5\ LiAlO_2 \rightarrow LiAl_5O_8 + Li_5Mn_7O_{16}$
$LiAlO_2/LiNiO_2$	none	none
$LiAlO_2/LiTiS_2$	none	$6\ LiTiS_2 + 10\ LiAlO_2 \rightarrow LiTi_2O_4 + 2\ LiAl_5O_8 + 4\ Li_2TiS_3$
$LiAlO_2/LiVS_2$	none	none
$LiAlO_2/Li_2S$	none	none
$Li_4Ti_5O_{12}/LiCoO_2$	$3\ Li_4Ti_5O_{12} \rightarrow 2\ Ti_2O_7 + 11\ TiO_2$	$3\ Li_4Ti_5O_{12} \rightarrow 2\ Ti_2O_7 + 11\ TiO_2$
$Li_4Ti_5O_{12}/LiFePO_4$	none	$4\ LiFePO_4 + 3\ Li_4Ti_5O_{12} \rightarrow 15\ TiO_2 + 4\ Li_3PO_4 + 2\ Fe_2O_3$
$Li_4Ti_5O_{12}/LiMnO_2$	none	$7\ LiMnO_2 + Li_4Ti_5O_{12} \rightarrow Li_5Mn_7O_{16} + 5\ TiO_2$
$Li_4Ti_5O_{12}/LiNiO_2$	none	$3\ LiNiO_2 + Li_4Ti_5O_{12} \rightarrow 3\ NiO + 5\ Li_2TiO_3$
$Li_4Ti_5O_{12}/LiTiS_2$	$5\ Li_4Ti_5O_{12} \rightarrow 4\ Li_2TiO_3 + 3\ Li_5Ti_7O_{16}$	$3\ LiTiS_2 + Li_4Ti_5O_{12} \rightarrow 2\ Li_2TiS_3 + 3\ LiTi_2O_4$
$Li_4Ti_5O_{12}/LiVS_2$	none	none
$Li_4Ti_5O_{12}/Li_2S$	none	none
$Li_2ZrO_3/LiCoO_2$	$2\ Li_2ZrO_3 \rightarrow 2\ ZrO_2 + O_2$	$2\ Li_2ZrO_3 \rightarrow O_2 + 2\ ZrO_2$
$Li_2ZrO_3/LiFePO_4$	none	$2\ LiFePO_4 + 3\ Li_2ZrO_3 \rightarrow Fe_2O_3 + 3\ ZrO_2 + 2\ Li_3PO_4$
$Li_2ZrO_3/LiMnO_2$	none	$LiMnO_2 + Li_2ZrO_3 \rightarrow ZrO_2 + Li_2MnO_3$
$Li_2ZrO_3/LiNiO_2$	none	none
$Li_2ZrO_3/LiTiS_2$	none	$21\ LiTiS_2 + 20\ Li_2ZrO_3 \rightarrow 6\ ZrO_2 + 14\ Li_2ZrS_3 + 3\ Li_5Ti_7O_{16}$
$Li_2ZrO_3/LiVS_2$	none	$3\ LiVS_2 + 8\ Li_2ZrO_3 \rightarrow 2\ Li_2ZrS_3 + 6\ ZrO_2 + 3\ Li_3VO_4$
Li_2ZrO_3/Li_2S	none	$Li_2S + 4\ Li_2ZrO_3 \rightarrow Li_2SO_4 + 4\ ZrO_2$

$Li_7La_3Zr_2O_{12}/LiCoO_2$	$4\ Li_7La_3Zr_2O_{12} \rightarrow 7\ O_2 + 4\ La_2Zr_2O_7 + 2\ La_2O_3$	$4\ Li_7La_3Zr_2O_{12} \rightarrow 7\ O_2 + 2\ La_2O_3 + 4\ La_2Zr_2O_7$
$Li_7La_3Zr_2O_{12}/LiFePO_4$	$4\ Li_7La_3Zr_2O_{12} \rightarrow 2\ La_2O_3 + 4\ La_2Zr_2O_7 + 7\ Li_2O_2$	$10\ LiFePO_4 + 3\ Li_7La_3Zr_2O_{12} \rightarrow 7\ Li_3PO_4 + 3\ LaPO_4 + 5\ Fe_2O_3 + 3\ La_2Zr_2O_7$
$Li_7La_3Zr_2O_{12}/LiMnO_2$	$4\ Li_7La_3Zr_2O_{12} \rightarrow 8\ LiLaZrO_4 + 5\ Li_2O_2 + 2\ La_2O_3$	$7\ LiMnO_2 + 2\ Li_7La_3Zr_2O_{12} \rightarrow La_2O_3 + 7\ Li_2MnO_3 + 2\ La_2Zr_2O_7$
$Li_7La_3Zr_2O_{12}/LiNiO_2$	$4\ Li_7La_3Zr_2O_{12} \rightarrow 8\ LiLaZrO_4 + 5\ Li_2O_2 + 2\ La_2O_3$	$7\ LiNiO_2 + 2\ Li_7La_3Zr_2O_{12} \rightarrow 2\ La_2Zr_2O_7 + 7\ Li_2NiO_3 + La_2O_3$
$Li_7La_3Zr_2O_{12}/LiTiS_2$	none	$147\ LiTiS_2 + 50\ Li_7La_3Zr_2O_{12} \rightarrow 28\ Li_2ZrS_3 + 72\ ZrO_2 + 15\ La_{10}S_{14}O + 147\ Li_2TiO_3$
$Li_7La_3Zr_2O_{12}/LiVS_2$	none	$63\ LiVS_2 + 36\ Li_7La_3Zr_2O_{12} \rightarrow 8\ La_{10}S_{14}O + 72\ ZrO_2 + 14\ La_2SO_2 + 63\ Li_3VO_4$
$Li_7La_3Zr_2O_{12}/Li_2S$	none	$11\ Li_2S + 4\ Li_7La_3Zr_2O_{12} \rightarrow 8\ ZrO_2 + 6\ La_2SO_2 + 5\ Li_2SO_4$
$Li_4GeO_4/LiCoO_2$	$2\ Li_4GeO_4 \rightarrow 2\ Li_2GeO_3 + O_2$	$2\ Li_4GeO_4 \rightarrow O_2 + 2\ Li_2GeO_3$
$Li_4GeO_4/LiFePO_4$	none	$16\ LiFePO_4 + 15\ Li_4GeO_4 \rightarrow 8\ Fe_2O_3 + 3\ Li_4Ge_5O_{12} + 16\ Li_3PO_4$
$Li_4GeO_4/LiMnO_2$	none	$LiMnO_2 + Li_4GeO_4 \rightarrow Li_2GeO_3 + Li_2MnO_3$
$Li_4GeO_4/LiNiO_2$	none	none
$Li_4GeO_4/LiTiS_2$	none	$4\ LiTiS_2 + 3\ Li_4GeO_4 \rightarrow 4\ Li_2TiO_3 + Ge + 2\ Li_4GeS_4$
$Li_4GeO_4/LiVS_2$	none	$15\ LiVS_2 + 10\ Li_4GeO_4 \rightarrow 10\ Li_2GeS_3 + 4\ V_2O_3 + 7\ Li_3VO_4$
Li_4GeO_4/Li_2S	none	$5\ Li_2S + Li_4GeO_4 \rightarrow Li_2SO_4 + Li_4GeS_4$
$LiNbO_3/LiCoO_2$	none	none
$LiNbO_3/LiFePO_4$	none	$2\ LiFePO_4 + 6\ LiNbO_3 \rightarrow 3\ Nb_2O_5 + 2\ Li_3PO_4 + Fe_2O_3$
$LiNbO_3/LiMnO_2$	none	$7\ LiMnO_2 + 4\ LiNbO_3 \rightarrow Li_5Mn_7O_{16} + 2\ Nb_2O_5$
$LiNbO_3/LiNiO_2$	none	$LiNiO_2 + LiNbO_3 \rightarrow NiO + Li_3NbO_4$
$LiNbO_3/LiTiS_2$	none	$LiTiS_2 + LiNbO_3 \rightarrow Li_2TiO_3 + LiNbS_2$
$LiNbO_3/LiVS_2$	none	$91\ LiVS_2 + 56\ LiNbO_3 \rightarrow 5\ Li_5(NbS_2)_7 + 21\ Li_2NbV_3O_8 + 28\ Li_3VS_4$
$LiNbO_3/Li_2S$	none	none

$Li_{3.2}PO_{3.8}N_{0.2}/LiCoO_2$	$Li_{16}P_5O_{19}N \rightarrow 2\ Li_4P_2O_7 + NO_2 + LiPO_3$	$LiCoO_2 + Li_{16}P_5O_{19}N \rightarrow LiCoPO_4 + LiNO_3 + 2\ Li_4P_2O_7$
$Li_{3.2}PO_{3.8}N_{0.2}/LiFePO_4$	$2\ Li_{16}P_5O_{19}N \rightarrow 2\ Li_4P_2O_7 + N_2 + 6\ Li_3PO_4$	$2\ Li_{16}P_5O_{19}N \rightarrow 6\ Li_3PO_4 + N_2 + 2\ Li_4P_2O_7$
$Li_{3.2}PO_{3.8}N_{0.2}/LiMnO_2$	$2\ Li_{16}P_5O_{19}N \rightarrow 6\ Li_3PO_4 + 2\ Li_4P_2O_7 + N_2$	$LiMnO_2 + 2\ Li_{16}P_5O_{19}N \rightarrow LiMnPO_4 + 9\ Li_3PO_4 + N_2$
$Li_{3.2}PO_{3.8}N_{0.2}/LiNiO_2$	$2\ Li_{16}P_5O_{19}N \rightarrow 2\ Li_4P_2O_7 + N_2 + 6\ Li_3PO_4$	$4\ LiNiO_2 + Li_{16}P_5O_{19}N \rightarrow LiNO_3 + 5\ Li_3PO_4 + 4\ NiO$
$Li_{3.2}PO_{3.8}N_{0.2}/LiTiS_2$	$4\ Li_{16}P_5O_{19}N \rightarrow N_2 + 2\ Li_2PO_2N + 18\ Li_3PO_4$	$LiTiS_2 + 2\ Li_{16}P_5O_{19}N \rightarrow 2\ Li_2S + 9\ Li_3PO_4 + TiN + Li_2PO_2N$
$Li_{3.2}PO_{3.8}N_{0.2}/LiVS_2$	$4\ Li_{16}P_5O_{19}N \rightarrow N_2 + 2\ Li_2PO_2N + 18\ Li_3PO_4$	$4\ Li_{16}P_5O_{19}N \rightarrow N_2 + 18\ Li_3PO_4 + 2\ Li_2PO_2N$
$Li_{3.2}PO_{3.8}N_{0.2}/Li_2S$	$4\ Li_{16}P_5O_{19}N \rightarrow 18\ Li_3PO_4 + 2\ Li_2PO_2N + N_2$	$4\ Li_{16}P_5O_{19}N \rightarrow 18\ Li_3PO_4 + 2\ Li_2PO_2N + N_2$
$Li_3PO_4/LiCoO_2$	none	none
$Li_3PO_4/LiFePO_4$	none	none
$Li_3PO_4/LiMnO_2$	none	none
$Li_3PO_4/LiNiO_2$	none	none
$Li_3PO_4/LiTiS_2$	none	none
$Li_3PO_4/LiVS_2$	none	none
Li_3PO_4/Li_2S	none	none
$LiGe_2(PO_4)_3/LiCoO_2$	none	$6\ LiCoO_2 + LiGe_2(PO_4)_3 \rightarrow 2\ Co_3O_4 + 2\ GeO_2 + 3\ Li_3PO_4$
$LiGe_2(PO_4)_3/LiFePO_4$	none	$5\ LiFePO_4 + LiGe_2(PO_4)_3 \rightarrow 3\ LiFeP_2O_7 + Fe_2P_2O_7 + 2\ GeO_2$
$LiGe_2(PO_4)_3/LiMnO_2$	none	$2\ LiMnO_2 + LiGe_2(PO_4)_3 \rightarrow 2\ LiMnPO_4 + 2\ GeO_2 + Li_3PO_4$
$LiGe_2(PO_4)_3/LiNiO_2$	none	$4\ LiNiO_2 + LiGe_2(PO_4)_3 \rightarrow 2\ Ni_2GeO_4 + 3\ Li_3PO_4$
$LiGe_2(PO_4)_3/LiTiS_2$	$LiGe_2(PO_4)_3 \rightarrow 2\ Ge + 3\ Li_3PO_4$	$LiGe_2(PO_4)_3 \rightarrow 2\ Ge + 3\ Li_3PO_4$
$LiGe_2(PO_4)_3/LiVS_2$	$LiGe_2(PO_4)_3 \rightarrow 3\ Li_3PO_4 + 2\ Ge$	$LiGe_2(PO_4)_3 \rightarrow 2\ Ge + 3\ Li_3PO_4$
$LiGe_2(PO_4)_3/Li_2S$	$LiGe_2(PO_4)_3 \rightarrow 2\ Ge + 3\ Li_3PO_4$	$6\ Li_2S + LiGe_2(PO_4)_3 \rightarrow 2\ Li_2GeS_3 + 3\ Li_3PO_4$

$LiTi_2(PO_4)_3/LiCoO_2$	none	$6\ LiCoO_2 + LiTi_2(PO_4)_3 \rightarrow 3\ Li_3PO_4 + 2\ TiO_2 + 2\ Co_3O_4$
$LiTi_2(PO_4)_3/LiFePO_4$	none	none
$LiTi_2(PO_4)_3/LiMnO_2$	none	$3\ LiMnO_2 + LiTi_2(PO_4)_3 \rightarrow LiMnPO_4 + 2\ Li_3PO_4 + 2\ TiMnO_3$
$LiTi_2(PO_4)_3/LiNiO_2$	none	$4\ LiNiO_2 + LiTi_2(PO_4)_3 \rightarrow 3\ Li_3PO_4 + 2\ Ti(NiO_2)_2$
$LiTi_2(PO_4)_3/LiTiS_2$	$3\ LiTi_2(PO_4)_3 \rightarrow 2\ LiTi_2O_4 + 7\ Li_3PO_4 + 2\ TiP$	$3\ LiTi_2(PO_4)_3 \rightarrow 2\ LiTi_2O_4 + 7\ Li_3PO_4 + 2\ TiP$
$LiTi_2(PO_4)_3/LiVS_2$	$5\ LiTi_2(PO_4)_3 \rightarrow 2\ TiP_2 + 8\ TiO_2 + 11\ Li_3PO_4$	$6\ LiVS_2 + LiTi_2(PO_4)_3 \rightarrow 2\ V_3S_4 + 2\ TiS_2 + 3\ Li_3PO_4$
$LiTi_2(PO_4)_3/Li_2S$	$LiTi_2(PO_4)_3 \rightarrow Li_2Ti_2(PO_4)_3$	$6\ Li_2S + LiTi_2(PO_4)_3 \rightarrow 2\ Li_2TiS_3 + 3\ Li_3PO_4$
$Li_3OCl/LiCoO_2$	$3\ Li_3ClO \rightarrow LiClO_3 + 2\ LiCl$	$3\ Li_3ClO \rightarrow LiClO_3 + 2\ LiCl$
$Li_3OCl/LiFePO_4$	$3\ Li_3ClO \rightarrow LiClO_3 + 2\ LiCl$	$3\ Li_3ClO \rightarrow LiClO_3 + 2\ LiCl$
$Li_3OCl/LiMnO_2$	$3\ Li_3ClO \rightarrow LiClO_3 + 2\ LiCl$	$3\ Li_3ClO \rightarrow 2\ LiCl + LiClO_3$
$Li_3OCl/LiNiO_2$	$3\ Li_3ClO \rightarrow LiClO_3 + 2\ LiCl$	$3\ Li_3ClO \rightarrow LiClO_3 + 2\ LiCl$
$Li_3OCl/LiTiS_2$	none	$LiTiS_2 + 3\ Li_3ClO \rightarrow 3\ LiCl + 2\ Li_2S + Li_2TiO_3$
$Li_3OCl/LiVS_2$	none	$LiVS_2 + 12\ Li_3ClO \rightarrow 2\ Li_2SO_4 + 12\ LiCl + Li_3VO_4$
Li_3OCl/Li_2S	none	$Li_2S + 4\ Li_3ClO \rightarrow Li_2SO_4 + 4\ LiCl$

B.5 Bromides

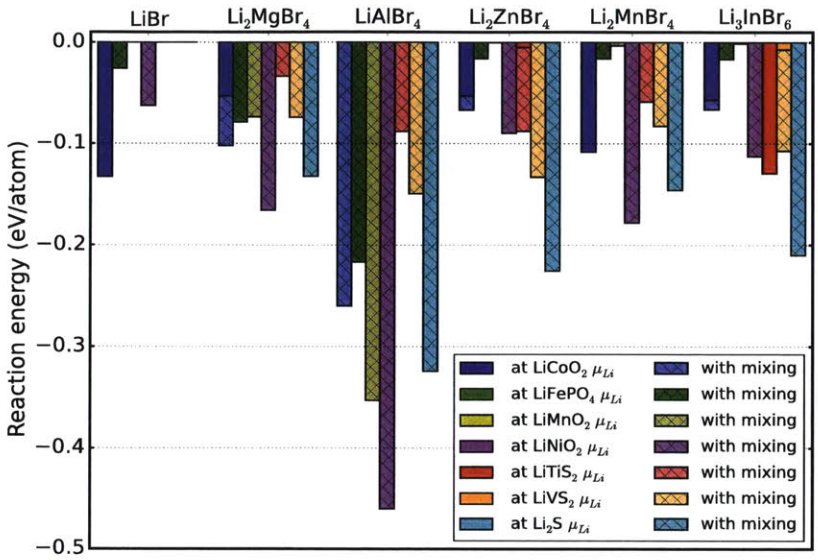

Figure B-5: **Reaction energies for the interfaces of bromide electrolytes.** Calculations performed at μ_{Li} corresponding to the average cathode voltage. Energies are given both for the energy of the lithium extraction only (no mixing) and for energy of cathode/electrolyte mixing open to lithium, following the procedure of figure 5-5.

Table B.7: **Decomposition reactions of bromide electrolytes.** Predicted decomposition reactions for the bromide electrolytes of figure B-5 at cathode chemical potentials and mixing reactions with the cathode.

cathode/electrolyte	reaction at cathode voltage	reaction with mixing
$LiBr/LiCoO_2$	$LiBr \rightarrow Br$	$LiBr \rightarrow Br$
$LiBr/LiFePO_4$	none	$LiFePO_4 + 4\ LiBr \rightarrow LiFeBr_4 + Li_3PO_4$
$LiBr/LiMnO_2$	none	none
$LiBr/LiNiO_2$	none	$3\ LiNiO_2 + LiBr \rightarrow LiBrO_3 + 3\ NiO$
$LiBr/LiTiS_2$	none	none
$LiBr/LiVS_2$	none	none
$LiBr/Li_2S$	none	none

$Li_2MgBr_4/LiCoO_2$	$Li_2MgBr_4 \rightarrow MgBr_2 + 2\ Br$	$2\ LiCoO_2 + Li_2MgBr_4 \rightarrow 4\ Br + Mg(CoO_2)_2$
$Li_2MgBr_4/LiFePO_4$	none	$2\ LiFePO_4 + 3\ Li_2MgBr_4 \rightarrow Mg_3(PO_4)_2 + 4\ LiBr + 2\ LiFeBr_4$
$Li_2MgBr_4/LiMnO_2$	none	$2\ LiMnO_2 + 2\ Li_2MgBr_4 \rightarrow 6\ LiBr + Mg_2MnO_4 + MnBr_2$
$Li_2MgBr_4/LiNiO_2$	none	$2\ LiNiO_2 + 2\ Li_2MgBr_4 \rightarrow 8\ LiBr + NiO + Mg_2NiO_3$
$Li_2MgBr_4/LiTiS_2$	none	$2\ LiTiS_2 + Li_2MgBr_4 \rightarrow MgS + 4\ LiBr + Ti_2S_3$
$Li_2MgBr_4/LiVS_2$	none	$3\ LiVS_2 + 2\ Li_2MgBr_4 \rightarrow 8\ LiBr + V_3S_4 + 2\ MgS$
Li_2MgBr_4/Li_2S	none	$Li_2S + Li_2MgBr_4 \rightarrow MgS + 4\ LiBr$
$LiAlBr_4/LiCoO_2$	none	$2\ LiCoO_2 + 2\ LiAlBr_4 \rightarrow Al_2CoO_4 + 5\ Br + CoBr_3$
$LiAlBr_4/LiFePO_4$	none	$LiFePO_4 + LiAlBr_4 \rightarrow AlPO_4 + LiFeBr_4$
$LiAlBr_4/LiMnO_2$	none	$3\ LiMnO_2 + 4\ LiAlBr_4 \rightarrow 2\ Al_2O_3 + 10\ LiBr + 3\ MnBr_2$
$LiAlBr_4/LiNiO_2$	none	$4\ LiNiO_2 + 5\ LiAlBr_4 \rightarrow 12\ LiBr + LiAl_5O_8 + 4\ NiBr_2$
$LiAlBr_4/LiTiS_2$	none	$2\ LiTiS_2 + LiAlBr_4 \rightarrow 4\ LiBr + 2\ TiS + LiAlS_2$
$LiAlBr_4/LiVS_2$	none	$3\ LiVS_2 + LiAlBr_4 \rightarrow 4\ LiBr + V_3S_4 + LiAlS_2$
$LiAlBr_4/Li_2S$	none	$2\ Li_2S + LiAlBr_4 \rightarrow 4\ LiBr + LiAlS_2$
$Li_2ZnBr_4/LiCoO_2$	$Li_2ZnBr_4 \rightarrow ZnBr_2 + 2\ Br$	$100\ LiCoO_2 + 5\ Li_2ZnBr_4 \rightarrow 27\ Co_3O_4 + Zn_5Co_{19}O_{32} + 20\ LiBrO_3$
$Li_2ZnBr_4/LiFePO_4$	none	$LiFePO_4 + 2\ Li_2ZnBr_4 \rightarrow 2\ ZnBr_2 + Li_3PO_4 + LiFeBr_4$
$Li_2ZnBr_4/LiMnO_2$	none	$6\ LiMnO_2 + Li_2ZnBr_4 \rightarrow Li_2Mn_3ZnO_8 + 4\ LiBr + Mn_3O_4$
$Li_2ZnBr_4/LiNiO_2$	none	$LiNiO_2 + Li_2ZnBr_4 \rightarrow NiO + 4\ LiBr + ZnO$
$Li_2ZnBr_4/LiTiS_2$	$Li_2ZnBr_4 \rightarrow Zn + 4\ LiBr$	$LiTiS_2 + Li_2ZnBr_4 \rightarrow TiS + 4\ LiBr + ZnS$
$Li_2ZnBr_4/LiVS_2$	none	$3\ LiVS_2 + 2\ Li_2ZnBr_4 \rightarrow V_3S_4 + 8\ LiBr + 2\ ZnS$
Li_2ZnBr_4/Li_2S	none	$Li_2S + Li_2ZnBr_4 \rightarrow 4\ LiBr + ZnS$

$Li_2MnBr_4/LiCoO_2$	$Li_2MnBr_4 \rightarrow MnBr_4$	$Li_2MnBr_4 \rightarrow MnBr_4$
$Li_2MnBr_4/LiFePO_4$	none	$LiFePO_4 + 2\ Li_2MnBr_4 \rightarrow LiFeBr_4 + 2\ MnBr_2 + Li_3PO_4$
$Li_2MnBr_4/LiMnO_2$	none	$2\ LiMnO_2 + Li_2MnBr_4 \rightarrow Mn_3O_4 + 4\ LiBr$
$Li_2MnBr_4/LiNiO_2$	none	$7\ LiNiO_2 + 3\ Li_2MnBr_4 \rightarrow 6\ NiO + Li_2Mn_3NiO_8 + 12\ LiBr$
$Li_2MnBr_4/LiTiS_2$	none	$2\ LiTiS_2 + 2\ Li_2MnBr_4 \rightarrow Ti_2S_3 + 8\ LiBr + Mn_2S$
$Li_2MnBr_4/LiVS_2$	none	$3\ LiVS_2 + 2\ Li_2MnBr_4 \rightarrow 2\ MnS + 8\ LiBr + V_3S_4$
Li_2MnBr_4/Li_2S	none	$Li_2S + Li_2MnBr_4 \rightarrow MnS + 4\ LiBr$
$Li_3InBr_6/LiCoO_2$	$Li_3InBr_6 \rightarrow InBr_3 + 3\ Br$	$27\ LiCoO_2 + 2\ Li_3InBr_6 \rightarrow 6\ LiBrO_3 + 2\ InBr_3 + 9\ Co_3O_4$
$Li_3InBr_6/LiFePO_4$	none	$3\ LiFePO_4 + 4\ Li_3InBr_6 \rightarrow 3\ LiFeBr_4 + 3\ Li_3PO_4 + 4\ InBr_3$
$Li_3InBr_6/LiMnO_2$	none	$3\ LiMnO_2 + 2\ Li_3InBr_6 \rightarrow 2\ InBrO + 10\ LiBr + Mn_3O_4$
$Li_3InBr_6/LiNiO_2$	none	$3\ LiNiO_2 + 2\ Li_3InBr_6 \rightarrow In_2O_3 + 12\ LiBr + 3\ NiO$
$Li_3InBr_6/LiTiS_2$	$Li_3InBr_6 \rightarrow In + 6\ LiBr$	$Li_3InBr_6 \rightarrow In + 6\ LiBr$
$Li_3InBr_6/LiVS_2$	$Li_3InBr_6 \rightarrow 6\ LiBr + In$	$3\ LiVS_2 + Li_3InBr_6 \rightarrow V_3S_4 + 6\ LiBr + LiInS_2$
Li_3InBr_6/Li_2S	none	$2\ Li_2S + Li_3InBr_6 \rightarrow 6\ LiBr + LiInS_2$

B.6 Chlorides

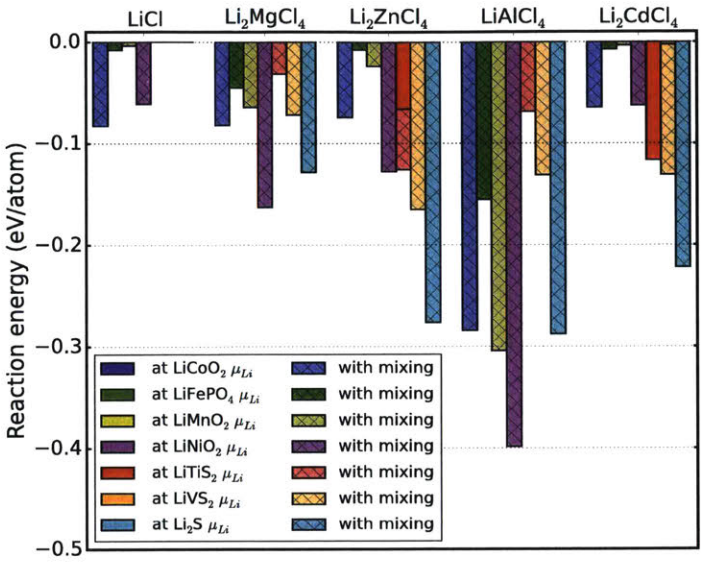

Figure B-6: **Reaction energies for the interfaces of chloride electrolytes.** Calculations performed at μ_{Li} corresponding to the average cathode voltage. Energies are given both for the energy of the lithium extraction only (no mixing) and for energy of cathode/electrolyte mixing open to lithium, following the procedure of figure 5-5.

Table B.8: **Decomposition reactions of chloride electrolytes.** Predicted decomposition reactions for the chloride electrolytes of figure B-6 at cathode chemical potentials and mixing reactions with the cathode.

cathode/electrolyte	reaction at cathode voltage	reaction with mixing
$LiCl/LiCoO_2$	none	$3\ LiCoO_2 + 14\ LiCl \rightarrow 3\ LiCoCl_4 + 2\ LiClO_3$
$LiCl/LiFePO_4$	none	$2\ LiFePO_4 + LiCl \rightarrow Fe_2PClO_4 + Li_3PO_4$
$LiCl/LiMnO_2$	none	$29\ LiMnO_2 + 3\ LiCl \rightarrow 3\ Li_5Mn_7O_{16} + Mn_8Cl_3O_{10}$
$LiCl/LiNiO_2$	none	$3\ LiNiO_2 + LiCl \rightarrow 3\ NiO + LiClO_3$
$LiCl/LiTiS_2$	none	none
$LiCl/LiVS_2$	none	none
$LiCl/Li_2S$	none	none

$Li_2MgCl_4/LiCoO_2$	none	$20\ LiCoO_2 + 7\ Li_2MgCl_4 \rightarrow 7\ Mg(CoO_2)_2 + 6\ LiCoCl_4 + 4\ LiClO_3$
$Li_2MgCl_4/LiFePO_4$	none	$2\ LiFePO_4 + 3\ Li_2MgCl_4 \rightarrow 8\ LiCl + 2\ FeCl_2 + Mg_3(PO_4)_2$
$Li_2MgCl_4/LiMnO_2$	none	$11\ LiMnO_2 + 10\ Li_2MgCl_4 \rightarrow 32\ LiCl + 5\ Mg_2MnO_4 + 2\ Mn_3Cl_4O$
$Li_2MgCl_4/LiNiO_2$	none	$2\ LiNiO_2 + 2\ Li_2MgCl_4 \rightarrow Mg_2NiO_3 + NiO + 8\ LiCl$
$Li_2MgCl_4/LiTiS_2$	none	$2\ LiTiS_2 + Li_2MgCl_4 \rightarrow 4\ LiCl + MgS + Ti_2S_3$
$Li_2MgCl_4/LiVS_2$	none	$3\ LiVS_2 + 2\ Li_2MgCl_4 \rightarrow V_3S_4 + 8\ LiCl + 2\ MgS$
Li_2MgCl_4/Li_2S	none	$Li_2S + Li_2MgCl_4 \rightarrow MgS + 4\ LiCl$
$Li_2ZnCl_4/LiCoO_2$	none	$20\ LiCoO_2 + 7\ Li_2ZnCl_4 \rightarrow 4\ LiClO_3 + 7\ Zn(CoO_2)_2 + 6\ LiCoCl_4$
$Li_2ZnCl_4/LiFePO_4$	none	$8\ LiFePO_4 + Li_2ZnCl_4 \rightarrow LiZnPO_4 + 4\ Fe_2PClO_4 + 3\ Li_3PO_4$
$Li_2ZnCl_4/LiMnO_2$	none	$8\ LiMnO_2 + 6\ Li_2ZnCl_4 \rightarrow 21\ LiCl + Mn_8Cl_3O_{10} + 6\ ZnO$
$Li_2ZnCl_4/LiNiO_2$	none	$LiNiO_2 + Li_2ZnCl_4 \rightarrow 4\ LiCl + NiO + ZnO$
$Li_2ZnCl_4/LiTiS_2$	$Li_2ZnCl_4 \rightarrow Zn + 4\ LiCl$	$LiTiS_2 + Li_2ZnCl_4 \rightarrow 4\ LiCl + TiS + ZnS$
$Li_2ZnCl_4/LiVS_2$	none	$3\ LiVS_2 + 2\ Li_2ZnCl_4 \rightarrow V_3S_4 + 8\ LiCl + 2\ ZnS$
Li_2ZnCl_4/Li_2S	none	$Li_2S + Li_2ZnCl_4 \rightarrow 4\ LiCl + ZnS$
$LiAlCl_4/LiCoO_2$	none	$3\ LiCoO_2 + 4\ LiAlCl_4 \rightarrow Li_5CoCl_8 + 2\ Al_2O_3 + 2\ LiCoCl_4$
$LiAlCl_4/LiFePO_4$	none	$LiFePO_4 + LiAlCl_4 \rightarrow 2\ LiCl + FeCl_2 + AlPO_4$
$LiAlCl_4/LiMnO_2$	none	$3\ LiMnO_2 + 4\ LiAlCl_4 \rightarrow 3\ LiMnCl_4 + 4\ LiCl + 2\ Al_2O_3$
$LiAlCl_4/LiNiO_2$	none	$4\ LiNiO_2 + 5\ LiAlCl_4 \rightarrow 12\ LiCl + 4\ NiCl_2 + LiAl_5O_8$
$LiAlCl_4/LiTiS_2$	none	$4\ LiTiS_2 + LiAlCl_4 \rightarrow 2\ Ti_2S_3 + 4\ LiCl + LiAlS_2$
$LiAlCl_4/LiVS_2$	none	$3\ LiVS_2 + LiAlCl_4 \rightarrow 4\ LiCl + V_3S_4 + LiAlS_2$
$LiAlCl_4/Li_2S$	none	$2\ Li_2S + LiAlCl_4 \rightarrow 4\ LiCl + LiAlS_2$

$Li_2CdCl_4/LiCoO_2$	none	$9\ LiCoO_2 + Li_2CdCl_4 \rightarrow CdCl_2 + 3\ Co_3O_4 + 2\ LiClO_3$
$Li_2CdCl_4/LiFePO_4$	none	$4\ LiFePO_4 + Li_2CdCl_4 \rightarrow 2\ Li_3PO_4 + 2\ Fe_2PClO_4 + CdCl_2$
$Li_2CdCl_4/LiMnO_2$	none	$58\ LiMnO_2 + 3\ Li_2CdCl_4 \rightarrow 2\ Mn_8Cl_3O_{10} + 6\ Li_5Mn_7O_{16} + 3\ CdCl_2$
$Li_2CdCl_4/LiNiO_2$	none	$13\ LiNiO_2 + Li_2CdCl_4 \rightarrow 13\ NiO + 4\ LiClO_3 + CdO$
$Li_2CdCl_4/LiTiS_2$	$Li_2CdCl_4 \rightarrow Cd + 4\ LiCl$	$Li_2CdCl_4 \rightarrow Cd + 4\ LiCl$
$Li_2CdCl_4/LiVS_2$	$Li_2CdCl_4 \rightarrow Cd + 4\ LiCl$	$3\ LiVS_2 + 2\ Li_2CdCl_4 \rightarrow 2\ CdS + 8\ LiCl + V_3S_4$
Li_2CdCl_4/Li_2S	none	$Li_2S + Li_2CdCl_4 \rightarrow 4\ LiCl + CdS$

B.7 Fluorides

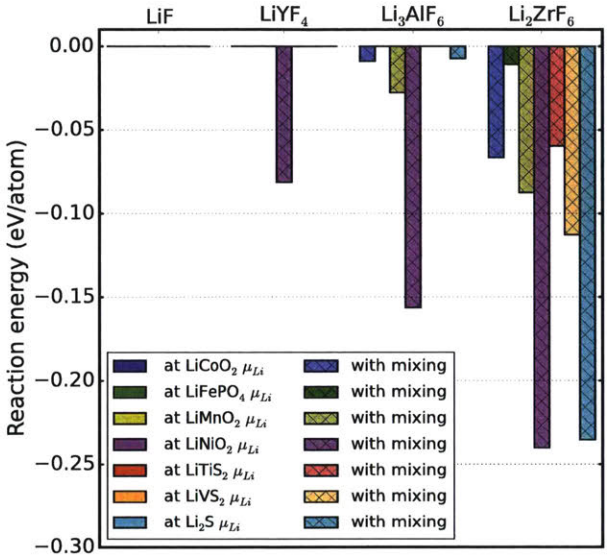

Figure B-7: **Reaction energies for the interfaces of fluoride electrolytes.** Calculations performed at μ_{Li} corresponding to the average cathode voltage. Energies are given both for the energy of the lithium extraction only (no mixing) and for energy of cathode/electrolyte mixing open to lithium, following the procedure of figure 5-5.

Table B.9: **Decomposition reactions of fluoride electrolytes.** Predicted decomposition reactions for the fluoride electrolytes of figure B-7 at cathode chemical potentials and mixing reactions with the cathode.

cathode/electrolyte	reaction at cathode voltage	reaction with mixing
$LiF/LiCoO_2$	none	none
$LiF/LiFePO_4$	none	none
$LiF/LiMnO_2$	none	none
$LiF/LiNiO_2$	none	none
$LiF/LiTiS_2$	none	none
$LiF/LiVS_2$	none	none
LiF/Li_2S	none	none
$LiYF_4/LiCoO_2$	none	none
$LiYF_4/LiFePO_4$	none	none
$LiYF_4/LiMnO_2$	none	none
$LiYF_4/LiNiO_2$	none	$3\ LiNiO_2 + 2\ LiYF_4 \rightarrow Y_2O_3 + 3\ NiO + 8\ LiF$
$LiYF_4/LiTiS_2$	none	none
$LiYF_4/LiVS_2$	none	none
$LiYF_4/Li_2S$	none	none
$Li_3AlF_6/LiCoO_2$	none	$12\ LiCoO_2 + 5\ Li_3AlF_6 \rightarrow LiAl_5O_8 + 30\ LiF + 4\ Co_3O_4$
$Li_3AlF_6/LiFePO_4$	none	none
$Li_3AlF_6/LiMnO_2$	none	$12\ LiMnO_2 + 5\ Li_3AlF_6 \rightarrow 4\ Mn_3O_4 + LiAl_5O_8 + 30\ LiF$
$Li_3AlF_6/LiNiO_2$	none	$2\ LiNiO_2 + Li_3AlF_6 \rightarrow LiAlO_2 + 6\ LiF + 2\ NiO$
$Li_3AlF_6/LiTiS_2$	none	none
$Li_3AlF_6/LiVS_2$	none	none
Li_3AlF_6/Li_2S	none	$4\ Li_2S + Li_3AlF_6 \rightarrow Li_5AlS_4 + 6\ LiF$
$Li_2ZrF_6/LiCoO_2$	none	$3\ LiCoO_2 + Li_2ZrF_6 \rightarrow 6\ LiF + Co_3O_4 + ZrO_2$
$Li_2ZrF_6/LiFePO_4$	none	$9\ LiFePO_4 + 2\ Li_2ZrF_6 \rightarrow 3\ Fe_3(PO_4)_2 + 12\ LiF + LiZr_2(PO_4)_3$
$Li_2ZrF_6/LiMnO_2$	none	$3\ LiMnO_2 + Li_2ZrF_6 \rightarrow 6\ LiF + ZrO_2 + Mn_3O_4$
$Li_2ZrF_6/LiNiO_2$	none	$2\ LiNiO_2 + Li_2ZrF_6 \rightarrow 2\ NiO + ZrO_2 + 6\ LiF$
$Li_2ZrF_6/LiTiS_2$	none	$4\ LiTiS_2 + Li_2ZrF_6 \rightarrow ZrS_2 + 2\ Ti_2S_3 + 6\ LiF$
$Li_2ZrF_6/LiVS_2$	none	$3\ LiVS_2 + Li_2ZrF_6 \rightarrow 6\ LiF + V_3S_4 + ZrS_2$
Li_2ZrF_6/Li_2S	none	$3\ Li_2S + Li_2ZrF_6 \rightarrow Li_2ZrS_3 + 6\ LiF$